FORMATION, CHARACTERIZATION, AND FLOW DYNAMICS OF NANOSTRUCTURE MODIFIED SENSITIVE AND SELECTIVE GAS SENSORS BASED ON POROUS SILICON

A Thesis
Presented to
The Academic Faculty

by

Serdar Ozdemir

In Partial Fulfillment
of the Requirements for the Degree
of Doctor of Philosophy in the
School of Physics

Georgia Institute of Technology
May 2011

FORMATION, CHARACTERIZATION, AND FLOW DYNAMICS OF NANOSTRUCTURE MODIFIED SENSITIVE AND SELECTIVE GAS SENSORS BASED ON POROUS SILICON

Approved by:

Dr. James L. Gole, Advisor
School of Physics
Georgia Institute of Technology

Dr. Peter Hesketh
School of School of Mechanical Engineering
Georgia Institute of Technology

Dr. Philip First
School of Physics
Georgia Institute of Technology

Dr. Andrei Fedorov
School of Mechanical Engineering
Georgia Institute of Technology

Dr. Ahmet Erbil
School of Physics
Georgia Institute of Technology

Date Approved: March 18, 2011

To my parents, Ramazan and Adalet Ozdemir
for their continuous support.

ACKNOWLEDGEMENTS

There are many people without whom, the work in this thesis wouldn't be completed. First of all, I would like to thank to my advisor Prof James Gole for stimulating scientific discussions. The interesting idea of using acidic and basic characters of metal oxides to understand the physisorptive solid-gas interactions and implementation of this idea on porous silicon interfaces came from him. Without him, I wouldn't be able to do this work. I especially admire his willingness and energy to do science. I would like to thank to Prof Hesketh for valuable discussions about gas sensors. I would have to especially thank to Prof Erbil because he let us use his lab when we urgently needed a chemical hood for experiments.

I would also like to thank to all of my committee members: Prof Hesketh, Prof Erbil, Prof First and Prof Fedorov for their reading of this thesis as well as their feedback and time they spent during the thesis defense.

I would like to thank to Dr Jiguang-Li for valuable discussions about nanoparticles and solgel methods. I would like to thank to Dr Steve Lewis, Dr John DeBoer, Dr Jimmy Corno, and Dr Se Il Lee, with whom I worked together for almost two years, for their fundamental work in the initial phase of the porous silicon research. I would like to thank to Dr Huseyin Kurtuldu. I got the idea of using image processing to calculate pore coverage on the surface after stimulating discussions about his experimental setup. I would have to thank to the friendly cleanroom staff and cleanroom manager Gary Spinner.

I would like to thank to William Laminack, Jenna Campbell, Dan Weisgerber and Tommy Osborne, Aaron Hansen, Chu-Lai Cheung, Naveen Pouse and Alisha Kasam and

many other dedicated undergraduate students for their contributions during their undergraduate research studies.

I would have to thank to all of my friends at School of Physics who have indirectly affected the success of this work. I would have to especially thank to Menderes Iskin, Gungor Ozer, Huseyin Kurtuldu, Serkan Dursun, Menal Guzelsoy, Onur Kececigil and Emiliano Papa for fun and fruitful discussions. My previous roommates Claus Christmann, Will Fenwick and Daniele Gianni definitely helped my smooth adaption to the USA. I am very thankful to all of them.

TABLE OF CONTENTS

LIST OF TABLES

LIST OF FIGURES

SUMMARY

Nanopore covered microporous silicon interfaces have been formed via an electrochemical etch for gas sensor applications. Rapid reversible and sensitive gas sensors have been fabricated. Both top-down and bottom-up approaches are utilized in the process. A nano-pore coated micro-porous silicon surface is modified selectively for sub-ppm detection of NH_3, PH_3, NO, H_2S, SO_2. The selective depositions include electrolessly generated SnO_2, Cu_xO, Au_xO, NiO, and nanoparticles such as TiO_2, MgO doped TiO_2, Al_2O_3, and ZrO_2. Flow dynamics are analyzed via numerical simulations and response data. An array of sensors is formed to analyze mixed gas response. A general coating selection method for chemical sensors is established via an extrapolation on the inverse of the Hard-Soft Acid-Base concept.

In Chapter 1, the current state of the porous silicon gas sensor research is reviewed. Since metal oxide thin films, and, recently, nanowires are dominantly used for sensing application, the general properties of metal oxides are also discussed in this chapter. This chapter is concluded with a discussion about commercial gas sensors and the advantages of using porous silicon as a sensing material. The PS review discussed at the beginning of this chapter is an overview of the following publication:

• ”*The Potential of Porous Silicon Gas Sensors*”, Serdar Ozdemir, James L. Gole, Current Opinion in Solid State and Materials Science, 11, 92-100 (2007).

In Chapter 2, porous silicon formation is explained in detail. Interesting results of various silicon anodization experiments are discussed. In the second part of this chapter, the microfabrication process of porous silicon conductometric gas sensors and gas testing set up are briefly introduced.

In chapter 3, metal oxide nanoparticle/nanocluster formation and characterization experiments via SEM and XPS analysis are discussed.

Chapter 4 is an overview of the test results for various concentrations NH_3, NO, NO_2 and PH_3. The interaction strengths between the test gases and various nanoparticles on porous silicon are measured. The flow dynamics in the micro- and nanoporous regime is analyzed by using experimental response data and numerical simulations. The results in this chapter are partially published in the following articles:

• ”*Porous Silicon Gas Sensors for Room Temperature Detection of Ammonia and Phosphine*”, 214th Meeting of ECS: Honolulu, Hawaii Oct 12-17, 2008, S. Ozdemir, J.L. Gole, ECS Trans. 16 (11), 379 (2008).

• ”*A Phosphine Detection Matrix Using Porous Silicon Gas Sensors*” S. Ozdemir, J.L. Gole, Sensors and Actuators B, 151, 274-280 (2010).

• "*A Nanostructure Modified Porous Silicon Gas Sensor Detection Matrix for NO with Demonstration of the Transient Conversion of NO to NO_2*", Serdar Ozdemir, Thomas B. Osburn, James L. Gole, submitted to Journal of Electrochemical Society.

• ” *Selectivity Improvement and Response Time Scale of Porous Silicon Conductometric Gas Sensors*” S. Ozdemir, J. L. Gole, ECS Transactions, Volume 33, Issue 8, pg 111-115.

In chapter 5, a model is proposed for selectivity improvements in PS gas sensors based on Inverse of Hard Soft Acid Base interactions. An extended version of this chapter is published in the following publication:

• ”*Nanostructure directed physisorption vs. chemisorption at semiconductor interfaces: the inverse of the hard-soft acid-base (HSAB) concep*t”, J.L.Gole, S. Ozdemir, ChemPhysChem, 11, 2573–2581 (2010).

Chapter 6 is a brief conclusion of the results discussed in this thesis.

CHAPTER 1

INTRODUCTION

Gas sensors have been widely used in various parts of everyday life. As early as the 19th century, historical evidence shows that there was a need for gas sensors for life threatening gases such as carbon monoxide (CO) and methane (CH_4), especially in mines. Canaries were the first choice of gas leak detection at the time. As time went on, different methods for gas sensing had been proposed and applied to a certain degree. Flame safety lamps, where the amount of flame is the indication of concentration, with a low level of accuracy were introduced [1]. Early catalytic sensors were used to burn the combustible gas and to measure the resistance change of a catalytic wire due the released heat. Electrochemical detectors which determine the amount of gas by measuring the current between two electrodes, where oxidation and reduction (redox) processes occur upon gas exposure, have been another choice. As industrialization continued through the 20th century, gas detection technology for monitoring toxic gases progressed in a parallel path. Dodd and Persaud introduced the idea of an electronic nose by using different metal oxides in array configurations to mimic biological olfactory systems [2,3]. Conductometric gas sensors based on metal oxide gas sensors are one of the most studied groups of gas sensors. It has been known that the resistance of a surface may change due to adsorption or desorption of gases since the 1960s [4]. The mechanism for gas detection in these materials is based on reactions that change the concentration of adsorbed oxygen on the materials surface. Oxygen adsorbed onto the surface removes charges from the bulk limiting the electron movement and conductivity of the material.

One of the foremost application areas of today's gas sensors is their use in the automotive and industrial sector for environmental protection. NO_x, O_2, NH_3, SO_2, CO, CO_2, and hydrocarbon detection has been the major concern for environmental protection [5]. Gas leak detectors, where CO_2 and combustible gases are the target gases, have also been employed for household safety. The medical use of gas sensors such as exhaled NO_x monitoring for asthma patients is also a rapidly growing field. In food industries, gas sensors have been used to monitor and control the fermentation process. After World War I, chemical warfare has initiated the need for monitoring certain gases such as chlorides,

nitrogen oxides, mustard gas, and sarin gas. There are about 70 different chemicals classified as chemical warfare agents that need to be detected even in low quantities. Detection of explosives such as TNT is another research field gaining momentum for gas sensor applications.

Among the various kinds of sensing methods; IR detection, UV-Vis spectroscopy, mass spectroscopy, or gas chromatography are conclusive and highly reliably methods even for detecting parts per billion (ppb) levels. Even though these methods/tools are precise, their physical size, cost and operation complexity prevent them from entering into everyday life use and mass commercialization [5]. However, in contrast, semiconducting sensors stand out for low cost and mobile applications.

In this work, the reactive surface area of a porous silicon (PS) semiconductor is combined with well known metal oxide nanoparticles/clusters to tune sensitivity and selectivity for various gases encountered in environmental problems. The proposal of combining PS and metal oxides on the same sensor may enable the production of a smart sensor system with signal processing and interconnects processed on silicon and metal oxide nanostructures that can alter the response at different concentration levels on the same substrate at room temperature by combining bottom-up and top-down micro/nano fabrication approaches (Figure 1.1). Two dimensional metal oxide films have been investigated for the past few decades. Recently, there has been ongoing research on one dimensional metal oxide nanowires, measuring their reactivity when they are placed between two electrodes and exposed to target gases. From a scientific point of view, the response of zero dimensional nanoparticles/clusters is still a fresh field due to the practical difficulties of designing devices and taking measurements for such dimensionality. Measuring the effect of metal oxides dispersed on a PS surface will give insight to important size dependent effects since it is not practical or easy to investigate solid-gas interactions on individual nanoparticles or clusters of various sizes. From a practical point of view, these kinds of operational, small and portable gas sensor devices can be used in a vast variety of products such as personal items (e.g. cell phones, automobiles), household items (e.g stoves, vacuum cleaners), industrial plants, and aeronautical applications (e.g. space stations).

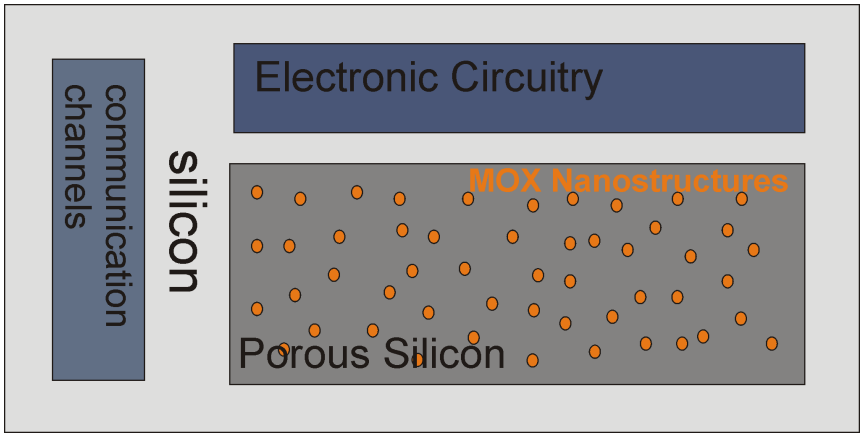

Figure 1.1 Choosing porous silicon as a substrate material will enable integrated smart sensor configurations combining electronic circuitry on silicon with the receptor function of metal oxide (MOX) nanostructures on the same substrate.

1.1 Porous Silicon as a Substrate Material for Gas Sensing

Porous silicon (PS) has drawn considerable attention for sensor applications. Its luminescence properties, large surface area, and compatibility with silicon based technologies have been the driving force for this technology development. Recently biochemical [6-8], microfluidic flow [9], temperature and pressure [10], magnetic [11,12], chemical ion [13] and gas sensors have been reported. Chemical functionalization of the large surface areas, which can be generated in PS, shows the potential for developing a variety of gas sensors. Humidity, organic solvents, CO_x, NO_x, NH_3, O_2, H_2, HCl, SO_2, H_2S and PH_3 have all been detected. In this chapter, the current state of the art PS gas sensor designs and their capabilities will be shortly discussed. Afterwards, the possible surface functionalization mechanisms and current state of the metal oxide nanoparticles and their applications will be introduced and a comparison between commercial thin film metal oxide gas sensors and PS gas sensors will be explained in the context of PS functionalization.

1.1.1 Humidity Detection

Humidity sensors represent one of the most widely studied applications of PS [14-19]. The large surface area intrinsic to PS enables sufficient water condensation to modify the electrical properties of the system. Differing relative humidity (RH) levels vary the amount of water adsorbed on the PS layer (PSL) and the PS sensor response to

RH is a function of both pressure and temperature. Nanoporous silicon exhibits two important properties; high resistivity (>10^5 Ω cm) due to free carrier depletion and a low dielectric constant (2-3 in vacuum) [16]. The adsorbed moisture on the PSL changes the dielectric constant and varies the capacitance of PS accordingly. Pore formation results from the anodization of an n or p type silicon wafer [16-17]; electrical contacts are generally coated onto the PSL and the backside of the etched wafer. A capacitance measurement between these contacts at different RH levels results in the change in response depicted in Fig 1.2 [16]. Here, the response time is less than 1 min for a change from ambient climate to 95 % RH at 20 ^{0}C [16].

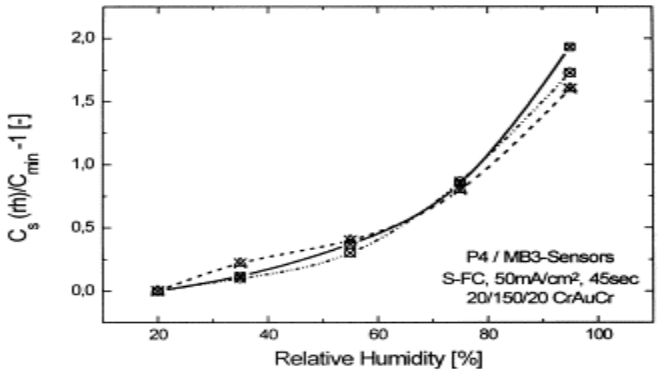

Figure 1.2. Humidity sensitivity of the sensor with a dielectric of 1 μm porous Si [16].

Björkvist et. al. have used thermal oxidation and thermal carbonization (TC) [15,18] to obtain better stability of the PSL in chemically harsh environments and presumably better sensitivity due to a larger surface area. PS carbonized at 500-650 ^{0}C becomes hydrophobic while at higher temperatures, 720-850 ^{0}C, it is hydrophilic. The response time for low humidity levels (< 70 %) is under 90 s. but it is greater than 120 s for higher humidity levels. Björkvist et. al. have now utilized pore size enlargement, making use of an integrated resistor heating the sensor, to obtain better hysteresis in TC PS [19]. Figure 1.3 shows the achieved hysteresis.

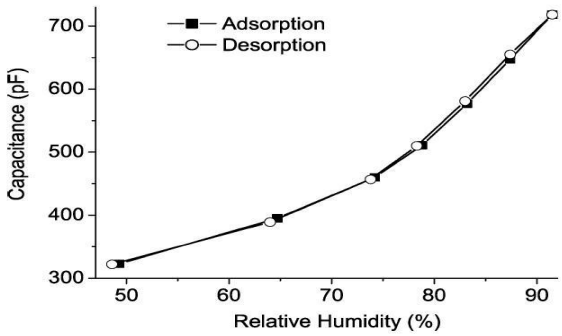

Figure 1.3. Hysteresis loop for TC PS with larger pores [19]. Humidity conditions are changed every 4 min.

1.1.2 Organic Vapor Detection

Research on organic vapor (acetone, ethanol, methanol etc.) detection using PS sensors has been ongoing [20-28]. These sensors follow two detection pathways involving (1) changes in electrical properties of the porous layer and (2) detection by optical property changes.

Both the capacitance and conductance change of a PSL can be employed to detect levels of exposure to gas species. Different contact configurations to (1) the PSL and the back side of the wafer [21], (2) only on the PSL [22], and (3) only on the back side of the wafer [23] have been suggested. For exposure to 4 % acetone, methanol and ethanol, Iraji zad et al. exploit the relative conductance to measure large and differing currents passing through the PSL under constant voltage with a response time of about 1000 s [22]. These sensitivities are achieved using the highest porosity samples that can be formed in a p type polysilicon wafer of 0.4-2 Ω cm resistivity anodized in 13 % concentrated HF solution at 30 mA/cm^2 for 5 minutes. After pore formation, the samples are oxidized in air at 350 ^{0}C for 1 hour [22]. A smaller current increase, albeit with tens of seconds response time, has recently been achieved for 1.5 % isopropanol [21].

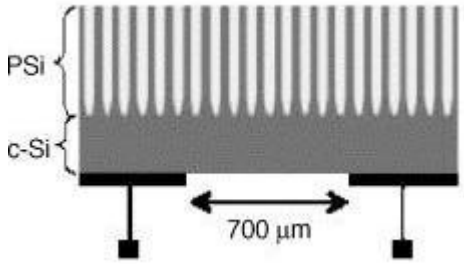

Figure 1.4. The response of the PSL resembles a gate voltage for a Field Effect Transistor [23].

Archer et al. have constructed a PS sensor (Fig. 1.4) where two Al contacts are evaporated onto the backside of a single crystal Si (c-Si) wafer and the capacitance and conductance are measured between these contacts [23]. The response of the sensor is modeled as a Field Effect Transistor (FET) where the conductance is modulated with a gate voltage. According to their space charge region modulation (SCRM) model, a porous layer acts like a gate electrode and the channel is the c-Si substrate. In this model, the space charge or depletion region changes when the porous region is exposed to organic solvents. Because the porous layer is coated with a thin layer of water (humidity), the change in response is related to the polarity of interacting molecules and the degree of exposure. The maximum changes in the capacitance and conductance of the sensor when exposed to 10 µl, of solvent clearly differ (Table 1.1 [23]).

Table 1.1. Maximum percentage changes in capacitance and conductance with respect to tested polar molecules [23].

Solvent	%ΔC	%ΔG
Chloroform	-44	-46
Acetone	-13	-21
Ethanol	-7	-10
Acetonitrile	53	37

The reflectance of the PSL changes when PS is exposed to organic vapors. Thus, 1D photonic crystals of PS have been used as an organic compound sensor with a detection limit of 0.43 % for ethanol using only ~ 0.5 W of power [24]. King et. al. have removed PS photonic crystals of 8 µm thickness and 500 µm diameter using an electropolishing reaction and affixed these to a cleaved silica-core optical fiber using a transparent epoxy [20]. The shift in the wavelength of the reflectance peak maximum for isopropyl alcohol (IPA), trichloroethylene (TCE), cyclohexane, and water in an N_2 carrier gas is shown in Fig. 1.5 [25]. The magnitude of the peak shift is related to the amount of analyte captured on the porous surface and it is reported to be inversely related to the

analyte vapor pressure which is also inversely related to the relative affinity of a surface for the given analyte [25].

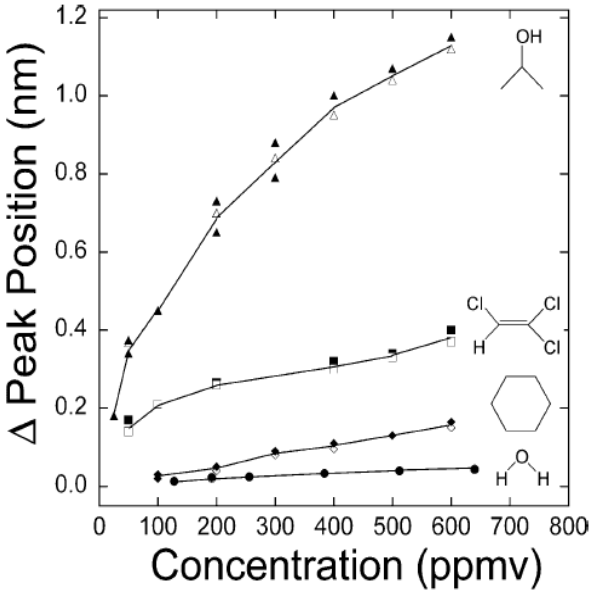

Figure 1.5. PS response to IPA, TCE, cyclohexane, and water in the 50 to 600 ppmv range [25].

Porous silicon oxide microcavity (POSM) sensors which detect the ethanol content in wine via the red-shift in the cavity mode have been reported [26]. Fig. 1.6 [26] shows the magnitude of the shift which is proportional to the alcoholic strength (ethanol) of the wine.

Recently a lab-on-chip sensor using a PS Fabry-Perot monolayer as a transducer has been reported for organic vapor detection [27]. Reflectivity measurements upon exposure to isopropanol, ethanol, and methanol show small response times of 156 ms, 104 ms, and 64 ms respectively. The photoluminescence (PL) variation of PS to gases provides an alternate means of detection. B-cyclodextrin modified PS exhibits a better PL response than unmodified PS [28].

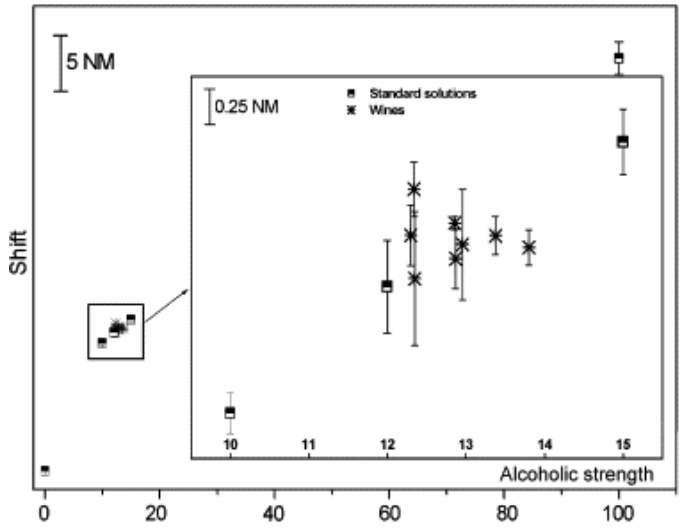

Figure 1.6. Cavity mode red shift for reference solutions and wines as a function of ethanol concentration [26].

1.1.3 CO_x, NO_x, NH_3, O_2, H_2, HCl, SO_2, H_2S, PH_3 Detection

Since PS has a large surface area, coating its surface with a catalyst can increase the response of the sensor considerably. Selectivity can also be provided with this form of surface modification.

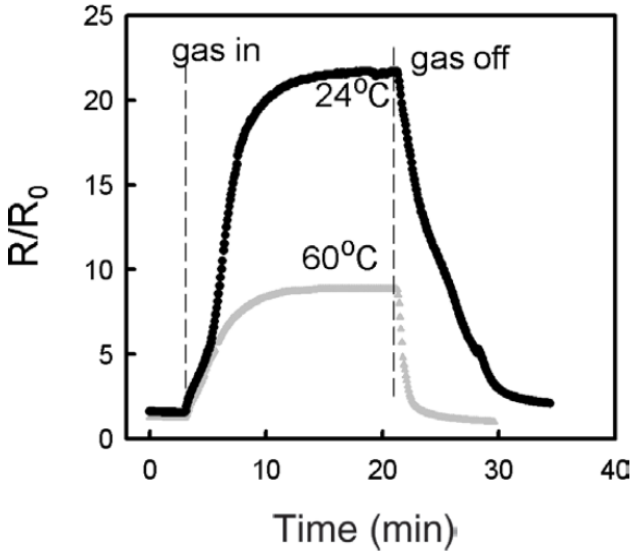

Figure 1.7. Relative resistance change of a Pd coated porous poly-silicon (PPS) at two different operating temperatures in response to 11 % H_2 [29].

In the last decade, there has been increased research on hydrogen due to its potential energy applications. Hydrogen detection via PS sensors has also been proposed.

Rahimi et. al. used an electroless Pd coating onto porous poly-silicon (PPS) for H_2 detection [29]. Here, 0.4-2 Ω cm p type poly-silicon wafers are anodized in 13 % concentrated HF solution with a current density of 32 mA cm^{-2} for 5-40 min. The electroless coating is done using 1.13 10^{-3} M $PdCl_2$ and 1.21 10^{-2} M HCl in water. The penetration depth of Pd in PPS increases with Si etching time. A resistance measurement for 11 % H_2 exposure is shown in Fig 1.7 [29]. The Pd coated PPS sensors exhibit a several thousand ppm sensitivity and a ~250 s response time while untreated PPS shows no response. The resistivity of Pd loaded PPS is found to be 3 orders of magnitude smaller than that of untreated PPS. This suggests that current passes through a Schottky barrier between Si and Pd near a Pd cluster and that the H_2 exposure forms a dipole layer on the surface increasing the Schottky barrier and causing an increase in the overall resistance [31]. TiO_{2-x} has been coated onto PS to achieve 1000-5000 ppm H_2 detection [32]. After pore formation, the PS layer is coated with TiO_{2-x} in an e-beam evaporator and a Pt layer is coated on the oxide layer to provide a catalyst for the splitting of the gas.

Recently, the CH_x treatment of a PSL has been investigated for O_2 detection by Mahmoudi et. al. [32]. The effect of annealing, through O_2 exposure, for a CH_x coated PSL at different temperatures has been investigated. Stable operation has been attained, even at low, 10 mV, bias voltages (Fig. 1.8a [32]). Annealing at 750 ^{0}C is found to give the highest sensitivity (Fig. 1.8b [32]). The same group demonstrate that the PL response of the CH_x coated PS sensors can be used for CO_2 detection after the same annealing treatment [33,34].

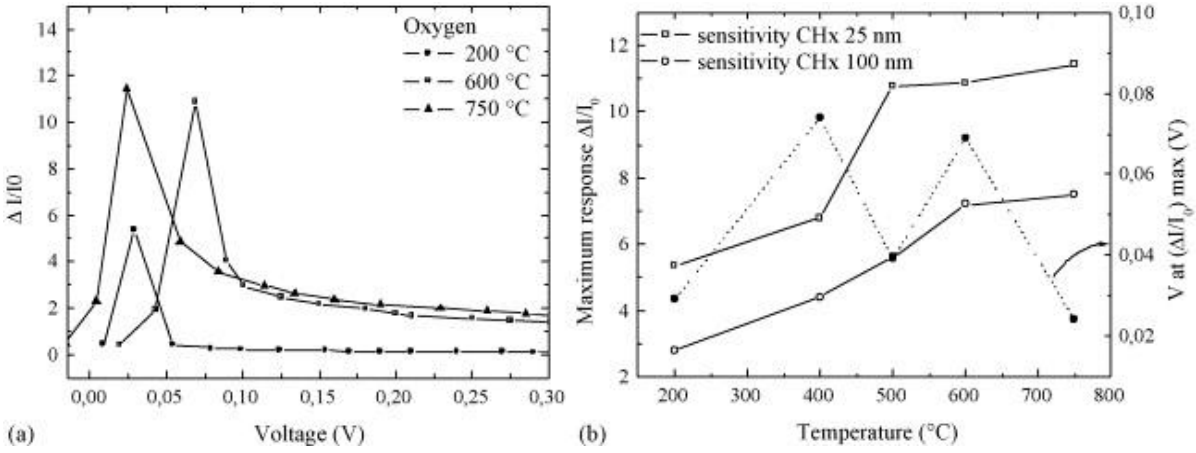

Figure 1.8 a).Sensor response at different operating temperatures and bias voltages. b) Annealing at 750 ^{0}C results in a maximum sensitivity for both 25 and 100 nm CH_x coatings [32].

NO_x is a well known toxic gas associated with air pollution and respiratory disease. NO_2 monitoring with PS sensors has been investigated in the last decade [35-40]. Massera et al. have fabricated a PSL from p-type Si, wafers detaching the layer from a Si wafer using high current densities in electrochemical etching. The membrane is then attached to interdigital contacts pre-deposited on an Al_2O_3 layer [36]. DC electrical measurements are done under NO_2. Responses to concentrations as low as 12 ppb are reported with this sensor [38]. The sensor sensitivity under variable concentrations of NO_2 is given in Fig. 1.9. [37]. Recently, the Pd and SnO_2 treatment of PS sensors has been reported to give rise to a 25 s and 57 s response for sensing liquefied petroleum gas (LPG) and NO_2 [41].

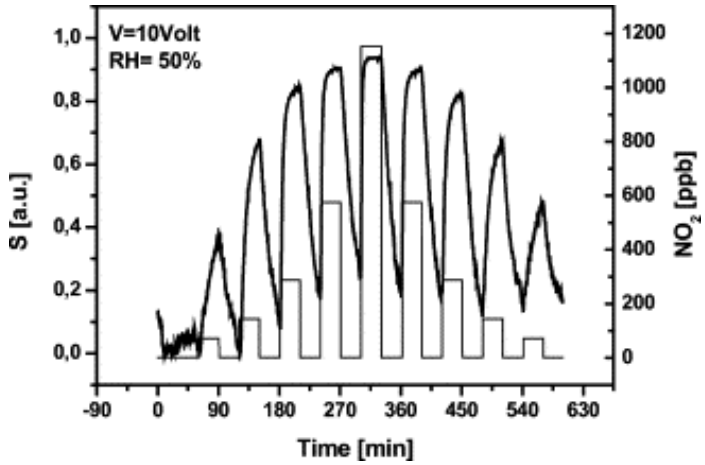

Figure 1.9 Sensitivity of PS NO_2 sensor at 10 V bias voltage in 50 % RH [37].

The basis of this research study emphasizes the important effect which the careful modification of a PS interface can have on the sensing of a variety of gases. Nanopore covered microporous PS interfaces have been formed to provide an active scaffolding for the creation of sensor [41,42] and microreactor [42,43] configurations. Rapidly responding ($\leq 2s$), reversible, and sensitive ($\leq 2ppm$) PS gas sensors, operating at room temperature, and based on a uniquely formed highly efficient electrical contract to the nanopore covered microporous array, are transformed on the basis of a general theory for surface modification by introducing active nanoparticles to establish gas selectivity.

Given the proper preparation of the nanopore coated micropore structure, subsequent treatments with HCl can provide a significant enhancement of the UV light induced photoluminescence (PL) emission from these surfaces [41,44,45]. A combination

of PL induced metallization and electron beam deposition is used to form a unique low-resistance contact to PS. Sensing of HCl, NH_3, CO, NO_x, SO_2, H_2S, and PH_3 at or below the ppm level at bias voltages as low as 100 mV and contact resistances as low as 20Ω [44] has been accomplished [41]. However, the distinguishing feature of this PSGS which is more typically operated in the 1-3 V range is the ability to incorporate not only high sensitivity and selectivity but also the ability to respond rapidly and accurately over a broad range of environmental temperature, pressure, and humidity. With an extremely low power requirement (watch battery) this PSGS sensor provides a combination of high sensitivity (ppb range) and room temperature operation that typical gas sensors do not offer. Furthermore, the sensor shows the potential for operation in elevated temperature combustion environments. Within a framework that is readily amenable to integration into standard CMOS/MEMS technology, novel surface coatings form the basis for operation of sensor arrays operating in concert or employing a divided gas flow in multiple gas environments. This combination, with ready replacement and sensor rejuvenation, can simplify a potentially complex and costly detection process.

A general approach to facilitate significant changes in sensor surface sensitivity for a variety of gases, based on a complementary theory to that of the well known concept of strong and weak acid and base interactions by Pearson and others [46] and commensurate with several established gas-surface interactions [47,48], has now been formulated [49] to create selective surface depositions. The technology as implemented [41,49] on 'phase matching' nanoporous silicon layers positioned on porous silicon micropores facilitates the application of nanostructured metals, metal oxides, and nanopoarticle catalytic coatings, providing for notably higher sensitivities. Within this framework, novel signal filtering techniques [41,50], operative in a pulsed gas environment, are introduced as a means to reliably eliminate false positive signals. A typical PS nanostructure coated microstructured hybrid configuration when fractionally deposited with tin oxide (NO_x, CO) and gold nanostructures (NH_3) provides a greatly increased sensitivity to the indicated gases. Sensing of NH_3 and NO_x for asthmatics and the HCl, PH_3, and formaldehyde products of methamphetamine is possible at or below the 100 ppb level. The introduction of gold and tin-based nanostructures to the micro/nanoporous PS framework, through electroless metal treatments, selectively

modifies the impedance response to considerably improve the detection of NH_3, CO, and NO_x [46]. The introduction of SnO_2 and Au_xO nanostructures to the micro/nanoporous framework to produce the enhanced sensitivity for PS is considerably less. The SnO_x deposited sensor, in particular, allows the room temperature detection of CO at the ppm level considerably below that of other PS sensors [51-53]. This SnO_2 deposited sensor should be compared with PS-based sensors whose resistances exceed hundreds of kΩ operating on a 2V bias [51], SnO_2 sensors operating at 300 ºC -500 ºC [52], and similar gas sensors operating at 2-5 V [53]. The sensitivity of these nanodeposited tin oxide sensors exceeds that of other tin oxide sensors by at least an order of magnitude and at room temperature. Further, more recent surface treatments have lead to the improvement in sensitivity for ammonia.

The proper combination of nanodeposition techniques can be used to produce combinations of array-based devices of varying sensitivity to a variety of gases and this matrix of array responses can be used in tandem to selectivity analyze gas mixtures. For example, an array of an untreated, SnO_2 nanodeposited, and gold clustered oxide deposited sensors could be used to sensitively test for the presence and relative concentrations of ammonia and nitric oxide [41]. A nanostructured tin oxide sensor deposit provides a basis for developing a very sensitive room temperature nitric oxide detector that could be installed in a simple sensor system for asthmatics [41]. The outlined nanodeposits are formed using electroless metal solutions [54], however, there are several additional complimentary modes that might be used to produce gas selective nanodeposits on the nano/micropores of PS. These include short-term electron beam deposition and direct nanoparticle diffusion into the PS micropores so as to promote the required interaction with the nanopore covered PS micropores. An extension to the detection of several methamphetamine manufacture by-produces including PH_3 [55] , acetone [56], and benzene [57] (in addition to NH_3 [41,45] and HCl [41,45]) can be made possible using specially designed aluminum oxide (e-beam) or aluminosilicate nanostructured deposits [55], nickel (electroless) or zirconium oxide based (nanostructured ZrO_2 nanoshells [58] deposited into the micropores of PS) nanostructured surfaces [56], and nitrided titanium dioxide [57] ($TiO_{2-x}N_x$ [59,60]) nanostructure deposits. It is possible to extend the technology to a more expanded list of gases with the

development of a more general selective deposition technology based on the extrapolation of the concepts of hard and soft acids and bases set forth in the literature by R.G. Pearson and others [49]. By monitoring the trends in hard and soft acid and base behavior, first order selections for appropriate modifications of the PS hybrid interface with nanostructured metal/metal oxide deposits to create selectivity for a number of gases can be made. The development of selective nanostructured deposits that reversibly complex with a gas can be based on the combination of hard Lewis acids with soft Lewis bases and on the trends associated with the classification of the hard and soft nature of these acids and bases.

1.2 A Survey of Functional Semiconducting Metal Oxides for Gas Sensing

Conductometric metal oxide gas sensors depend on the resistance change caused by chemical interactions between a sensor surface and the surrounding gaseous environment. The gaseous environment is usually the atmospheric air mixed with one or more different types of toxic gases that needs to be detected by the sensor. The atmospheric air composition at 15 ^{0}C and a pressure of 1 atm is summarized in Table 1.2 [61]. Nitrogen which constitutes 78 % of atmospheric air turns out to be a good dilution and entrainment gas choice for testing experiments due to its inertness.

Table 1.2. Air composition at a temperature of 15 ^{0}C and a pressure of 1 atm.

Name	Symbol	Percent by Volume
Nitrogen	N_2	78.084%
Oxygen	O_2	20.9476%
Argon	Ar	0.934%
Carbon Dioxide	CO_2	0.0314%
Neon	Ne	0.001818%
Methane	CH_4	0.0002%
Helium	He	0.000524%
Krypton	Kr	0.000114%
Hydrogen	H_2	0.00005%
Xenon	Xe	0.0000087%

Semiconducting metal oxides may be classified into different categories with respect to their types, sizes or dimensionality. There are various types of semiconducting

metal oxides which have been reported for gas sensing applications. Some of the frequently researched ones are SnO_2, WO_3, ZnO, In_2O_3, Fe_2O_3, NiO, TiO_2, ZrO_2, Ga_2O_3 and CuO [62]. In addition, noble metals such as Pd, Pt, Au, Ag have been employed to improve selectivity and stability [63]. Most of the metal oxide nanocrystals used in sensor applications have dimensions lower than 100 nm. In terms of dimensionality, metal oxide nanoparticles/clusters are defined as zero dimensional. There has been ongoing research on nanowires which are classified as one dimensional. Most commercial applications involve two dimensional semiconducting films. Although nanowires have higher surface to volume ratios compared to films, it is difficult to achieve preferential growth on a substrate. One other cost effective method involves compressing metal oxide nanocrystals which are produced in powder form into thin or thick films to increase the reacting surface area and gas diffusivity.

Typical production and deposition methods for semiconducting materials for gas sensing include chemical vapor deposition, electroless plating, physical vapor deposition or forming powders produced using sol-gel methods. Chemical vapor deposition (CVD) is frequently used in the semiconductor industry to produce high quality films. Even though it is precise, it is more costly compared to other methods. Atomic layer deposition (ALD) is a thin film (~few Å) deposition technique which has been used more frequently in recent years in both research and industry (especially, thinner gate oxide growth of high-k materials such as HfO_2, Al_2O_3, and ZrO_2 required for making smaller transistors). In electroless plating, the reaction resulting in deposition is auto-catalytic without the need for an external electric current. Gold, nickel, and silver are popular choices for electroless plating baths for printed circuit boards, transistor headers, electrical connectors, diode leads, lamps and other electronic parts [64]. It is possible to control the film growth or the amount of nanoparticle deposition by adjusting the reaction temperature and immersion duration. Physical vapor deposition can be accomplished using either thermal evaporation or sputtering systems. In thermal evaporation, one or more materials are evaporated from crucibles by passing a high current through them or by methods like bombarding them with electron-beams. On the other hand, in sputtering, the target material which is to be deposited is bombarded by highly energetic particles and after a physical momentum exchange process between the target and an ion source or

a plasma, the target material is deposited onto a substrate. Both thermal evaporation and sputtering methods are utilized for thin film deposition in the semiconductor industry.

Zero and one dimensional metal oxide nanostructures are produced and deposited by another physical process called the vapor liquid solid (VLS) process which has become a popular research tool in the last decade for creating nanostructures of various morphologies such as nanowires, nanobelts, nanoods, nanorings, and nanocombs [63]. The nanoparticle/film growth setup for the VLS process consists of a high temperature furnace with a temperature gradient, a pressure controlled tube through which a carrier gas, usually an inert gas including nitrogen or argon, flows and a crucible in which the purified, primary ingredient is heated. The primary material, initially in solid form, is heated at elevated temperatures. As a result, the material generally liquefies as some atoms or molecules are liberated due to the liquid's vapor pressure. The inert, carrier gas aids the flow of the liberated material along the path of a temperature gradient as they solidify on colder zones in the tube. The morphology of the solidified particles depends on the temperature gradient, pressure and gas flow. The nanoparticles/nanowires collected from the colder zones can be used for sensor applications. Films composed of compressed nanocrystalline metal oxides can also be produced by sol-gel processes. The sol-gel process is a wet process which starts with a chemical solution (sol) which usually contains metals or metalloids that act as a precursor to form a network of particles (gel). For example, the starting ingredient for an SnO_2 sol-gel is usually $SnCl_4$. Controlled calcination yields crystals of varying grain sizes and it is possible to dope these nanocrystals with Pt and Pd [65].

Figure 1.10 shows a simplified schematic of a thin film sensor and a sensor which is composed of a collection of nanowires. A sensitive thin layer is deposited onto an insulating layer. A planar heating layer is formed at the bottom of the insulating layer to control the temperature of the sensor. A sensitive (semiconducting metal oxide) layer is coated onto the insulating layer by one of the processes discussed above. The interdigitated gold electrodes deposited onto the sensing layer are used to measure the conductivity response of the surface upon gas exposure. In Figure 1.10 (b), the sensitive layer of semiconducting thin film is replaced with semiconducting nanowires deposited

onto the interdigitated electrodes for electrical measurements. The controlled alignment of these wires on a surface is one of the biggest problems in nanowire research.

The sensitive parts of the gas sensors are usually made out of thin film materials. This layer must be thin enough so that interactions with the gaseous environment can alter the charge transport significantly. Semiconductors, in general, have a low number of charge carriers with respect to surface sites [66]. Although it is theoretically possible to replace the semiconducting layer with a very thin (few nm) metal layer for similar operation, it is not feasible for practical applications. Substrate materials on which to deposit the sensing layer are usually SiO_2 or Al_2O_3 because of their stability at high temperatures.

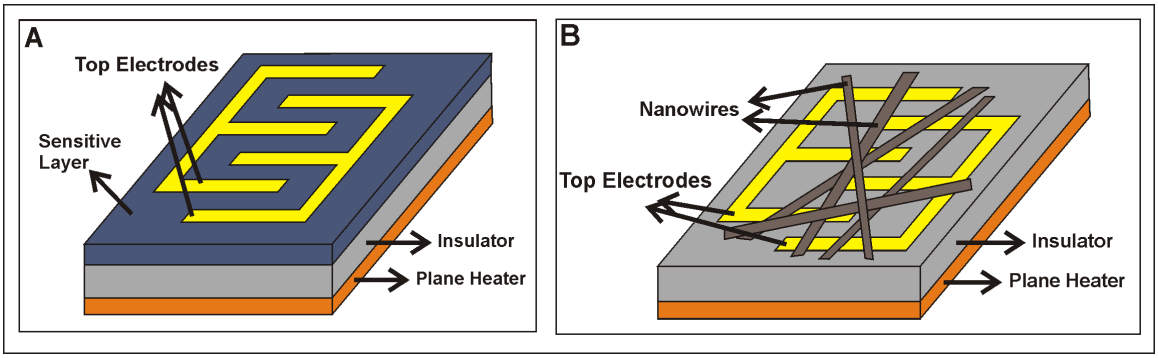

Figure 1.10. a) Schematic of a thin film sensor. The heating electrode is used to control the reaction temperature while the interdigitated electrodes are used to measure a response when a sensitive layer is exposed to a target gas. b) The sensitive layer of the semiconducting thin film is replaced with semiconducting nanowires deposited onto the interdigitated electrodes for electrical measurements.

1.2.1 Response Mechanisms

We can divide solid materials into three groups with respect to their bulk conductivity. Materials with conductivities smaller than 10^{-8} siemens per centimeter (S/cm) are called insulators. Materials with conductivities greater than 10^{3} S/cm are named conductors. The materials with conductivities roughly in between (10^{-8} S/cm < σ < 10^{3} S/cm) are semiconductors. In crystalline materials, charged carriers are allowed to have energies within certain ranges. The allowed energy levels form energy bands and are separated by band gaps. The highest energy level completely filled with electrons at 0 K is the valence band. The energy of the highest occupied electronic state at absolute temperature (0 K) corresponds to the Fermi energy, E_F. Valence electrons are bound to atoms. In contrast, the conduction electrons are free to move in the lattice. The next

excited state above the valence band is called the conduction band. We can also define a vacuum energy level that corresponds to the energy needed to free an electron from the crystal and a work function (Φ) which corresponds to the energy needed to remove and electron from the crystal at 0 K. The relationship between Φ, E_F, and E_{vac} are given in Equation 1.1. A simple schematic of the flat-band structure of a bulk semiconductor is depicted in Figure 1.11a.

$$e\Phi = E_{vac} - E_F \qquad \text{(Equation 1.1)}$$

When an electron gets excited to a higher energy state, the absence of an electron left behind is called a "hole". The occupation of the energy levels is governed by Fermi-Dirac statistics. Holes are effectively positively charged particles with an effective mass and mobility analogous to electrons. In metals, there is no energy gap between the valence and conduction band, as a result electrons can easily be excited to the conduction band and move in the crystal. In contrast, insulators have a large band gap and electron excitation to the conduction band doesn't occur easily at room temperature. At temperatures greater than 0 K, electrons can jump to the conduction band leaving holes behind in the valence band. Impurities, vacancies, interstitial atoms, dislocations, grain boundaries, and amorphous regions can cause imperfections in the crystal and this affects the number of electrons in the bands. It is also possible to add imperfections intentionally by doping the semiconductor. The type of dopants (donors or acceptors) may determine the type of majority carriers (electrons or holes). A semiconductor whose electrical properties are dominated by doping is called an extrinsic semiconductor as opposed to an intrinsic or pure semiconductor. In an n-type semiconductor, donor levels appear close to the conduction band. However, in a p-type semiconductor, the acceptor levels appear close to the valence band.

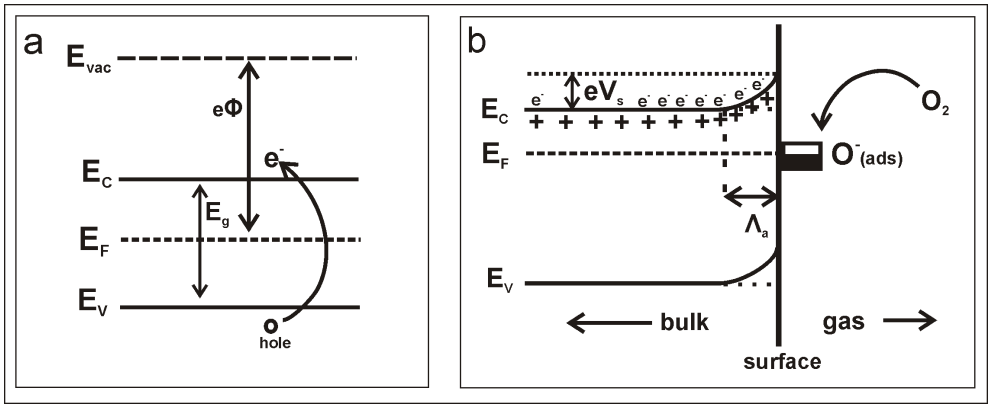

Figure 1.11 a) Simple schematic of the band diagram of a semiconductor. E_v, E_F, E_C, E_{vac}, E_g denote the energy of the valence band, Fermi level, conduction band, vacuum level and band gap and Φ represents the work function. At 0 K, the conduction band is completely empty and at higher temperatures, electrons can jump to the conduction band leaving holes in the valence band. b) A simplified model of band bending at the surface of an n-type semiconductor is illustrated. Λ_a denotes the thickness of the space charge layer and eV_s denotes the potential barrier formed in the space charge region. The Fermi energy has the same value everywhere in the material. As a result of the surface charges accumulated on the surface due to gas adsorption, the bands bend close to the surface to keep the Fermi energy constant. [adapted from Ref. [67]]

The response of most semiconducting gas sensors is based on the change of the number of electrons in the conduction band after a solid gas interaction and its measurable affect on the resistance of the semiconductor. The surface is where the crystal periodicity is interrupted and this enables localized energy levels in the forbidden gap region. The energy levels available on the surface are called surface states [68]. These states can capture or give up electrons. They might arise from surface defects or adsorbed impurity atoms. They behave like traps for electrons. Conduction band or donor level electrons prefer to flow to the low-energy surface states residing in the band gap. As a result, the Fermi energy at the surface decreases and the electronic energy on the surface increases. The Fermi energy has to have the same value everywhere in the material under equilibrium conditions. As a result of the surface charge accumulation, valence and conduction bands bend close to the surface to keep the Fermi energy level constant everywhere. Figure 1.11 (b) illustrates the band bending of an n-type semiconductor [67]. In Figure 1.11 (b), the donor electrons move to the surface and take part in adsorbing oxygen onto the surface. This process forms a space charge region where positively charged donor atoms are on one side and negatively charged surface states on the other. This region is depleted of charges and Λ_a denotes the thickness of the

depletion region. The potential barrier formed on the surface due to the space-charge region is denoted as eV_s. The height and depth of the bending depends on the surface charge. The Debye Length (L_D) is another parameter that affects the thickness of the depletion region (Equation 1.2). L_D is a measure of the electrostatic screening in a semiconductor. It depends on the dielectric permittivity (ε), Boltzmann constant (k_B), temperature (T), electron charge (e) and carrier concentration (n_d) [5].

$$L_D = \sqrt{\frac{\varepsilon_0 \varepsilon k_B T}{e^2 n_d}} \qquad \text{Equation 1.2}$$

The conductivity of the surface has an Arrhenius type dependence on the potential barrier (eV_s) [5] (Equation 1.3).

$$\sigma(T) \sim \exp(\frac{-eV_s}{k_B T}) \qquad \text{Equation 1.3}$$

Metal oxide gas sensors also known as chemiresistors are typically operated between 200 ^{0}C and 500 ^{0}C where conduction is electronic and oxygen vacancies are doubly ionized [63]. Oxygen and water vapor are the most reactive constituents of air. When oxygen oxidizes a material, it attracts electrons from the surface of the material and becomes a tightly bound ion at the surface (Figure 1.12(a)). This changes the number of electrons, which are free to move, that are available for the material. Some gases are not easily adsorbed by the clean surface of the sensing layer, but instead interact with the already adsorbed species on the surface. In Figure 1.12, a schematic of an n-type semiconducting metal oxide film (e.g. SnO_2) has been depicted. The oxygen molecules in the air are adsorbed onto the surface as molecular (O_2^-) and atomic (O^- and O^{--}) species. The chemisorption of oxygen onto an n-type semiconductor surface leads to the trapping of more electrons from the conduction band and a higher surface resistance. In a p-type semiconductor, the same process leads to a higher conductance. Infrared (IR) analysis have shown that molecular ionosorption decreases and atomic ionosorption increases as the temperature increases above 150 ^{0}C for SnO_2 surfaces. This is due to a higher activation energy needed for atomic formation [65]. This energy is supplied by heat at high temperatures. The operation range for such sensors could be as wide as 100 ^{0}C to 500 ^{0}C. When ionosorption occurs, the metal oxide film contributes an electron to the process leading to a depletion layer at the surface of the metal oxide film. In Figure 1.12

b, a schematic of the interaction with a reducing gas of a typical surface is depicted. The presence of gases with reducing or oxidizing properties will affect the surface charge density close to the surface of the film (or grain). When the surface is exposed to a reducing gas (e.g. CO), the reducing gas reacts with the pre-adsorbed oxygen on the surface releasing electrons back to the surface (Equations 1.4 and 1.5). However, an oxidizing gas (e.g. NO_2) will trap more free conduction electrons from the surface due to its high electronegativity and the thickness of the depletion layer increases accordingly (Equations 1.6 and 1.7). Operating at higher temperatures is believed to decrease the effects of humidity fluctuations and may also induce the creation of oxygen vacancies (Vo) as indicated in Equation 1.8. In most cases, resistance measurements are carried out on such a surface to quantify the amount of the reacting gas by applying a DC current onto the surface. Other response measurement methods include work functions, mobilities, temperature changes, and catalytic activity on the surface.

$CO\ (gas) \rightarrow CO\ (ads)$ Equation 1.4

$CO\ (ads) + O^-\ (ads) \rightarrow CO_2\ (gas) + e^-$ Equation 1.5

$NO_2\ (gas) \rightarrow NO_2\ (ads)$ Equation 1.6

$e^- + NO_2\ (ads) \rightarrow NO_2^-\ (ads)$ Equation 1.7

$O^{2-}\ (ads) \rightarrow 1/2O_2\ (gas) + Vo$ Equation 1.8

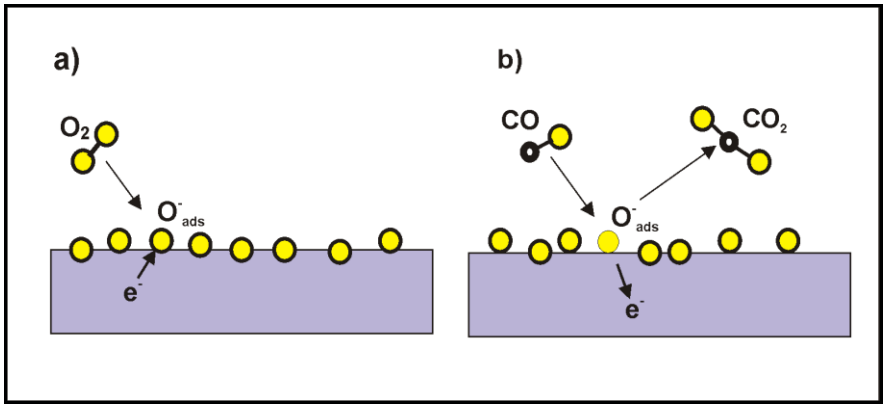

Figure 1.12. a) Schematic representation of oxygen adsorption from the gas phase on a semiconducting film surface (n-type). b) Interaction with a reducing gas (CO) removes chemisorbed oxygen from the surface releasing electrons back to the film.

1.2.2 Important Parameters

Polycrystalline films can be formed by compressing nanocrystalline grains of semiconducting oxides. The structural parameters are grain size and agglomeration, pore size and film morphology. Crystallite size is an important parameter which determines the number of surface and bulk states. A low grain size imposes a high ratio of surface trapping states to bulk states and the response strength of the surface is proportional to this ratio upon exposure to a target gas. The shape of the grains or powders may also be an important parameter associated with sensing properties. Conventional sol-gel synthesis techniques usually yield spherical particles. Physical vapor deposition techniques may result in cylindrical 1D nanowires. The surface area to volume (Sa:V) ratio of a spherical particle is 3/R where R is the radius of the spherical particle. When we calculate the Sa:V ratio of a cylindrical wire with the same radius R and length L, the result is 2(R+L)/RL. If we compare the two calculated Sa:V ratios for two different shapes, their ratio is 3L/2(R+L). This final result shows us that for the same amount of material, as L is much larger than R, we always get a larger Sa:V ratio for spheres. When L is comparable to R, the cylindrical shape becomes favorable in terms of surface area. Larger surface area means more interaction surface and a higher response as well as faster response and recovery times for a gas sensor. Film thickness and porosity of the film are significant factors for analyte diffusion. A thinner and high porosity film facilitates faster response and recovery. Another way to gain a faster response time scales is to use 1D metal oxide structures such as wires, rods, belts, and tubes. 1D structures have more reactive surface area than 2D structures.

Bulk properties such as the doping type and concentration, and the mobility of the carriers are important electronic parameters. Adding catalytically active sites onto the surface by introducing additional metals/oxides is another way of doping a sensitive layer. The properties of additional catalytic particles such as noble metals on the surface will change the surface states and electronic structure as well. Beyond the depletion region, interior parts of the grains do not contribute to the response. The thickness of the space charge region formed on the surface and the height of the potential barrier (Figure 1.11 (b)) are also important constraints. A critical grain size may result in fully depleted surfaces. Producing smaller grains down to this critical dimension leads to larger

responses per grain [5]. On the other hand, sensors composed of nanocrystalline metal oxide grains/particles may suffer from poor interconnectivity between grains if the grain size shrinks too much. Furthermore, a smaller grain/particle size may cause substantial increase in the contribution of impurities and defects to the response. Although there is a wealth of experimental data, there is no well developed model to optimize either grain or particle size grain/particle size to achieve higher responses in any type of metal oxide sensor.

The ambient conditions where measurements are done can affect the sensor response as well. The amount of humidity in the environment is considered to be an important factor. The surface of the sensitive layer is covered with OH^- groups under humid conditions. These OH^- groups can interact with the target gas and alter the response. The operating temperature changes the amount of water in the ambient air as well as the chemisorption rate of the target analyte. In most cases, the target gas is mixed with other reducing or oxidizing gases which react with the sensitive layer. The unwanted adsorption of gases other than the target gas onto the sensor can influence the reproducibility of the response due to cross correlations.

Although the amount of data, mostly empirical, on a wide range of metal oxides continues to increase every year, unifying simple mechanisms that can provide a basic scientific understanding of metal oxide sensor operation, and transduction for various environments are not well understood. The selectivity of the metal oxide surfaces may be adjusted by varying a number of parameters such as crystal structure and morphology, dopants, surface geometries, modes of operation, gas pressure and temperature.

1.2.3 Solid Gas Interactions: Physisorption and Chemisorption

The interaction between a surface and an adsorbent can be either physical (physisoption) or chemical (chemisorption). The transition from physisorption to chemisorption is continuous and at some instances it is not easy to distinguish the difference between the two regimes. Physisorption is a weaker interaction and can involve a weak bonding or surface polarization (dipole-dipole interaction) rather than a charge exchange between surface and the adsorbate. Any molecule approaching the surface can polarize and induce a dipole on the surface. The typical binding energy for a

dipole-dipole interaction is 0.1-0.12 eV [69]. Gas molecules can condense on a surface at low temperature which results in physisorption. The heat of adsorption for physisorption is roughly less than 6 kcal/mol compared to greater than 15 kcal/mol for chemisorption [69]. Physisorption is usually not directional, independent of the surface atom orientations and more uniform across a substrate [70]. On the other hand, chemisorbed molecules interact more strongly with the substrate surface or already chemisorbed species on the surface and usually form new molecules.

Figure 1.13 shows a Lennard-Jones model of physisorption and chemisorption [Adapted from Ref-69]. The dashed line represents the system energy of physisorption with respect to the separation distance (d) between a surface and the physisorbed species. At infinity, the system energy goes to zero. As the separation decreases, the dipole/dipole attraction grows up to a critical value and after a critical separation, the surface and adsorbate begin to repel each other. The solid line in Figure 1.13 represents the chemical interaction between a surface and an adsorbate. Far away from the surface, the total energy is positive due to molecular bonds of the gas species. When a gas molecule is close to the surface, it partially dissociate and chemical bonds between the surface and gas atoms start to form. ΔEc, and ΔEp represent the heat of chemisorption, and heat of physisorption. ΔEc is usually considerably higher than ΔEp.

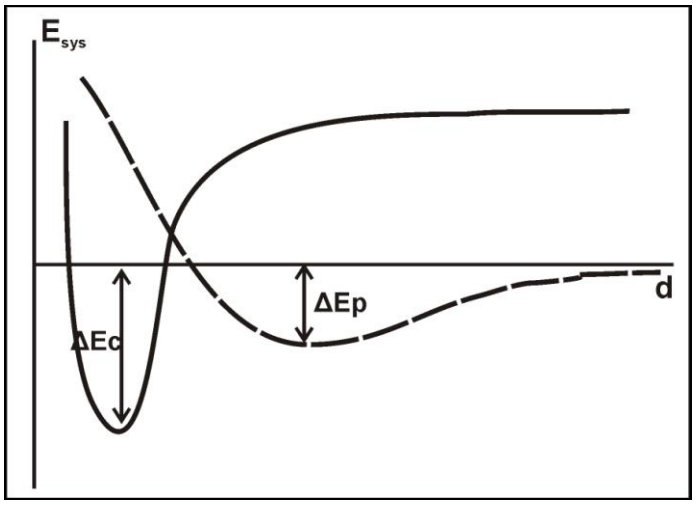

Figure 1.13. [Adapted from Ref. 69] The dashed line represents the system energy variation of physisorbed particle and a surface with respect to their separation distance. Similarly, the solid line represents the chemisorption energy. ΔEc, and ΔEp represent heat of chemisorption, and heat of physisorption.

1.2.4 Semiconducting Metal Oxides of Interest

Noble metals are highly effective oxidation catalysts. Many types of noble metals have been used to dope sensitive metal oxide layers to adjust sensitivity. Pd and Pt are the most commonly used noble metal additives to SnO_2 films. Impregnation, sol-gel methods, sputtering, and thermal evaporation have been used to add noble metals into metal oxide sensitive layers [71]. O^- adsorbed on the semiconducting oxides is more active then adsorbed O_2^-. Although the exact mechanism is not well understood, noble metals such as Pd are believed to increase O_2^- dissociation and traps on the Pd surface. Noble metals also increase the surface activity of metal oxides in redox processes. Although there are various types of semiconducting metal oxides available for sensing applications, NiO, CuO, SnO_2, Al_2O_3, ZrO_2, and TiO_2 nanoparticles on PS have been researched more extensively in our group because of the know-how accumulated about producing these particles.

Ultra thin nickel oxide (NiO_x) films produced by molecular beam epitaxy (MBE) on silicon substrates have been reported for sensing H_2, NH_3, NO_2, SO_2, and CO. The measurements were done at 30 ^{0}C for detecting 100 ppm of target gas and the method of measurement was through variations in DC conductivity [62,72]. At 450 ^{0}C, NiO is used for detecting H_2, CO_2 and O_2 below 10 % concentration [62,73]. NiO shows a rocksalt structure and, at Ni vacancies on the surface, O atoms can react with reducing gases and release electrons to the NiO film. Briquet, et.al. showed that Ni (111) nanoparticles supported on α-Al_2O_3 can adsorb CO at a metal-metal oxide interface based on density functional theory (DFT) investigations presented in a recent research paper [74]. Doping NiO thin films with noble metals to detect CH_4 at high concentrations (10000 ppm) has also been reported in the literature [74].

Typically copper oxide (CuO) behaves like a p type semiconductor. Jernigan et. al. studied CO oxidation on different oxidation states of copper; metallic copper, copper (I) oxide and copper (II) oxide and found that the oxidation rate at 300 ^{0}C is in the order Cu(0)>Cu(I)>Cu(II) [75]. Chowdhuri et al used CuO nanoparticles deposited on sputtered a sputtered thin (90 nm) SnO_2 film to detect H_2S. CuO nanoparticles deposited on the SnO_2 film allow removal of excess adsorbed oxygen from the uncovered SnO_2 surface leading to an easier hydrogen dissociation from the H_2S–CuO interaction [76].

SnO_2-CuO mixtures can be screen-printed onto substrates for sensor applications instead of using microfabrication process methods which increase costs. ZnO heterojunctions of doped and undoped layers with CuO have been shown to detect CO and CO_2 [77].

SnO_2 is the most studied material for gas sensing application because of its stability and durability, especially at high temperatures. However, it has poor selectivity. Pure SnO_2 is a semiconductor with a band gap of 3.6 eV. There have been many attempts to improve the selectivity of SnO_2 by doping it with other metal oxides and noble metals. SnO_2 has been used to detect H_2 (25 to 650 ^{0}C), C_2H_5OH (25 to 500 ^{0}C), CO (131 to 570 ^{0}C), NO_x (131 to 525 ^{0}C), CH_4 (200 to 320 ^{0}C), SO_2 (200 to 500 ^{0}C), H_2S (300 to 450 ^{0}C), and CO_2 (450 to 500 ^{0}C) [62]. Various structures of SnO_2 have been employed for this purpose. Comini et. al. reported single crystalline SnO_2 nanobelts for detection of CO, NO_2 and ethanol at 400 ^{0}C [78]. Kolmakov et al. used SnO_2 nanowires to detect CO in an O_2 background at 250 ^{0}C [79]. A comprehensive overview of SnO_2 sensing is presented in Reference-62.

Titania (TiO_2) is another semiconducting oxide which has been researched thoroughly especially for photocatalysis and solar cell applications. TiO_2 thin films prepared by sol-gel methods were employed by Comini et. al. to detect 100 ppm of ethanol and methanol at 400 and 500 ^{0}C [80]. Kim et. al used TiO_2 nanofiber (dimaters of 200-500 nm) networks to detect NO_2 (500 ppb) at 300 ^{0}C and showed a nanofiber response to CO, H_2 and CH_4 at ppm levels [81]. Ferroni et. al. managed to detect 20 ppm NO_2 with nanosized TiO_2 films at 600 ^{0}C and studied the stability and reproducibility of the response from such thin films [82]. Yates studied the NO chemisorption of on TiO_2 powders under UV radiation over a wide range of temperatures 100-1500 ^{0}C [83]. The detection of 500 ppm of NH_3 at an operating temperature of 250 ^{0}C with TiO_2 thin films has also been reported [84].

Porous anodic alumina (Al_2O_3) is used for humidity detection at room temperature with good stability. Nahar et. al. reported a detection range of 3 % to 98 % humidity [85] using capacitance and resistance measurements. Seiyama et. al. reported H_2 (9%), O_2 (9%), and CO_2 (2.1 %) detection at 450 ^{0}C using an alumina thin film on silica substrates [86].

Zirconia (ZrO_2) sensors have been used to detect a variety of gases, but they are mostly known for O_2 detection in internal combustion engines in automobiles [87]. Yttria (Y_2O_3) and ZrO_2 are two examples of solid electrolytes used in sensor applications. In solid electrolytes, the conductivity is ionic rather than electronic. In a solid electrolyte gas sensor, two types of solid electrolytes (Y_2O_3 and ZrO_2) are connected with a membrane through which ions can move freely. When one side of the membrane is exposed to chemical species, ions (O^{2-}) move from one side of the membrane to the other to compensate the chemical interaction. By measuring the voltage difference between the separated regions at steady state, it is possible to determine the concentration of the chemical species [88]. The Yamazoe group achieved a 1-100 ppm Cl_2 detection in a dry, O_2 containing air background at 550-650 ^{0}C [89]. A 5 % H_2 in N_2 background has been detected using a ZrO_2 electrochemical cell at 450 ^{0}C [97].

Some of the metal oxides sensors discussed above are summarized in Table 1.3 with their structural forms, target gases, detection limits, and operating temperatures. The mechanisms for gas sensing for each type of metal oxide is not fully understood. A better description of the sensing mechanism and a way to correlate target gas and the most suitable type of metal oxide for sensing the target analyte is desirable.

Table 1.3. Selected metal oxides for sensing applications. The structure, test gas, detection limit, and operating temperature are given in the table. (Emc is short for Electrochemical Cell).

MATERIAL	GAS	FORM	T (^{0}C)	DETECTION	REF
NiO	H_2	Film	600	500-10k ppm	90
Ni/MgO	NO	Clusters	600		91
NiO	H_2 NH_3 NO_2 SO_2 CO	Film	30	10 %	62,72
CuO	CO	Clusters	300		75
CuO/SnO_2	H_2S	Clusters	100	5-100 ppm	76
CuO	H_2 CO_2 O_2	Film	450	<9%	86
SnO_2	CO NO_2 Ethanol	Nanobelts	400	250 ppm 0.5 ppm 250 ppm	78
SnO_2	CO in 10 % O_2	Nanobelts	200-300	0.6 %	79
SnO_2	NO_2 CO	Thick Films	136-312	10-25 ppb 1-20 ppm	62,92
SnO_2	H_2S NO_2	Thin Film	300-400	0-9 ppm	62,93
SnO_2	SO_2	Powder	200-500		63,94
SnO_2 (Pt,In,Au)	NO_x CO	Thin Film	200-400	2-70 ppm 50-1000 ppm	62,95
TiO_2	Ethanol Methanol	Thin Film	400-500	100 ppm	80
TiO_2	NO_2 CO H_2 CH_4	Nanofibers	300	0.5-12.5 ppm ~ppm	81
TiO_2	NO_2	Thin Film	600	20 ppm	82
TiO_2	NH_3	Thin Film	250	500 ppm	84
Al_2O_3	Humidity	Porous Film	Room Temperature	3-98%	85
Al_2O_3	H_2 CO_2 O_2	Thin Film	450	9 % 9 % 2.1 %	62.86
ZrO_2	O_2	Disk in Emc	253		62,96
ZrO_2	Cl_2	Disk in Emc	550-650	1-100 ppm	89
ZrO_2-Y_2O_3	H_2 in N_2	Disk in Emc	450	5 %	97
ZrO_2-Y_2O_3	SO_2	Disk in Emc	600	100 ppm	98

1.3 Commercial Gas Sensors

There is a huge market for low cost, reliable, sensitive gas sensors in mines, chemical industries, the oil industry, the semiconductor industry, the aerospace industry, homes, cars, and hospitals. The dominant types of sensors in the market are currently Taguchi-type sensors (eg. Figaro Inc. from Japan) [99]. Taguchi introduced a semiconductor based gas sensor for hydrocarbon detection in 1968. At the time, most popular sensors were catalytic bead sensors which are poisoned frequently and lose sensitivity in time.

The commercial metal oxide sensors are usually prepared from compressed powder or paste that is deposited onto an insulating layer (e.g. alumina or silica). Since the response of the metal oxide layer may vary with temperature, a heating layer (e.g. a thin layer of platinum or a resistive metal oxide) is deposited onto the back of the insulating layer to control the temperature of the sensitive layer. It is also possible to use filter combinations in front of industrial sensors to avoid responses from superfluous background gases. A popular example is charcoal to remove organic volatiles and water. Some of the commercially available metal oxide sensors use charcoal as a filter in front of CO sensors [100]. Zeolites and porous alumina and silica are also used as filter materials.

Commercial sensors can detect various gases in various concentration ranges. This allows them to be used in many different applications. On the other hand, most metal oxides suffer from selectivity problems and interferences from other gases may contribute immensely to this factor. They need to be operated at different temperature ranges for differing target gases. Temperature is an important factor in the reproducibility of the sensor response. Furthermore, when a flammable gas needs to be detected, the operating temperature of the sensor has to be below the ignition temperature at which ignition will take place without a spark or a flame. The accuracy of the response can fluctuate 10-20 % due to the partial pressure of interfering gases. The gradual drift of response in time may cause a need for frequent recalibration in some applications (e.g. breath analyzers). One of the advantages of metal oxide sensors is that no sensor material is consumed in the sensing process and metal oxide sensors have a long life expectancy. The life expectancy of some sensors may be as long as 10+ years.

A good approach to improve the selectivity of a sensor is to use sensor arrays. Since metal oxides operate at various temperatures for the optimum response to a given gas, forming an array in the same package can influence cross sensitivities. There is also a problem of lack of compatibility with integrated circuit (IC) technologies to form smart sensors because ICs are built on silicon. Uniting receptor and transduction functions with electronic components on a single substrate is not yet possible.

Toxic gases are poisonous and can be life threatening at high concentrations or for long term exposures. Most toxic gases need to be detected at ppm or ppb levels. The Occupational Safety and Health Administration (OSHA) publishes legal standards of toxic gases acceptable at work places. An extensive list of toxic gases with OSHA work place permissible exposure limits (PEL) and the equivalent UK legal standard, EH40/2005 short and long term work place exposure limits (WEL), is given in a table in Appendix I. [Adapted from Ref. 101]. Some gases of interest and their PEL and WEL levels are summarized in Table 1.4.

Table 1.4. EH40 and OSHA standards for the work place. Gas data is supplied where known [Adapted from Ref 101].

Name	Formula	EH40 WEL (Long)	EH40 WEL (Short)	OSHA (PEL)
Ammonia	NH_3	25 ppm	35 ppm	50 ppm
Phosphine	PH_3		0.3 ppm	0.3 ppm
Nitric Oxide	NO			25 ppm
Nitrogen Dioxide	NO_2			5 ppm
Sulfur Dioxide	SO_2			5 ppm
Hydrogen Sulfide	H_2S	5 ppm	10 ppm	20 ppm
Carbon Monoxide	CO	30 ppm	200 ppm	50 ppm

1.4 Motivation

Porous silicon (PS) stands out as an excellent platform for gas sensing applications. Hybrid porous silicon gas sensors display the advantage of operation at room temperature as well as at a single, readily accessible, temperature with an insensitivity to temperature drift; operation in a heat-sunk configuration with a surface temperature up to 80°C even in highly elevated temperature environments, in sharp contrast to metal oxide sensors; ease of coating with gas-selective materials; low cost of

fabrication and operation, and the ability to rapidly assess false positives by operating the sensor in a pulsed mode. Surface functionalization can be accomplished by metal oxide nanoparticle/cluster depositions and the sensitivity of the surface can be tuned to achieve maximum response for various gases. It is easy to form an array of PS sensors to detect toxic gases even in interfering backgrounds. The operation at room temperature makes it possible to form a sensor array in the same package and moreover saves power for mobile applications. Another big advantage over metal oxide gas sensors is that an integrated electronic monitoring system can be implemented on the same substrate as the receptor function in order to form smart sensor systems. PS is easily machinable with microfabrication techniques in comparison with many metal oxide gas sensor substrates.

From a scientific point of view, PS is a good platform to study the interaction of metal oxide nanoparticles/clusters and toxic gases. There has been an ongoing research to understand the sensing properties of one dimensional and two dimensional metal oxide nanostructures. However, it is not easy to build platforms to study zero dimensional systems because of size limitations. Nevertheless, it is possible to understand these interactions by studying the effects of various nanoparticle depositions on a PS network.

1.5 References

[1] http://en.wikipedia.org/wiki/Gas_leak_detection (Last Accesed on March 8th, 2011).

[2] Persaud, K. C.; Dodd, G. Nature, 299, 352 (1982).

[3] Frank Röck, Nicolae Barsan, and Udo Weimar "Electronic Nose: Current Status and Future Trends" Chem. Rev., 108 (2), pp 705–725 (2008).

[4] Seiyama, T.; Kato, A.; Fujiishi, K.; Nagatani, M. "A new detector for gaseous components using semiconductive thin films", Anal. Chem., 34, 1502–1503 (1962).

[5] M. E. Franke, T. J. Koplin, U. Simon, Small, 2, 36 (2006).

[6] Francia DG, Ferrara LV, Manzo S, Chiavarini S. "Towards a label free optical porous silicon DNA sensor", Biosense Bioelectron., 21, 661-5 (2005).

[7] Rendina I, Rea I, Rotiroti L, Stefano DL. "Porous silicon-based optical biosensors and biochips", Physica E., 38:188-92 (2007).

[8] Benilov A, Cabrera M, Skryshevsky V, Martin JR. "Porous silicon localization for implementation in matrix biosensors" Mat Sci Eng B-Solid,139, 221-5 (2007).

[9] Pagonis DN, Petropoulos A, Kaltsas G, Nassiopoulou AG, Tserepi A. “Novel microfluidic flow sensor based on a microchannel capped by porous silicon” Phys Stat Sol A, 204, 1474-9 (2007).

[10] Pramanik C, Saha H, Gangopadhyay U. “An integrated pressure and temperature sensor based on nanocrystalline porous silicon.” J Micromech Microeng,16,1340-8 (2006).

[11] Granitzer P, Rumpf K, Krenn H. “Ferromagnetic nanostructures incorporated in quasi-one-dimensional porous silicon channels suitable for magnetic sensor applications. J Nanomaterials” 2006, 1-7 (2006).

[12] Belkacem W, Mliki N, Belhi R, Saikaly, Yangui. “Nanostructures cobalt on porous silicon substrate: structure and magnetic behaviour”, Phys Stat Sol A, 204, 3321-32 (2007).

[13] Mery E. Alekseev SA, Zaitsev VN, Barbier D. “Covalent grafting ion-exchange groups on porous silicon for Microsystems applications”, Sens Actuators B: Chem., 126, 120-5 (2007).

[14] Gole JL, Lewis S. Porous silicon- sensors and future applications. In: Kumar V, editor, Nanosilicon, Elsevier, 149-75 (2007).

[15] Björkqvist M, Salonen J, Paski J, Laine E. “Characterization of thermally carbonized porous silicon humidity sensor”, Sens Actuators A: Phys., 112, 244-7 (2004).

[16] Rittersma ZM, Splinter S, Bödecker, Bnecke W. “A novel surface-micromachined capacitive porous silicon humidity sensor”, Sens Actuators B: Chem, 68, 210-7 (2000).

[17] Foucaran A, Sorli B, Garcia M, Pascal--Delannoy F, Giani A, Boyer A. “Porous silicon layer coupled with thermoelectric cooler: a humidity sensor”, Sens Actuators A: Phys, 79, 189-93 (2000).

[18] Björkqvist M, Salonen J, Laine E, Niinistö L. “Comparison of stabilizing treatments on porous silicon sensor applications”, Phys Stat Sol A, 182, 123-6 (2000).

[19] Björkqvist M, Paski J, Salonen J, Lehto V, “Studies on the hysteresis reduction in thermally carbonized porous silicon humidity sensor”, IEEE Sense J, 6, 542-7 (2007).

[20] Salgado GG, Becerril DT, Santiesteban JH, Andres ER. “Porous silicon organic vapor sensors”, Opt Mater., 29, 51-5 (2006).

[21] Barillaro G, Diligenti A, Marola G, Strambini LM. “A silicon crystalline resistor with an adsorbing porous layer as gas sensor” Sens Actuators B: Chem.,105, 278-82 (2005).

[22] Iraji zad A, Rahimi F, Chavoshi M, Ahadian MM. “Characterization of porous poly--silicon as a gas sensor” Sens Actuators B: Chem,100, 341-6 (2004).

[23] Archer M, Christophersen M, Fauchet PM. “Electrical porous silicon chemical sensor for detection of organic solvents” Sens Actuators B: Chem,106, 347-57 (2005).

[24] Dorvee J, Sailor MJ. “A low--power sensor for volatile organic compounds based on porous silicon photonic crystals”, Phys Stat Sol A, 202, 1619-23 (2005).

[25] King HB, Ruminski AM, Snyder JL, Sailor MJ. “Optical fiber mounted porous silicon photonic crystals for sensing organic vapor breakthrough in activated carbon”, Adv Mater.,19, 4530-4 (2007).

[26] Rocchia M, Rossi AM, Zeppa G. “Determination of ethanol content in wine through a porous silicon oxide microcavity” Sens Actuators B: Chem,123, 89-93 (2007).

[27] Stefano LD, Alfieri D, Rea I, Rotiroti L, Malecki K, Moretti L, Corte FGD, Rendina I. “An integrated pressure--driven microsystem based on porous silicon for optical monitoring of gaseous and liquid substances” Phys Stat Sol A, 204, 1459-63 (2007).

[28] Vrkoslav V, Jelinek I, Trojan T, Jindrich J. Dian J. “Porous silicon with β-cyclodextrin modified surface photoluminescence sensing of organic molecules in gas and liquid phase”, Physica E, 38, 200-4 (2007).

[29] Rahimi F, Iraji zad A, Razi F. “Characterization of porous poly-silicon impregnated with Pd as a hydrogen sensor”, J Phys D: Appl Phys, 38, 36-40 (2005).

[30] Rahimi F, Iraji zad A. “Characterization of Pd nanoparticle dispersed over porous silicon as a hydrogen sensor” J Phys D: Appl Phys, 40, 7201-9 (2007).

[31] Arakelyan VM, Galstyan VE, Martirosyan KS, Shahnazaryan GE, Aroutiounian VM, Soukiassian PG. “Hydrogen sensitive gas sensor based on porous silicon/TiO_{2-x} structure” Physica E, 38, 219-221 (2007).

[32] Mahmoudi Be, Gabouse N, Haddadi M, Mahmoudi Br, Cheraga H, Beldjilali K, Dahmane D. “The effect of annealing on the sensing properties of porous silicon gas sensors: use of screen-printed contacts”, Sens Actuators B: Chem,123, 680-4 (2007).

[33] Mahmoudi Be, Gabouse N, Guerbous L, Haddadi M, Cheraga H, Beldjilali K. “Photoluminescence response of gas sensor based on CH_x/porous silicon-effect of annealing treatment”, Mat Sci Eng B-Solid, 138, 293-7 (2007).

[34] Gabouse N, Belhousse S, Cheraga H, Ghellai H, Ouadah Y, Belkacem Y, Keffous A. “CO_2 and H_2 detection with a CH_x/porous silicon-based sensor”, Vacuum, 80, 986-9 (2006).

[35] Boarino L, Baratto C, Geobaldo F, Amato G, Comini E, Rossi AM, Faglia G, Lerondel G, Sberveglieri G. "NO_2 monitoring at room temperature by a porous silicon sensor" Mat Sci Eng B-Solid, 69-70 (2000).

[36] Baratto C, Faglia G, Comini E, Sberveglieri G, Taroni A, Ferrara VL, Quercia L, Francia GD. "A novel porous silicon sensor for detection of sub-ppm NO_2 concentrations", Sens Actuators B: Chem, 77, 62-6 (2001).

[37] Massera E, Nasti I, Quercia L, Rea I, Francia GD. "Improvement of stability and recovery time in porous-silicon based NO_2 sensor", Sens Actuators B: Chem,102,195-7 (2004).

[38] Pancheri L, Oton CJ, Gaburro Z, Soncini G, Pavesi L. "Very sensitive porous silicon NO_2 sensor", Sens Actuators B: Chem, 89, 237-9 (2003).

[39] Chakane S, Gokarna A, Bhoraskar SV. "Metallophthalocyanine coated porous silicon gas sensor selective to NO_2", Sens Actuators B: Chem, 92, 1-5 (2003).

[40] Subramanian NS, Sabaapathy V, Vickraman, Kumar GV, Sriram R, Santhi B. "Investigations on Pd:SnO_2/porous silicon structures for sensing LPG and NO_2 gas. Ionics" 13, 323-8 (2007).

[41] Lewis S, DeBoer J, Gole JL, Hesketh P. "Sensitive, selective, and analytical improvements to a porous silicon gas sensor", Sens Actuators B: Chem, 110, 54-65 (2005).

[42] Gole JL, Lewis S, Lee S. "Nanostructures and porous silicon: activity at interfaces in sensors and photocatalytic reactors", Phys Stat Sol A, 204, 1417-22 (2007) and references therein.

[43] Gole JL, Fedorov A, Hesketh P, Burda C. "From nanostructures to porous silicon: sensors and photocatalytic reactors", Phys Stat Sol C, 1, 188-97 (2004).

[44a] Gole JL, Seals LT, Lillehei PT. "Patterned metallization of porous silicon from electroless solution for direct electrical contact", J Electrochem Soc, 147, 3785-9 (2000).

[44b] Gole JL, Seals LT, DeVincentis JA, Lillhei PT, Prokes SM, Dixon DA. "Chloride salt enhancement and stabilization of the photoluminescence for a porous silicon surface", Phys Rev B, 61, 5615 (2000).

[44c] Gole JL. "Photoluminescence induced metallization for low resistance contacts." Tech Adv, Invited, MRS Bulletin, 28, 263 (2003).

[45] Seals L, Tse LA, Hesketh PJ, Gole JL. "Rapid, reversible, sensitive porous silicon gas sensor", J Appl Phys, 91, 2519-2523 (2002).

[46] Pearson RG. “Hard and soft acids and bases--the evolution of a chemical concept”, Coordin Chem Rev, 100, 403-25 (1990).

[47] Albert KJ, Lewis NS, Shauer CL, Sotzing GA, Sitizel SE, Vaid TP,Walt DA. “Cross-reactive chemical sensor arrays”, Chem Rev, 100, 2595-2626 (2000).

[48] Kwon CW, Poquet A, Mornet S, Campet G, Deliville MH, Treguer M, Portier J. “Electronegativity and chemical hardness: two helpful concepts for understanding oxide nanochemistry” Mater Lett, 51, 402-403 (2001).

[49] Gole JL. A General Approach to Creating Selective Metal Coatings at a Nano-microporous Porous Silicon Interface for Sensor Applications. Continuation in part; Patent Applied for, (2006).

[50] Lewis SE, DeBoer JR, Gole JL. “A pulsed system frequency analysis for device characterization and experimental design”, Sensor Actuator B: Chem,122, 20-29 (2007).

[51] Foucaran A, Pascalk-Delannoy F, Giani A, Sackda A, Comette P, Boyer A. “Porous silicon layers used for gas sensor applications”, Thin Sol Films, 297, 317 (1997).

[52] Moseley PT. Solid State Gas Sensors. Meas Sci Technol, 8, 223 (1997).

[53] Schechter I, Ben-Chorin M, Kuz A. “Sensitive, selective and tunable nanostructure modified porous silicon gas sensor”, Anal Chem, 67, 3727 (1995).

[54] (a)Schlesinger M, Paunovic M. Modern Electroplating, 4th edn., New York, John Wiley and Sons, 2000; (b) Fundamentals of Electrochemical Deposition, 2nd edn. New York, Wiley, 2006.

[55] Weller GL, Pratt SJ. Measuring phosphine: how sensors work. In: Wright EJ, Webb MC, Hightly H, editors, Proceedings of the Australian Postharvest Technical Conference Canberra 25-27, June 2003.

[56] Dirkson JA, Duval K, Ring TA. “NiO thin film formaldehyde gas sensor”, Sensor Actuator B: Chem, 80:106-115 (2001) and references therein.

[57] Mabrook M, Hawkins P. “Benzene sensing using thin films of titanium dioxide operating at room temperature”, Sensors, 2, 374-382 (2002).

[58] Gole JL, Prokes SM, Glembocki OJ, Yang R. “Unique properties of selectivity form ZrO_x nanostructures-light enhancement from a metal oxide”, Adv Mater,18, 664 (2006).

[59] Gole JL, Stout J, Burda C, Lou Y, Chen X. “Highly efficient formation of visible light tunable $TiO_{2-x}N_x$ photocatalyst and their transformation at the nanoscale”, J Phys Chem B,108,1230-1240 (2004).

[60a] Gole JL, Chen X, Lou Y, Samia ACS, Burda C. "Formation of oxynitride as the photocatalytic enhancing site nitrogen--doped titania nanocatalysts comparison to a commercial nanopowder", Adv Funct Mater, 15, 41-49 (2005).

[60b] Gole JL, Kumar S, Fedorov AG, "Photodegregation of ethylene using visible-light responsive surfaces prepared from titania nanoparticle slurries", J Appl Catalysis Envir, 57, 93 (2005).

[61] http://en.wikipedia.org/wiki/Air (Last Accesed on March 8th, 2011).

[62] G. Eranna, B. C. Joshi, D. P. Runthala, R. P. Gupta, Crit. Rev. Solid State Mater. Sci., 29, 111-188 (2004).

[63] E. Comini, Analytica Chimica Acta, 568, 28–40 (2006).

[64] http://www.transene.com/au.html (Last Accesed on March 8th, 2011).

[65] N. Barsan, M. Schweizer-Berberich and W. Gopel, Fundamental and practical aspects in the design of nanoscaled SnO2 gas sensors: a status report, Fresen. J. Anal. Chem. 365, 287–304 (1999).

[66] "Introduction to the Electroadsorptive Effect and its Applications", M. Bogner, T. Doll in "Advanced Gas Sensing: The Electroadsorptive Effect and Related Techniques", Ed: Theodor Doll, Kluwer Academic publishing, 2003, 1st Edition, USA.

[67] N. BMrsan, U. Weimar, J. Electroceram., 7, 143–167 (2001).

[68] Craig R. Barrett, Alan S. Tetelman, William D. Nix, "The principles of engineering materials", Prentice Hall, New Jersey, p. 428-429 (1973).

[69] M. J. Madou and S. R. Morrison, Chemical Sensing with Solid State Devices, Academic Press, San Diego, CA , p. 67-69 (1989).

[70] Kurt W. Kolasinski, Surface Science: Foundations of Catalysis and Nanoscience, 2nd Edition, Wiley, Great Britain, p.128 (2008).

[71] Chengxiang Wang, Longwei Yin, Luyuan Zhang, Dong Xiang and Rui Gao, "Metal Oxide Gas Sensors: Sensitivity and Influencing Factors", Sensors, 10, 2088-2106 (2010)

[72] A. Neubecker, T. Pompl, T. Doll, W. Hansch, and I. Eisele, Ozone-Enhanced Molecular Beam Deposition of Nickel Oxide (NiO) for Sensor Applications, *Thin Solid Films* 310, 19–23 (1997).

[73] T. Seiyama and S. Kagawa, "Study on a Detector for Gaseous Components using Semiconductive Thin Films", Analytical Chemistry 38, 1069–1073 (1966).

[74] M. Egashira, Y. Shimizu, and Y. Takao, “Trimethylamine Sensor based on Semiconductive Metal Oxides for Detection of Fish Freshness”, Sensors and Actuators B1, 108–112 (1990).

[75] C.G. Jernigan, G.A. Somorjai, Journal of Catalysis 147, 567-577 (1994)

[76] Arijit Chowdhuri , Vinay Gupta, K. Sreenivas, Rajeev Kumar and Subho Mozumdar , P. K. Patanjali “Response speed of SnO2-based H2S gas sensors with CuO nanoparticles” Appl. Phys. Lett., Vol. 84, No. 7 (2004).

[77] Y. Nakamura, H. Zhuang, A. Kishimoto, O. Okada, and H. Yanagida, “Enhanced CO and CO_2 Gas Sensitivity of the CuO/ZnO Heterocontact Made by Quenched CuO Ceramics”, J. Electrochem. Soc. 145, 632–638 (1998).

[78] E. Comini, G. Faglia, G. Sberveglieri, Zhengwei Pan and Zhong L. Wang , “Stable and highly sensitive gas sensors based on semiconducting oxide nanobelts” Appl. Phys. Lett., Vol. 81, No. 10 (2002).

[79] A. Kolmakov, Y. Zhang, G. Cheng, M. Moskovits, “Detection of CO and O_2 using Tin Oxide Nanowire Sensors”, Adv. Mater., 15, No. 12 (2003).

[80] C. Garzella, E. Comini, E. Tempesti, C. Frigeri, G. Sberveglieri, “TiO_2 thin films by a novel sol–gel processing for gas sensor applications”, Sensors and Actuators B 68, 189–196 (2000).

[81] Il-Doo Kim, Avner Rothschild, Byong Hong Lee,Dong Young Kim, Seong Mu Jo, Harry L. Tuller “Ultrasensitive Chemiresistors Based on Electrospun TiO_2 Nanofibers”, Nano Lett., Vol. 6, No. 9 (2006).

[82] M. Ferroni, V. Guidi, G. Martinelli, G. Faglia, P. Nelli, G. Sberveglieri ‘Characterization of a nanosized TiO_2 gas sensor’ Nanostructured Materials, Vol. 7, No 7, pp 709-718 (1996).

[83] C. N. Rusu and J. T. Yates, Jr., “Photochemistry of NO Chemisorbed on TiO_2 (110) and TiO_2 Powders” J. Phys. Chem. B, 104, 1729-1737 (2000).

[84] B. Karunagaran a, Periyayya Uthirakumar, S.J. Chung, S. Velumani, E.-K. Suh “TiO_2 thin film gas sensor for monitoring ammonia”, Materials Characterization 58 680–684, I-5, (2007).

[85] R. K. Nahar and V. K. Khanna, “A Study of Capacitance and Resistance Characteristics of an Al_2O_3 Humidity Sensor”, International Journal of Electronics 52, 557–567 (1982).

[86] T. Seiyama and S. Kagawa, "Study on a Detector for Gaseous, Components using Semiconductive Thin Films", Analytical Chemistry 38, 1069–1073 (1966).

[87] http://en.wikipedia.org/wiki/Oxygen_sensor (Last Accesed on March 8th, 2011).

[88] M. J. Madou and S. R. Morrison, "Chemical Sensing with Solid State Devices", Academic Press, San Diego, CA, p. 8-9 (1989).

[89] Yongtie Yan, Norio Miura, Noboru Yamazoe "Potentiometric sensor using stabilized zirconia for chlorine gas", Sensors and Actuators B, 24-25, 287-290 (1995).

[90] H. Steinebach, S. Kannan, L. Rieth, F. Solzbacher, "H_2 gas sensor performance of NiO at high temperatures in gas mixtures", Sensors and Actuators B, 151, 162–168 (2010).

[91] D. F. Remar, A. M. Turiev, N. I. Tsidaeva, and T. T. Magkoev "Adsorption of Nitrogen Oxide Molecules to the Surface of Nanosized Nickel Clusters Formed on the (111) Surface of a Magnesium Oxide"Russian Physics Journal, Vol. 53, No. 5 (2010).

[92] M. A. Martin, J. P. Santos, H. Vásquez, and J. A. Agapito, "Study of the Interference of NO_2 and CO in Solid State Commercial Sensors", Sensors and Actuators B58, 469–473 (1999).

[93] C. D. Natale, F. Davide, G. Faglia, and P. Nelli, "Study of the Effect of the Sensor Operating Temperature on SnO_2-Based Sensor-Array Performance", Sensors and Actuators B23, 187–191 (1995).

[94] F. Berger, M. Fromm, A. Chambaudet, and R. Planade, "Tin Dioxide-based Gas Sensors for SO_2 Detection:A Chemical Interpretation of the Increase in Sensitivity Obtained after a Primary Detection", Sensors and Actuators B45, 175–181 (1997).

[95] I. Sayago, J. Gutierrez, L. Ares, J. I. Robla, M. C. Horrillo, J. Getino, J. Rino, and J. A. Agapito, "The Effect of Additives in Tin Oxide on the Sensitivity and Selectivity to NO_x and CO", Sensors and Actuators B, 26-27, 19–23 (1995).

[96] A. D. Brailsford, M.Yussouff, and E. M. Logothetis, "Steady State Model of Electrochemical Gas Sensors with Multiple Reactions", Sensors and Actuators B, 35-36, 392–397 (1996).

[97] T. Usui, A. Asada, M. Nakazawa, H. Osanai, "Gas Polarographic Hydrogen Sensor Using a Zirconia Electrolyte" Japanese Journal of Applied Physics, Vol 28, No 9, pp L 1654-L 1656 (1989).

[98] Shigeaki Suganuma, Misa Watanabe, Tuyoshi Kobayashi, Shin-ichi Wakabayashi "SO gas sensor utilizing stabilized zirconia and sulfate salts with a new working mechanism" Solid State Ionics 126, 175–179 (1999).

[99] N. Taguchi, US Patent 3695848, 1972.

[100] Figaro TG-2442 CO Gas Sensor, Figaro Inc. http://www.figarosensor.com/products/2442pdf.pdf (Last Accesed on March 8th, 2011).

[101] Gas Handbook, Honeywell Analytics. http://www.honeywellanalytics.com/Technical%20Library/EMEAI/1%20Types%20of%20Documents/Gas%20Book/Gas%20Book%20English.pdf (Last Accesed on March 8th, 2011).

CHAPTER 2

POROUS SILICON FORMATION & SENSOR FABRICATION

2.1 Silicon

Silicon (Si) is the second most abundant element (after oxygen) by mass on earth and usually found as various forms of silicon dioxides and silicates. It is the principal substrate of most of the semiconductor devices such as integrated circuits (ICs), photovoltaics and microelectromechanical (MEMs) devices. Si is a group IV element with four valence electrons. It forms a diamond like crystal structure where each Si atom forms a covalent bond with four nearest neighbor Si atoms. At room temperature and atmospheric pressure, high purity silicon has an indirect band gap of 1.12 eV and its bandgap decreases as a function of increasing temperature. Intrinsic Si has an electrical conductivity a few orders of magnitude lower than metals at room temperature. The ability to grow good quality SiO_2 as a dielectric layer by simple means (eg. thermal oxidation in furnace systems under O_2 or in contact with water vapor at higher temperatures (~ 1000 ^{0}C)) is one of the main advantages allowing the wide use of silicon in electronic devices. Its mechanical stability enables the integration of mechanical and electronic parts on the same substrate. It is a feasible substrate choice for integrating sensing and signal processing electronics on the same chip. Smart sensor systems have sensing parts, analog to digital converters, and electrical communication channels all on the same silicon substrate. Its extreme flatness makes the silicon surface excellent for thin film depositions. A great deal of thin film equipment is built to accommodate silicon and there are well-established coating processes for a wide variety of thin films. Its ease of metallization is another advantage for electronic applications. It is manufactured in 3 crystal forms; single crystal, polycrystal and amorphous. Most electronic applications are based on single crystal silicon substrates. Silicon monocrystals are grown via the

Czochralski (CZ) process. After the Si ingot is grown, it is cut into individual wafers, as the surface of the wafers is aligned in one of several relative directions known as crystal orientations. The most common crystal orientations are (100), (111) and (110). (100) single crystal silicon wafers have been used almost exclusively in all PS experiments. However, pores can be created in all these crystal orientations. Silicon wafers have distinctive primary and secondary flats which indicate the type and orientation of the crystal. The primary flat which has a specific crystal orientation with respect to the wafer surface is the flat of longest length, located in on circumference of the wafer. The location of the secondary flat varies with respect to the crystal orientation and doping of the wafer. The primary and secondary flats of silicon (100) are shown in Figure 2.1. Cleavage is done using a scriber which has a synthetic diamond on its tip. When the surface plane crystal orientation of the Si is (100), the cleaved pieces form rectangles (at 90 degrees angles). Since the gas sensors are fabricated in rectangular shapes, it is possible to dice the wafer simply with a scriber with a very high yield. This also enables easy final packaging of the sensors. One popular method to dice wafers of closely packed devices is to use automated dicing tools (eg. The dicing Saw from Dicing Technologies at the MiRC Cleanroom of Gatech.). It is possible to purchase wafers with different sizes. The standard wafer sizes are 2, 4, 6, 8, 12 inches. Processing larger wafers is cost effective and in the semiconductor industry, the current state of the art fabs use 300 mm (12 inch) wafers. It is easier to control the pore characteristics when a small area is etched. In all the experiments presented in this thesis, 2" wafers are employed.

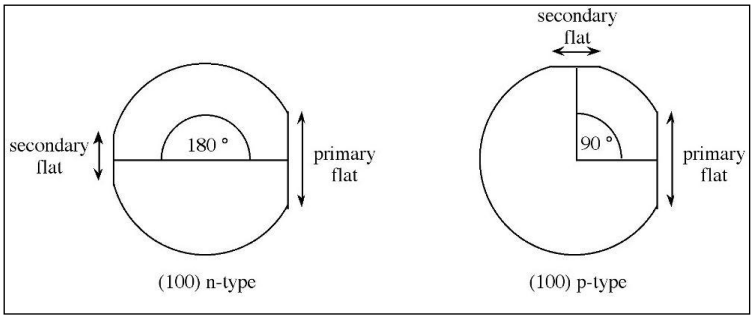

Figure 2.1. Primary and secondary flats of silicon (100).

One may adjust the doping level of Si by adding phosphorus or boron to the silicon melt during the crystallization process of CZ growth. In n type silicon, a phosphorus atom which has five valence electrons replaces a silicon atom and donates the extra electron to the conduction band of the lattice. On the other hand, a boron atom with three valence electrons is used to substitute a silicon atom for p type doping. The extra positively charged hole is donated to the valence band. I have used a variety of doping levels in anodization experiments. Two major manufacturers (Wafer World Inc. and Siltronix) have been contacted to purchase the silicon substrates. The resistivity range of the wafers in a batch as specified by the manufacturer is shown in Table 2.1.

Table 2.1. Resistivity range of the wafers purchased for PS anodization experiments.

	p +	**p**	**n**	**n+**
Resistivity (Ωcm)	0.005-0.02	7-13	1-20	0.001-0.005

Resistivity is a key etch parameter in the electrochemical etch process. Resistivities of the wafers are measured via a four point probe technique [1]. The 4- point probe technique can be applied to measure the resistivity of any type of semiconductor or thin film. A typical 4-point probe station is shown in Figure 2. The four point probe contains four thin parallel tungsten wire probes which are made to contact the wafer for testing as in Figure 2.2. The outer probes (1 and 4 in Figure 2.2) are used to flow the desired amount of current and the inner probes (1 and 2 in Figure 2.2) are used the measure a voltage difference.

The resistivity of a material is given by Equation 2.1.

$$R = \rho \frac{L}{Wt} \qquad \text{(Equation 2.1)}$$

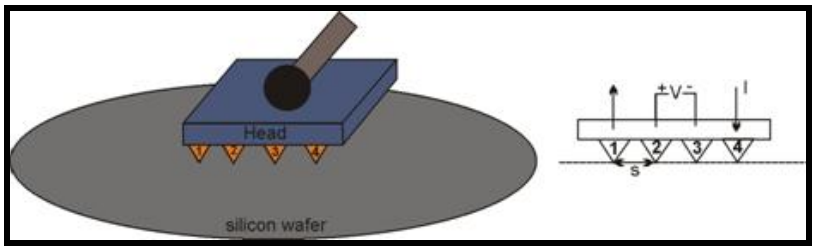

Figure 2.2. A four point probe station is depicted (not to scale). The head holds 4 probes. The voltage difference between interior probes is measured while a current is applied through the exterior probes. The separation (s) of the probes is ~ 1 mm with s>>t (wafer thickness).

In Equation 2.1, ρ is the material resistivity, L is the length of the resistor, W is the resistor width and t is the thickness of the layer. The unit for resistivity is Ohms-cm which refers to the bulk or volume resistivity of the test material. This factor is independent of the shape or size of the material. The resistivity of the silicon wafer is controlled by the amount of dopants added to the ingot during the CZ growth. However, the thickness of the wafer (250-300 μm) is determined during the slicing step of the bulk Si crystal after the CZ growth. Using these two controlled parameters which are constant for each wafer, one can define sheet resistance ρ_s. The unit of sheet resistance is Ohms, the same as the bulk resistance because the bulk resistance is multiplied by a dimensionless quantity to get sheet resistance. As an alternative, "Ohms per square" is used as a common unit for sheet resistance so that it won't be misinterpreted as bulk resistance. Its meaning is that a layer which has a 1 Ω/sq. sheet resistance will have a 1 Ohms resistance regardless of the size of the square area. The sheet resistance (Equation 2.2) is dependent on the thickness of the material.

$$\rho_s = \rho / t \qquad \text{(Equation 2.2)}$$

The 4-point probe approach to measuring resistivity states that if the sample is of semi-infinite volume and if the interprobe spacings are s, the resistivity of the semi-infinite volume can be found as:

$$\rho_o = \frac{2\pi s V}{I} \qquad \text{(Equation 2.3)}$$

Real samples have finite size and a thickness correction factor is needed [2].

$$\rho = 4.53\frac{2\pi s V}{I} \qquad \text{(Equation 2.4)}$$

The resistivity measurements and their variations in a batch are shown in Figure 2.3. Batch 1 was purchased from Siltronix (France). The batch consists of 25 p-type Boron doped 2" wafers with resistivities ranging from 7-13 Ωcm. The wafers were prepared by CZ process, single side polished, test grade and their orientation is (100) ± 0.5^0. The thickness of the wafers ranges from 250 μm to 300 μm. In most of the gas sensor experiments, wafers with these characteristics are utilized. Batch 2 was purchased from Wafer World Inc. The batch consists of 25 p-type Boron doped 2" wafers with resistivities ranging from 1-20 Ωcm. These wafers are also prepared by CZ growth, single side polished, test grade, have an orientation is (100) ± 0.5^0. The thickness of each wafer ranges from 250 to 300 μm. Batch 2 was utilized in a number of etching experiments. The resistivities of these two batches were measured using a Signatone Four-point Probe. The resistivities measured are shown in Table 2.2. The measurements are done at the center of the wafers. The average resistivity for batch 1 is 10.8 Ωcm. The standard deviation shows the amount of variation from the mean. The standard deviation for this Batch 1 is 1.3 Ωcm which is a third of the standard deviation of the Batch 2.

Table 2.2. The resistivity of a wafer is an important parameter for the porous silicon etch mechanism. The resistivity measurements for two batches of 25 wafers from two different vendors with different specifications show the indicated variations for wafers from the same batch.

	Batch 1	**Batch 2**
MEAN	10.7 Ωcm	6.5 Ωcm
STDEV	0.9 Ωcm	4.5 Ωcm

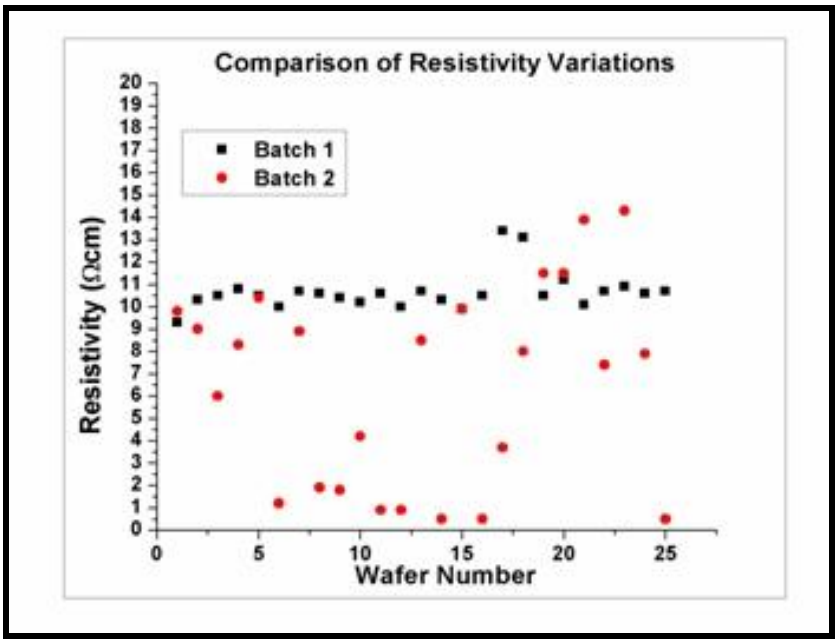

Figure 2.3. Fluctuations of the base resisitivity of two batches of wafers measured by a four point probe technique.

Chemical (wet) etching is used for wafer cleaning, polishing and patterning structural features. Chemical etching usually has a better selectivity than dry etching techniques. However, it has some disadvantages such as a lack of anisotropy, poor process control and particle contamination. The important parameters in chemical etching are etch rate, anisotropy and selectivity. The wet etching rate is usually higher than that for dry etching; from a few microns per minute to tens of microns for isotropic wet etchants and ~ 1 micron/minute for anisotropic etches compared to ~0.1 micron/min for dry etching [3]. In a typical chemical etching, there are three major process steps; transport of the reactants to the surface, surface reaction, transport of the reaction products away from the surface. Each one of these steps can be rate limiting. In the chemical etching of silicon, it is usually the surface reaction step that determines the etch rate and this step depends on the substrate surface, etching solution, temperature, and agitation.

2.1.1 Wafer Cleaning

Wafer cleaning is the first step before any thin film deposition. The goal of this step is to clean the oxide and remove any kind of impurities and contamination on the wafer surface and create a perfect silicon surface. When a silicon wafer is exposed to air under ambient conditions, the surface forms a native oxide and collects carbon. The native oxide thickness is about 10 Å.

One of the most popular wet etch cleaning processes for silicon is the RCA clean [4]. The RCA clean is used to remove organic contaminants, the oxide layer, and metallic contaminants and it consists of three steps:

1- The silicon wafer is soaked in $NH_4OH : H_2O_2 : H_2O$ (1:1:5) @ 75 ^{0}C for 10 min. to remove organic contaminants (photoresist, oil etc) and then cleaned with DI water.

2- The wafer is put into dilute HF (HF: DI H_2O; 1:20) @ 25 ^{0}C for 10 sec. to remove the oxide layer created by the strong oxidant H_2O_2 in the previous step and then a DI water rinse is performed.

3- The wafer is then soaked in HCl: H_2O2: H_2O (1:1:6) @ 75 ^{0}C for 10 min to remove alkali ion and heavy metal contaminants and cleaned with DI water.

After the RCA clean, the wafer is dried thoroughly with N_2 gas. This process leaves a thin oxide layer on silicon, free of any type of contaminants. Before doing any epitaxial growth on silicon, it is a common practice to remove the oxide layer by repeating step 2. Another common application of chemical etching is that after a lithography step for fast removal of photoresist. The wafer is soaked in acetone (10 min), methanol (5 min), and isopropanol (5 min) and rinsed with DI water. In some cases, an ultrasonic acetone bath might be employed for sticky resist formations after a hard bake step. More resistant organic contaminants are stripped in piranha clean which consists of a mixture of 98% H_2SO_4 and 30% H_2O_2 in volume ratios of 4:1 at 100 ^{0}C [5].

2.2 Porous Silicon Formation

Porous silicon (PS) formation was first reported by Uhlir in 1956 [6]. It has been studied extensively since the 1990s after the discovery of photoluminescence from a porous silicon surface in the visible range under ultra violet (UV) illumination. The main research interest was initially for optoelectronics applications using the photoluminescence and electroluminescence of a PS surface [7]. The main PS research areas have involved sensors [8-10], photocatalytic reactors [11,12], drug delivery, filters, nanostructured templates [13], microcavities, and batteries [14] in the Gole research group.

We classify pore dimensions before discussing the details of pore formation and various pore morphologies. There are three characteristic pore dimensions that are used to distinguish PS surfaces: (average) pore diameter, (average) pore spacing and (average) pore depth. These dimensions are also used to describe the *porosity* of a PS surface. Some literature follows the IUPAC standard and divides the average PS pore diameter and spacing into 3 categories: Micropores ($d < 10nm$), mesopores ($10nm < d < 50$ nm) and macropores ($d > 50$ nm) [15]. Although micro-, meso- and macro- prefixes are regularly used to describe PS, the distinction between the corresponding length scales is not precise and this nomenclature is used loosely. *Nanopores* ($d < 100$ nm) and *micropores* ($d > 0.5$ μm) have been used to distinguish two main characteristic length scales in this thesis. Pore dimensions from a few nm to 100 μm have been observed with various electrochemical etch solutions throughout this research. It is also possible to achieve multiple pore dimensions on the same surface with a single etch. A *hybrid* pore structure, which is the primary PS structure used in the Gole group for gas sensing, corresponds to a nanopore covered microporous surface with an amplified surface area.

The pore creation in silicon can be divided into two categories: Electroless etching and electrochemical etching. Electroless etching does not require external charges in the chemical dissolution process as opposed to electrochemical etching. The widely

accepted basic principle for both methods is first the creation of SiO_2 by oxidizing the silicon surface at random surface sites and then the removal of SiO_2 molecules by hydrofluoric acid (HF), creating a porous network. The distribution of the oxidation sites is important in the sense that a uniformly oxidized surface is *electropolished* after the removal of the oxidized layer, leaving behind a perfectly flat and shiny surface instead of a porous structure. The morphology and etch direction of the pores strongly depend on the etch solution and wafer characteristics and will be discussed later in this chapter.

2.2.1 Electroless Etching:

Electroless etching methods have the advantage of simplicity over electrochemical etching. There are two popular methods for the electroless etching of silicon: A stain etching and metal assisted etching. Stain etching solution is usually an aqueous mixture of acidic fluoride (HF) and an oxidant (e.g nitric acid) (See Equation 2.5). The Turner Mechanism which describes the stain etching process states that nitric acid injects holes into the valence band and aids surface oxidation (SiO_2 formation) in an aqueous solution. SiO_2 molecules are removed by an HF attack through the formation of H_2SiF_6 [16]. Stain etching is usually very suitable for producing thin layers of porous films.

$$Si + HNO_3 + 6HF \rightarrow H_2SiF_6 + HNO_2 + H_2 + H_2O_2 \qquad \text{(Equation 2.5)}$$

Metal Assisted Etching

In metal assisted etching, metal nanoparticles (usually Au or Ag) are deposited onto the Si surface. These particles are believed to catalyze SiO_2 formation in their vicinity. The SiO_2 is then etched by HF, resulting in continuous etching of the Si region around the nanoparticles. Silicon nanowires (SiNW) may form as the samples are kept in the etching solution. The diameter of the porous structures created, as a result, is around the physical size of the nanoparticles (or clusters) deposited [17].

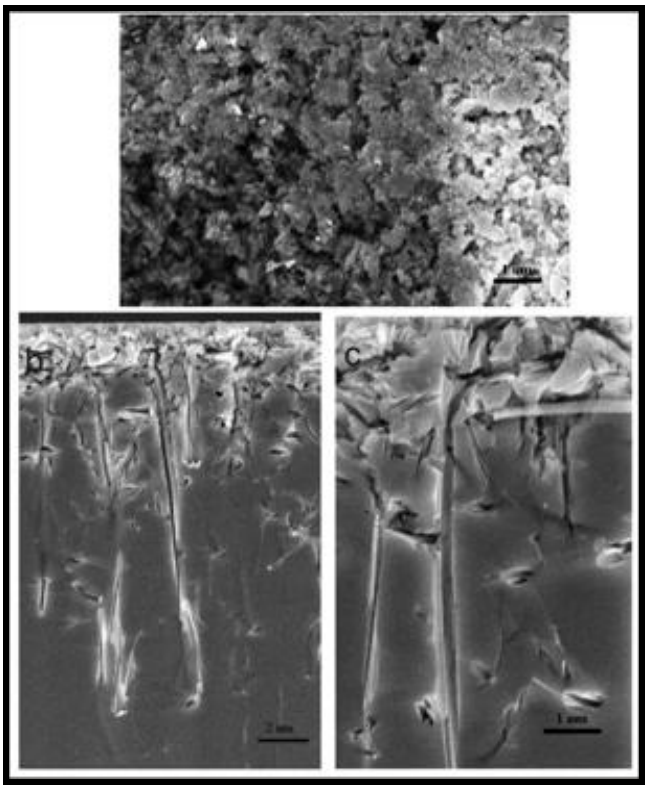

Figure 2.4 a) The top surface has small pores which are randomly distributed and not clearly defined. b) Helical pores where gold nanoparticles are at the bottom and catalyze pore growth c) Pore diameters vary due to the nonuniformity of the size of the gold particles. The pore diameter varies from 10's of nm to few 100 nm.

Scanning electron microscope (SEM) images of the pores formed via metal assisted etching are shown in Figure 2.4. A quarter of a 4" p type wafer is immersed in a dilute HF solution for a few minutes to roughen the surface and rid it of native oxide. A gold layer of thickness 50 Å is deposited onto the rough surface via the e-beam deposition method. The wafer is then etched in a mixture of 20 ml HF (49 %) and 15 ml H_2O_2 (30 %) for 5 minutes by following a similar recipe as described in Ref [18]. The Levy-Clement group claims that a Au nanoparticle etch rate is about 10 times higher than that for a thin Au film etch rate and that Ag particles have a better catalytic activity and faster etch rate than Au particles [18]. The top surface of the porous structure (Fig. 2.4 (a)) has a brownish color with pore diameters much smaller than 1 μm. The pores are randomly distributed in the first 1 μm depth of the surface and not clearly defined. An

application area for similar non-regular porous surfaces is found in antireflection coatings for solar cells. In Figure 2.4 (b), an SEM side view of a deeper ~10 μm pore is shown. The gold clusters at the bottom of the pores are distinguished clearly. The pores have a cone shape with an average pore diameter of a few 100 nm (Figure 2.4 (c)).

2.2.2 Electrochemical Etching:

The electrochemical etching method is by far the most studied method of PS creation because it can lead to various pore morphologies under controlled anodization conditions. When the wafer is bought from the manufacturer, one side of the wafer is polished by chemical mechanical planarization (CMP) which utilizes both chemical and mechanical means to smooth the surface. CMP is a global planarization method [19]. Figure 2.5 shows the basic steps of the electrochemical etch process. The top surface of the wafer is already polished at the beginning of the process, as shown in Figure 2.5 (a). In a fluoride containing acid electrochemical etch solution, the already polished surface become roughened, as shown in Figure 2.5 (b). At this stage, we can define two etch rates, a horizontal etch rate (R_h) and a vertical etch rate (R_v), that compete with each other (a similar definition is given in Ref-16). At the roughening stage (Figure 2.5 (b)), R_h is on the order of R_v. Pore nucleation at random surface sites starts just after surface roughening. One method of generating exact pore initiation sites is creating etch pits via nanoindentation or e-beam lithography methods. Although it is not possible to control the exact pore nucleation sites on the wafer during an electrochemical etch, it is much simpler and cost effective to control porosity and pore morphology compared to top-down approaches. Figure 2.5 (c) shows the pore propagation stage. At this stage, there is a constant current or voltage applied between the wafer (anode) and a counter electrode (usually a Pt cathode). The resultant electric field forces holes in the wafer to move to the silicon/electrolyte interface. R_v is significantly larger than R_h due to hole injection at the tip of the pores during the pore propagation phase.

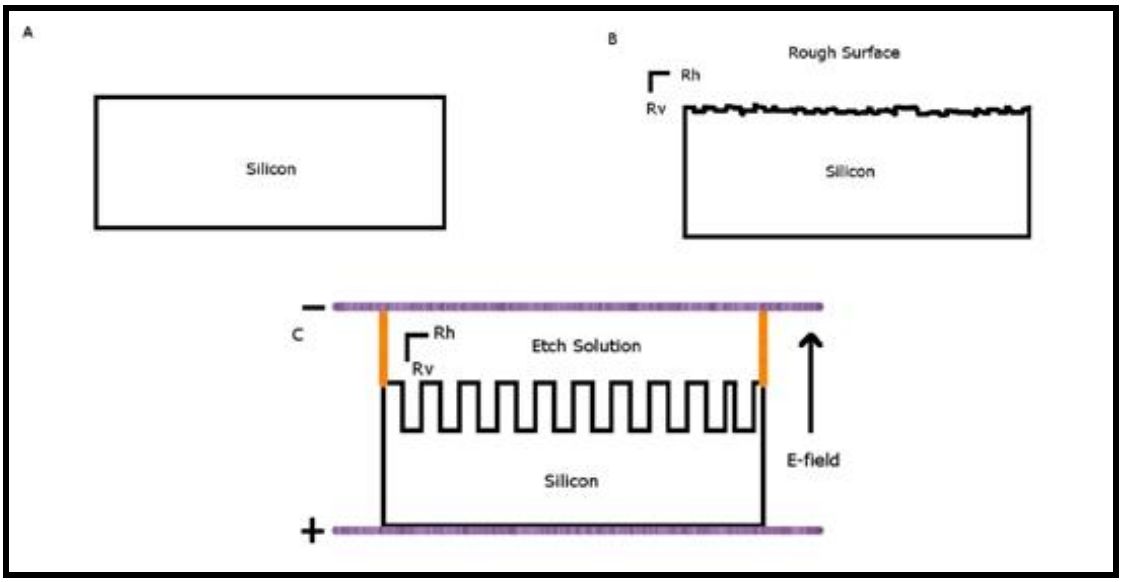

Figure 2.5 a) A top side polished Si surface. b) At the first phase of the electrochemical etching, the surface roughens and pore nucleation centers start to appear. At this stage, R_v (vertical etch rate in the electrochemical solution) is on the order of R_h (horizontal etch rate). c) During the pore propagation phase, R_v is significantly larger than R_h, due to hole injection at the tip of the pores. The thickness of the wafer and the porous film is not scaled in the diagram.

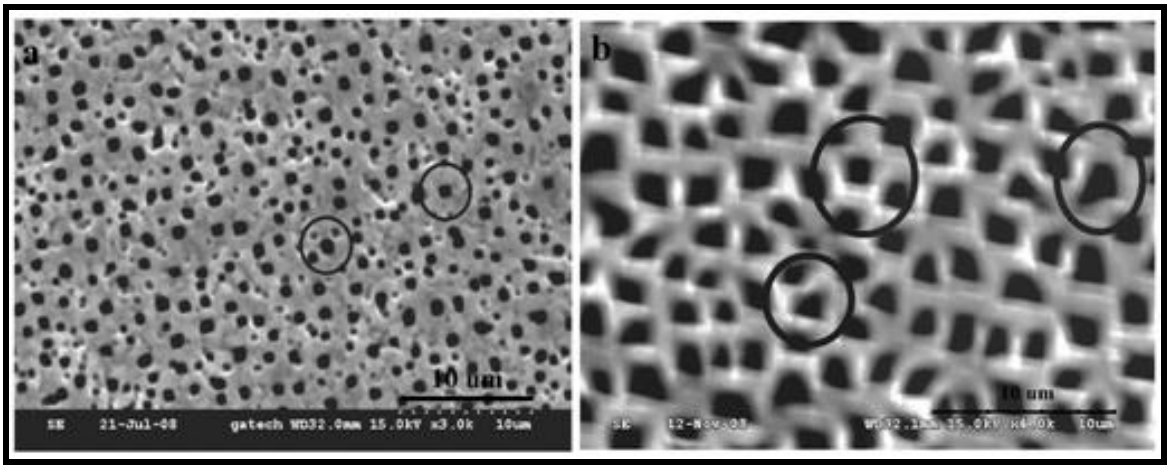

Figure 2.6. Different pore nucleation profiles may be seen on the same surface. (a) SEM image - top view of a p-type wafer anodized in HF-MeCN electrolyte. Circular and square openings are shown. (b) Triangular and square openings seen on another sample anodized under similar conditions.

When Si is left in HF for an extended period of times, its surface is roughened. Surface defects are excellent pore initiation sites. At the first stage, the pore initiation sites that are closer to each other might join to form pores of larger diameters. Pore diameters as large as a few μm have been observed. SEM images of different pore nucleation profiles of anodized p-type wafers are shown in Figure 2.6. In Figure 2.6 (a), circular and square pores are marked on the image and in Figure 2.6 (b) triangular and square openings are depicted. This kind of pore nucleation strongly depends on the etch parameters which will be discussed later in this chapter.

Because of the different pore morphologies observed in various types of silicon wafers, there have been many models proposed to describe pore formation in each case. By far the most popular model in the PS community is the quantum model proposed by Lehmann and Gosele to describe pore formation during the electrochemical process [20]. According to this model, pore walls are passivated due to the depletion of charges on the walls and pore propagation continues at the pore tips where the space charge region is thinner. When silicon is put in an aqueous HF solution, the surface becomes hydrogen terminated instead of fluorine terminated. Although the Si-F bond is stronger then the Si-H bond, the fluoride terminated surface polarizes the back Si-Si bonds and the Si surface becomes kinetically unstable. Since the electronegativity of hydrogen and silicon are about the same, the Si surface becomes nonpolar and immune to chemical attacks. All pore formation models suggest that the dissolution mechanism at the silicon electrode is reaction rate limited by the hole supply [21]. When holes reach the surface due to the external electric field, they weaken Si-H bonds and make them susceptible to F^- attack in order to form an Si-F bond. The already formed Si-F bond further polarizes and weakens the back Si-Si bonds and helps another F^- attack to form H_2 as a byproduct. This helps further F^- attacks forming $SiHF_3$ or SiF_4 and, finally, resulting in removal of the silicon atom from the surface. After a Si atom is removed from the surface, creating a dip on the initially flat surface, the transformation of surface morphology gives rise to a preferential

hole transfer from the bulk to this location due to the electric field. This process is depicted in Figure 2.7 (a). Porous silicon formation is initiated by the formation holes in the valence band [22]. Holes move to the surface during an electrochemical etch process. The bottom of the pore has a conical U-shape where hole injection is a maximum at the tip. Figure 2.7 (b) shows an SEM image of a pore tip in a p-type Si wafer. The tip radius is ~ 600 nm for this pore.

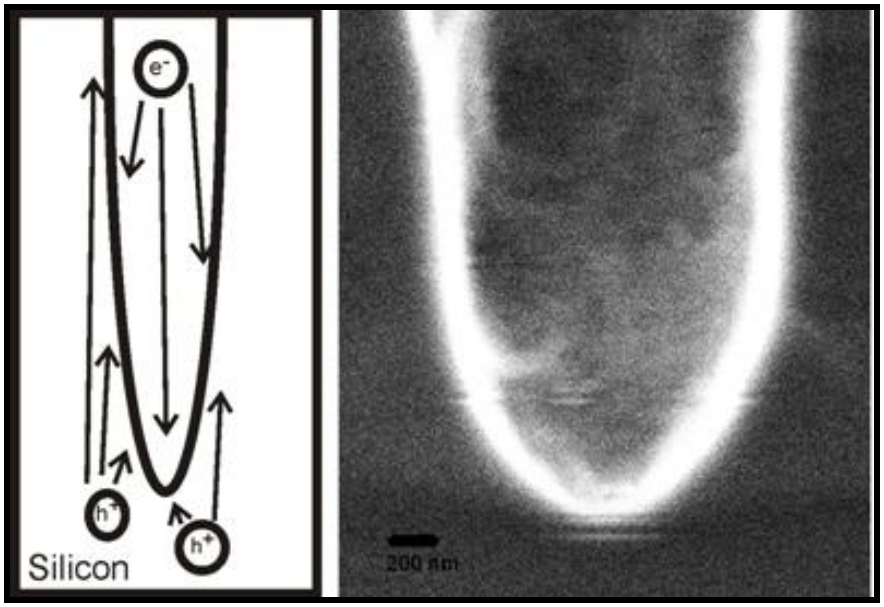

Figure 2.7 (a) Holes move to the tip of a pore due to the external electric field and pore propagation continues mostly on pore tips instead of on the depleted walls. (b) SEM image of a pore tip in p-type Si. The tip radius is ~ 600 nm for this pore.

Although the pore walls are depleted according to the Gosele model and an electrochemical etch results in very high aspect ratio pore by pore propagation at the pore tips, a very long etch duration may cause thinning in the pore wall thickness, decrease pore spacing and increase pore diameters. An example is shown in Figure 2.8. After one hour anodization of a p-type wafer in a hybrid etch solution at 3 mA/cm^2, the pore walls start to collapse (Figure 2.8 (b)). Even though R_h is much smaller then R_v, pore diameter expansion and pore wall weakening is observed for long anodization durations. If the

electrochemical etch continues after this point, the whole surface becomes electropolished, leaving behind a flat Si surface.

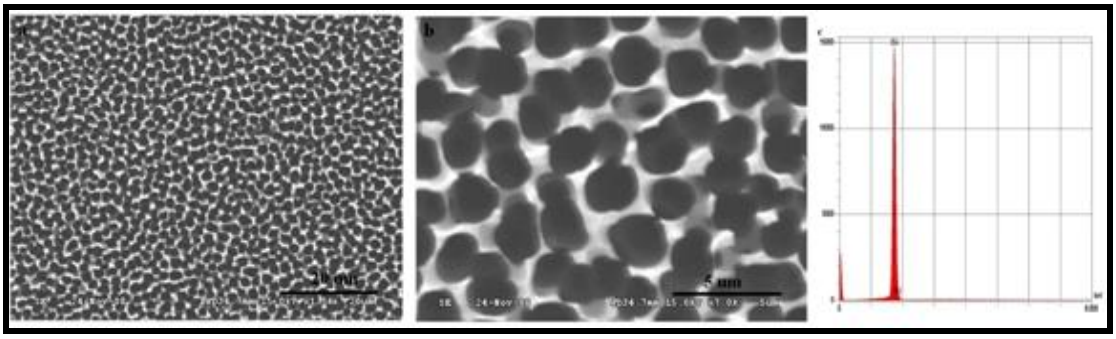

Figure 2.8. (a) Top view SEM image of a p type wafer etched in a hybrid etch solution for 3600 s. (b) Closeup SEM image of the pore walls which have already started to collapse is shown. Although R_h is much smaller then R_v, pore diameter expansion is observed for long anodization durations. (c) An energy-dispersive x-ray spectroscopy (EDS) spectrum of the same surface is shown.

Etch Conditions

HF-H_2O systems are generally classified as aqueous etch solutions used in the electrochemical anodization of Si [15]. HF which has been utilized in all experiments is 48-51% (in water) (Alfa Aesar). The clean Si surface is hydrophobic. Ethanol (C_2H_5OH) is usually added to the aqueous solutions to increase the wettability of the Si surface and enhance HF interaction. During the electrochemical etch process, H_2 bubbles form and cover the Si surface. Aqueous solutions produce more H_2 compared to non-aqueous etch solutions. Further attack by fluoride ions at the surface is prevented due to this bubble formation. The other advantage of using surfactants (e.g. ethanol) is to remove bubbles from the surface. All n-type wafer anodization experiments are done in HF-Ethanol solutions of various ratios.

NH_4F is usually used as a buffering agent with HF for SiO_2 dissolution by the reaction path, as indicated in Equation 2.6. Because the reaction slows down with time due to HF consumption, NH_4F is added to the solution to maintain a constant concentration of HF and solution pH to keep the reaction rate constant (Equation 2.7). In

an electrochemical etch solution, NH_4F can be used to substitute HF as the fluoride source.

$$SiO_2 + 6\,HF \rightarrow H_2 + SiF_6 + 2H_2O \qquad \text{(Equation 2.6)}$$

$$NH_4F \rightarrow NH_3 + HF \qquad \text{(Equation 2-7)}$$

No oxidant (e.g. HNO_3 or H_2O_2) is necessary for an electrochemical etch as opposed to electroless etching techniques. The holes required in the dissolution process are supplied by excess electron-hole (e-h) pairs created by the electric field or optical excitation. The resistivity of an aqueous solution decreases with increasing water concentration [23]. However, additional oxidizing agents may be used to increase the etch rate and control the surface morphology. The HF concentration in aqueous solutions is usually high (HF:Ethanol ratios ranges from 1:5 to 1:1). Addition of H_2O_2 (1ml) to an HF-Ethanol (10 ml:10 ml) solution give rise to microporous structures instead of nanopores for anodized n-type wafers (1-20 Ω cm). Aqueous electrolytes have always been the chosen anodizing solution for n-type wafers throughout the research discussed in this thesis.

Another category of electrochemical etch solution is a non-aqueous solution where HF (49 % in H_2O) is mixed with organic electrolytes such as acetonitrile (MeCN) or dimethylformamide (DMF) [15,24]. P-type wafer anodization experiments discussed in this thesis have always been performed in organic electrolytes. Organic electrolytes usually have a high resistivity. In acetonitrile based solutions, an oxidizing agent, tetra-n-butylammonium perchlorate (TBAP) is used to increase etch rate and decrease electrolyte resistivity. The HF concentration in organic electrolytes is much lower compared aqueous electrolytes and the HF:Org. electrolyte ratio varies from 1:10 to 1:25. However, their etch rate is fast and usually give rise to microporous morphologies. DMF electrolyte has a higher oxidizing power than MeCN and doesn't need an extra oxidant. A MeCN

solution gives rise to a nanopore covered microporous surface under appropriate etching conditions. On the other hand, a DMF solution gives rise to smooth and deep microporous surfaces which are more suitable for filtering applications. Most of the p-type wafers anodized in DMF/HF electrolyte show a pale, smooth PS top surface. However, p-type wafers anodized in MeCN:HF electrolyte often result in surface textures of concentric rings which are visible by naked eye. Similar surface textures have never been reported in the literature and their photos are depicted in Appendix II.

It is possible to work in either constant current or constant voltage regimes during Si dissolution. It is widely accepted that constant current gives better control of pore morphology, porosity, and the reproducibility of the PS layer. The current applied to the electrolyte/Si interface is another important parameter. In general; if the hole supply to the electrolyte/Si surface is low (due to low doping in p-type wafers or low UV illumination intensity and/or high doping in n-type wafers), the HF concentration should be increased and the applied current should be decreased to get porous silicon. By contrast, if the hole supply is sufficient, the HF concentration should be decreased and the applied current should be increased to get porous silicon. It is usually recommended that one obtain a current-voltage (IV) curve of an electrochemical etch to decide on the current that should be applied in the constant current mode. A schematic of the IV relationship of an electrochemical anodization of n type silicon under UV illumination or p-type silicon without illumination is depicted in Figure 2.9 (Adapted from Ref-25). The schematic shows that there is no cathodic dissolution of silicon and there are two key current levels, namely I_{PS} (PS formation limiting current) and I_{Ox} (oxidation current) that determine the behavior of the process. Under cathodic potentials, water is reduced on the Si/HF interface forming H_2. Pore formation occurs in the initial rising part of the IV curve. I_{PS} is the maximum current that can be applied to get pore formation. After this current limit, electropolishing occurs. The I_{PS} peak depends on the solution composition and wafer resistivity. I_{Ox} represents the anodic oxidation peak. After this limit, the surface

is still electropolished and the IV curve shows linear oscillations (not shown in the schematic).

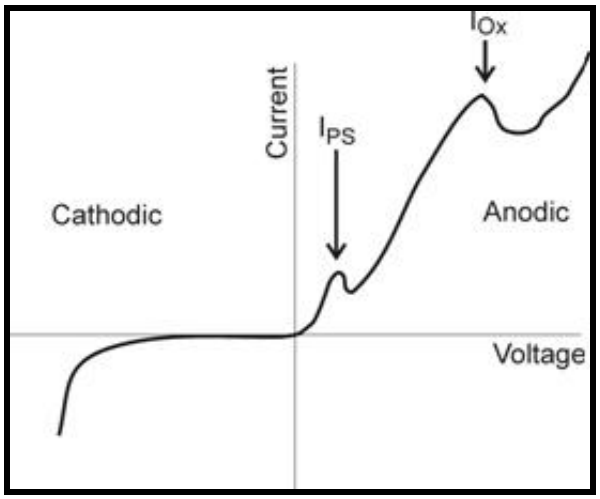

Figure 2.9. A schematic of the IV curve of electrochemical anodization of n type silicon under illumination and p type silicon in the dark (Adapted from Ref-25). The scale is arbitrary and the position of the electropolishing and oxidation peaks depends on the experimental conditions and wafer properties.

An IV relationship of a p-type wafer (1-20 Ω cm) anodized in HF:MeCN (1:20) solution is shown in Figure 2.10. In this experiment, the voltage is increased from 0 to 30 V with 0.25 V increments every 0.5 s. and the corresponding current passing through the electrolyte is measured. The initial rising part of the curve is where pore formation occurs and the constant current that needs to be applied for pore formation should be chosen from this part of the IV curve. At a current around 50 mA, we can see the start of the transition region where the electropolishing and pore formation rates start to compete with each other. After 75 mA, the electropolishing regime dominates the process. This IV curve shows us that 40 mA would be a good constant current for anodizing this wafer. The anodization area for this sample is about 4 cm^2, so the upper limit of the necessary current for pore formation corresponds to 10 mA/cm^2. In some cases, the I_{PS} peak is not seen and only the pore formation region appears in 0-30 V range. Any current in the rising part of the curve should result in pore formation for these wafers. As the water

content in the solution decreases, the electropolishing current peak starts to disappear [24].

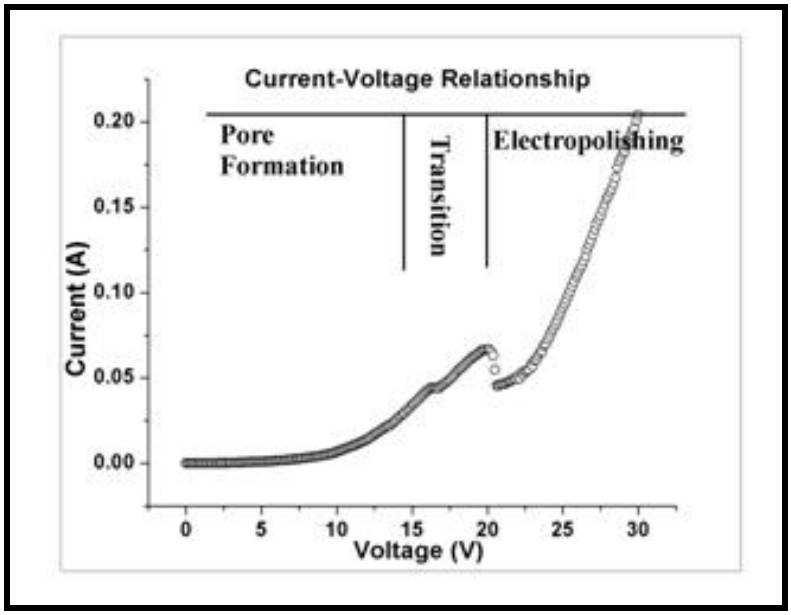

Fig 2.10 A typical IV curve for an electrochemical etch in organic electrolytes is shown. The voltage is increased from 0 to 30 V with 0.25 V increments (frequency 2 Hz) and the resulting current passing through the electrolyte is shown on the y-axis. Pore formation occurs with applied currents up to 75 mA.

A nanoporous PS surface is photoluminescent in the visible range of the electromagnetic (EM) spectrum under UV illumination. This property has been one of the most investigated properties of nanoporous surfaces due to the possibility of various applications in optoelectronics. The intensity of photoluminescence is proportional to the porosity of the surface. There have been two widely accepted theories to describe the photoluminescence of PS. The first one, quantum confinement, states that charge confinement within the nanoporous surfaces (wires) increases the band gap of Si and the probability of a direct band gap recombination [25]. In this theory, as the pore size decreases, the quantum confinement increases and shifts the photoluminescence toward blue range of the spectrum. The second widely accepted approach to explain photoluminescence is surface chemistry. There are silicon oxyhydride fluorophors bound to the porous silicon surface. When the silicon oxyhydride-based surface functional

groups are illuminated with UV light, these surface fluorophors become electronically excited [26] and they emit light in the visible range when they decay to the ground state from these excited states. The decay time and luminescence intensity are both affected by the oxidation level of the surface.

Parameter Space

As described in the PS etch mechanism above, the parameters that may affect the pore morphology and porosity are diverse and small modifications in each parameter might have significant consequences. Wafer characteristics, crystallographic orientation, doping type and level, are, by far, the most important parameters. In all experiments, Si wafers with (100) orientation are used exclusively. {111} planes have the highest packing density in Si and it is much easier to create pores and control the morphologies in {100} planes in an electrochemical etch. The hole transfer rate is determined by the electronic properties of the Si electrode. Anodizing p-type wafers has the benefit of using a simpler etch cell with no need of external illumination. However, n-type wafers are usually the doping type of choice for electronic applications and n-type wafer anodization is usually studied for combining porous silicon with other electronic components. Precise control of the doping range increases the wafer manufacturing costs exponentially. When manufacturers sell a batch of wafers, they advertise a resistivity range for each of the wafers in the batch. We have observed that 1 Ωcm and 20 Ωcm wafers may have very different etch morphologies even though the anodization conditions are kept the same. Illumination intensity affects the hole injection rate by creating e-h pairs and is vital for n-type wafer anodization. The other important parameters are anodic current density and HF concentration. As discussed in the section on PS etch mechanism, the necessary current density can be determined by looking at the IV relationship. PS typically forms at low current densities in highly concentrated HF solutions in order to limit surface oxidation. Since fluoride ions are the major contributors to H_2SiF_6 formation and Si

dissolution, HF concentration is a key parameter. The secondary parameters are the amount of surfactants and oxidizers added to the solution. Both parameters affect the electrochemical etch rate and may result in a transition from nanopores to micropores. The physical design of the anodization cell, which will be discussed in the next section, may also affect the porous surface drastically.

Etch Setup

The most important component of the etch setup is the etch cell. The design of the etch cells can have a huge impact on the morphology of the etched layer. All of the parameters discussed above depend strongly on the etch cell and may change even if simple modifications are made to the cell. Since frequent use of the cell with acidic and organic solutions can damage the surface of the cell, a durable material, high density polyethylene (HDPE), is prepared in a machine shop in order to form the body of the cell. A viton gasket of various sizes (an opening area of 3-7 cm^2) is put between the wafer and the etch cell so that the solution does not leak and the wafer is not broken during the clamping process. However, viton gaskets may soak up etch solution for very long etch durations (over 1.5 hr), loose flatness, and may cause leaks. One electrode (anode), the back plate, is an aluminum foil covered flat steel piece and it is fixed onto the back of the Si wafer during the etch process. The aluminum foil serves the purpose of protecting steel back plate and has to be renewed frequently to ensure a good contact between the back plate and the Si wafer. The counter electrode (cathode) is usually made of platinum (Pt) or gold (Au) due to their inertness in the corrosive electrochemical etch solutions. The cathode may be a Pt wire or a planar piece of Pt. Although many research groups use Pt wire we have observed that large planar pieces of Pt as the counter electrode serves a better purpose to achieve etch uniformity over the whole anodized area.

The two different types of etch cells used in the majority of the anodization experiments described in this thesis are shown in Figure 2.11. The first type of cell is

used for etching n-type wafers (Figure 2.11 (a)). It allows both front side and back side UV illumination during the etch process. N-type wafers don't have enough holes to take part in the PS formation process and need an external light source to excite e-h pairs. Front side illumination usually gives rise to nanopore covered micropores as compared to just micropores with backside illumination [27]. A mercury lamp of 365 nm UV source is used for illumination. The counter Pt electrode (cathode) is fixed to the top of the cell after filling with etch solution. The whole etch cell is boltled together as depicted in Figure 2.11 (a).

The cell used for anodizing p-type wafers is shown in Figure 2.11 (b). In this configuration, the back plate and the etch cell are clamped together with a c-clamp. The Pt electrode is fixed onto the cell with torr seal about 1 cm away from the anodized wafer. The platinum electrode has to be as flat as possible and directly face the Si wafer. In earlier experiments, with a Pt electrode free to move at the bottom end and we observed non-uniformity in the pore dimensions on the anodized Si surface. An SEM image in side view of a PS sample anodized in this configuration is shown in Figure 2.12. The sample area is diced into halves as an SEM analysis of the side view of the area from center to edge of the anodized region (Figure 12 a-c) is depicted. As can be clearly seen from the SEM images, the pores in the etched area are shallower at the center and deeper at the edge. Pore depths vary from 1 μm at the center to 10 μm at the edge. Another reason for obtaining non-uniform etches as shown in Fig. 2.12 is the over-clamping of the wafer to the cell. As a result, the stress induced along the edges of the opening in the viton gasket may cause faster dissolution of Si along these edges, leaving shallower pores at the center. In an extreme case, it is possible to brake the Si wafer during clamping. This etch cell has a recess bottom where a small magnetic bar can be placed to stir the solution. In this way, one can prevent the sticking of H_2 bubbles onto the surface and increase mass transport in the etch solution and improve etch uniformity. Circulating the solution may also help uniformity. Even some researchers suggest using an ultrasonic

bath during the electrochemical etch to get a more uniform pore structure, finding that a higher vibration frequency results in larger pore diameters [28].

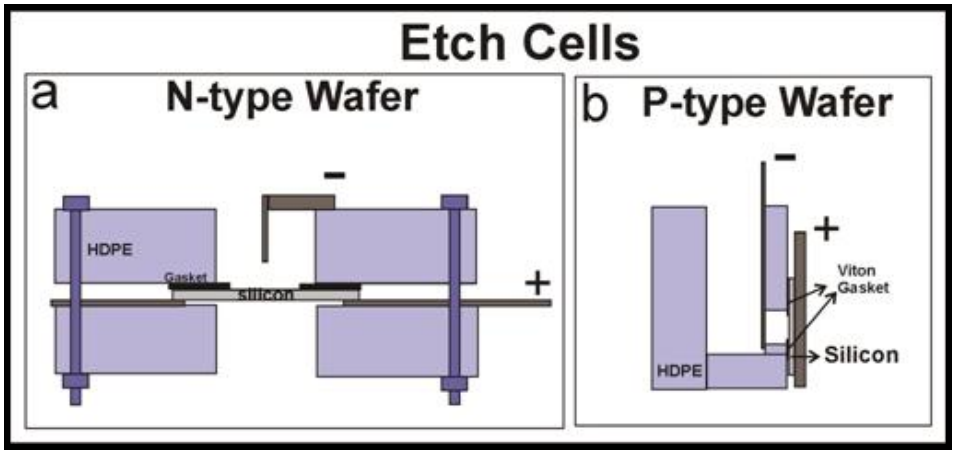

Figure 2.11. Etch cells used in anaodization experiments are illustrated. a) N-type wafer anodization cell. b) P-type wafer anodization cell.

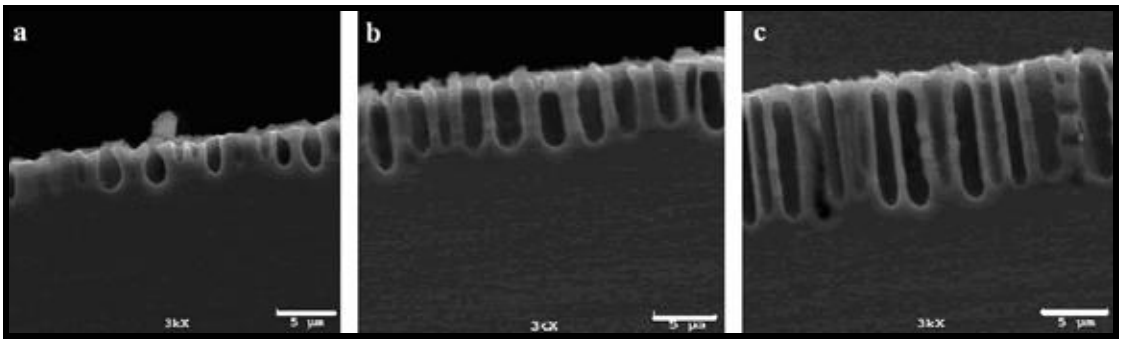

Figure 2.12 depicts SEM images of a non-uniform etch. a) SEM micrograph of a side view of the central region of a PS film. b) SEM of a side view of the intermediate region between center and edge of the porous film. c) SEM of a side view of the edge of the porous film.

All of the experiments are performed in constant current mode using an Agilent 66348 System DC Power Supply, which can deliver a maximum of 100 V and 1A. A labview program written by Steve Lewis [9] is used to control the power supply through a GPIB card for most of the anodization experiments. It is possible to set a current and a duration for the anodization period via the Labview code. For p-type wafer anodization, the applied current ranges from 1-10 mA/cm^2 as opposed to 50-150 mA/cm^2 for an n-type wafer anodization experiment. When the electroless solution is highly resistive, the

power supply may not be able to provide enough current because it is restricted to a maximum of 100 V. One way of getting around this problem is coating a thin aluminum (Al) or nickel (Ni) layer on the back of the wafer to decrease the junction resistance between the back plate and the Si wafer. A Ni coating (MG Chemicals Super Shield Nickel Conductive Coating) is used in some experiments. The full curing of the Ni layer takes about 24 hrs. [29]. After each experiment, the etch cell is washed with DI water completely to prevent any sort of contamination. Using the same cell for extended periods may cause loosening of the Pt electrode in the p-type etch cell. The position of the Pt electrode has to be inspected regularly and the Pt electrode has to be fixed with torr seal when necessary. One has to wait for a day for the curing of the torr seal. It is usually a good practice to run a few initial experiments with redundant wafers since some effluents can desorb from the torr seal into the solution in the first few runs just after fixing the Pt electrode with a new torr seal every time.

Hybrid Surface

Porous silicon interfaces for sensor applications are generated by electrochemical anodization of 7–13 Ω cm, p type (boron doped), (1 0 0) silicon wafers (Siltronix). The anodization is done in 1 M H_2O, 1 M HF and 0.1 M tetrabutylammonium perchlorate in acetonitrile at 3 mA/cm^2. The process results in a hybrid surface (nanopore covered microprous structure) [31,32]. After the anodized sample is cleaned in acetonitrile for 10 min to purge any residue in the pores from the etch solution, it is immersed in dilute HF and then placed in MeOH. The typical pore depth is 10–30 μm (Fig. 2.13 (a)) and the porous film has a typical porosity of 50–80%. The pore diameter varies from 1 to 2 μm (Fig. 2.13 (b)) [33]. The micropores are cylindrical in shape with a conical termination at the c–Si interface of the anodized wafer. The micropores are aligned in the (100) direction. SEM images of the structure of a porous silicon film shows that nanopore dimensions in the inner surface of micropores vary from 1-100 nm (Fig. 2.13 (b)-(c)). It

is not easy to determine the onset of the nanopores covering the cylindrical micropores with the SEM since the electrochemical etch increases the surface roughness at the nm scale. The hybrid etch practically increases the reactive surface area of the sensors as opposed to microporous etch. Thus, it increases a sensor's response. The nanoporous surface of hybrid etch enhances the amount of charge trapped on the surface as it generates additional interaction sites and consequently also contributes to the response.

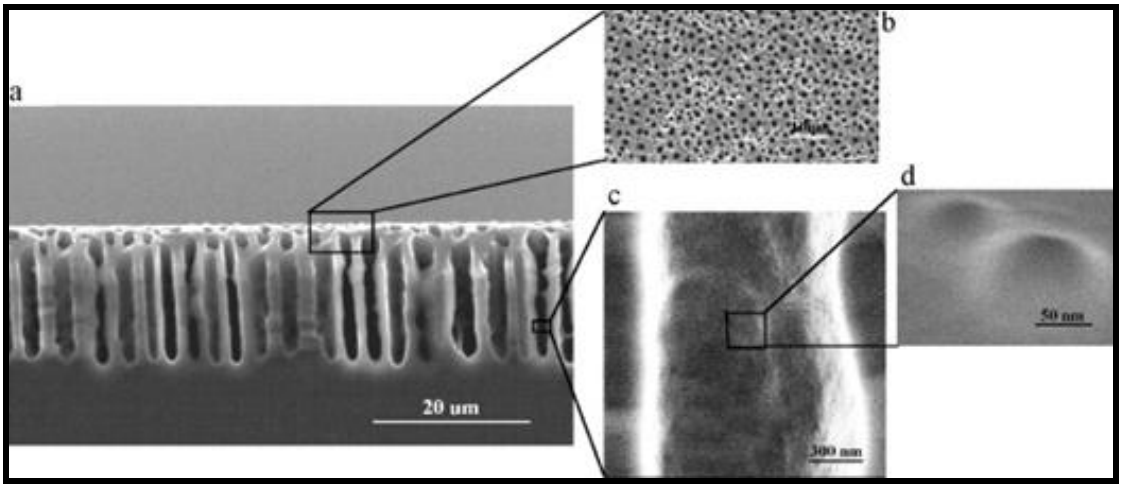

Figure 2.13. (a) Side view and (b) top view of micropore structure, (c) micropore side view at a higher magnification, and (d) SEM images of a porous silicon etch within the silicon micropore.

A PS surface generated from an n-type (1-20 Ωcm, phosphorous doped) wafer (100) (Wafer World Inc.) is shown in Figure 2.14. This surface is anodized in HF:EtOH (1:1) solution for 10 minutes under front-side UV illumination and subsequently cleaned with MeOH after the anodization. Some of the samples freshly prepared using this method were partially covered with oxide and therefore were placed in dilute HF:MeOH (1:20) solution for a few hrs after anodization. The porosity of this sample is lower than that of the hybrid etch. Pore diameters on the surface vary considerably. Pores which have less than a 50 nm diameter have been detected. The average pore diameter is less than 500 nm (Figure 2.14 (a)-(b)). The top surface SEM image shows mostly square and some circular pore openings. The edges of the square openings lie along the (110)

direction. Pores nucleated close to each other start to merge and take various shapes at some surface sites. On the other hand, the etch rate is faster, and the pore depth is over 100 μm for a 10 min etch. The pores penetrate directly into the (100) surface (Figure 2.14 (c)). On the surface of these pores, there are intermittent branches of various lengths (Figure 2.14 (c)). This type of surface is less suitable for sensor applications because of the narrower pore openings and decreased porosity.

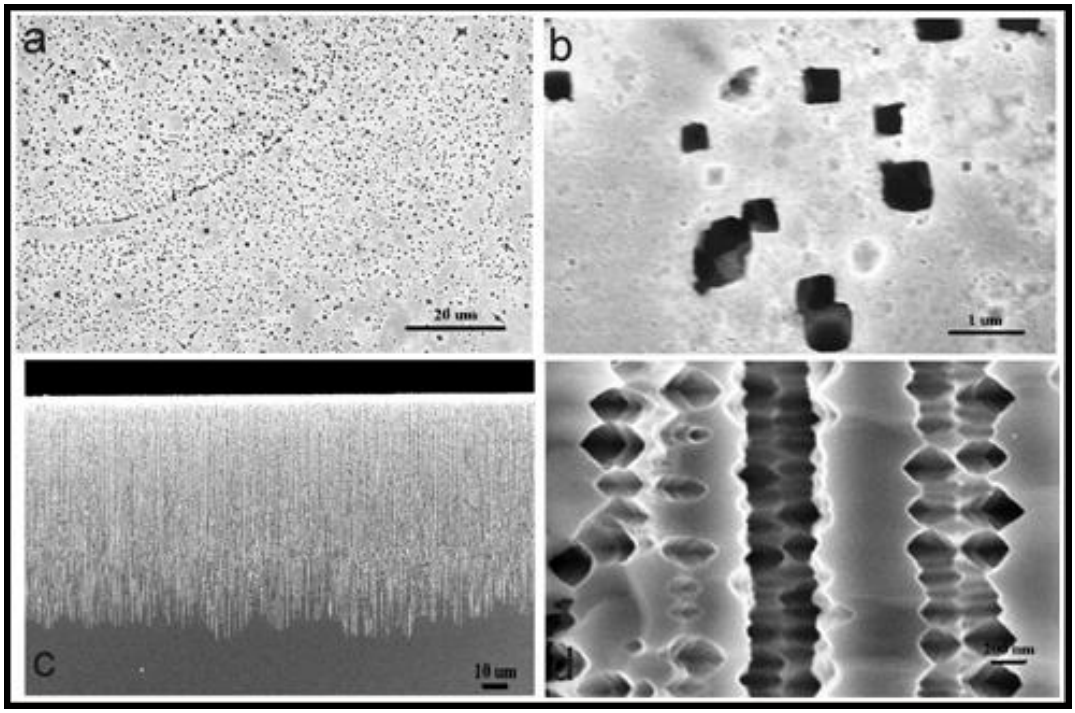

Figure 2.14. Pore sizes decrease when etching occurs under illumination. a) An SEM image of a top view of PS at a low magnification. b) An SEM image of a top view of PS observed at a higher magnification. Square pore openings have an area less than 1 um^2. c) SEM images of a cleaved cross section of the surface. The pores are penetrate directly into the (100) surface (Figure 2.14 (c)). d) On the surface of the pores there are intermittent branches of various lengths.

Porosity

Porosity is an important parameter that affects the sensing properties of the sensor. We have observed that porosity tends to increase with the HF concentration and the applied current as well as the anodization duration. It is usually measured by gravimetric methods. One way to calculate the pore volume or void content is by

measuring the weight of the wafer before and after anodization and dividing by the silicon density (d_{Si}=2.329 g/cm^3). Any physical or chemical contaminants that may form on the surface during or after the anodization step have to be stripped before the final weight measurement [33]. Porosity may also be checked with reflectometry. Porosimetric ellipsometry is used to measure the optical properties of a material which depend on the pore size, thickness, and porosity. This method is even sensitive to porous films which have a thickness of 10 nm. [34].

Another method has been developed to get a rough idea about the nanoporous coverage on the hybrid PS surface. The SEM image of a top surface is analyzed with Matlab to calculate the percentage of the total surface coverage. Since pore nucleation starts on random sites on the surface, a top surface SEM image is a good representsentation of the average pore coverage on the entire anodized surface. The areas where pores nucleate have a high contrast with respect to the flat Si surface in the SEM image (Figure 2.15-left). We assign a threshold value for the contrast and transform the image to black and white (Figure 2.15-right). After that, we need count the number of pixels which are "black" and calculate the ratio of black pixels to the total number of pixels on the image using Matlab. The code written for this calculation is in Appendix III. The ratio is 0.3925 for the image in Figure 2.15. We can also check the average pore depth via SEM. The average pore depth (~20 μm) multiplied by the surface coverage ratio and total anodized area gives a rough estimate for the total microporous void volume. This method especially works with smooth microporous surfaces. However, there are nanopores on the micropores on a hybrid surface. One can use this method in combination with the gravimetric method to calculate the void volume corresponding to the nanopores. By subtracting the microporous void volume calculated by matlab analysis from the total void volume which is calculated by the gravimetric method gives an estimate for the total nanoporous volume.

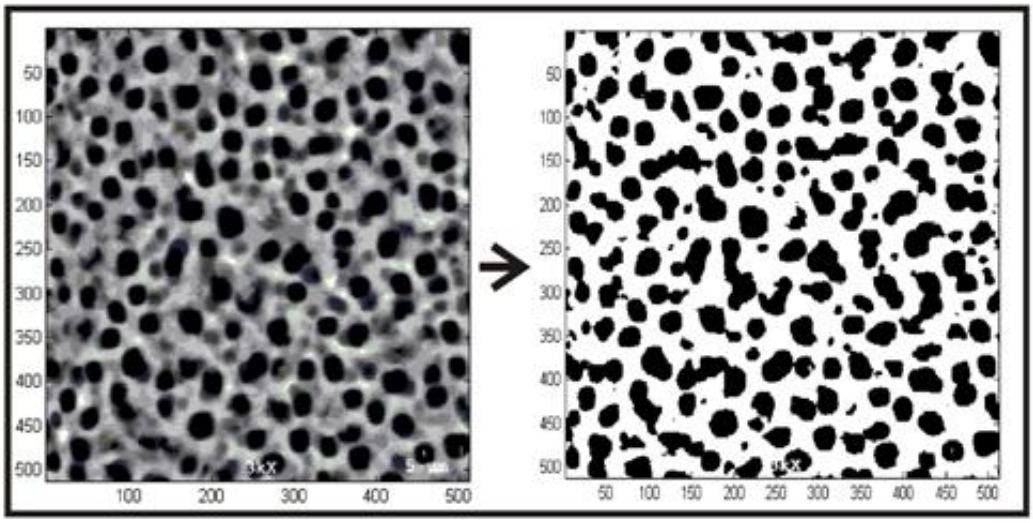

Figure 2.15. Image processing of the SEM image of a PS surface to calculate porosity is shown. Left: Real SEM image of the surface. Right: The image is transformed to black & white by assigning a threshold value for the contrast. The ratio of black pixels to the total number of pixels is calculated by Matlab. The ratio is 0.3925 for the left image. Surface coverage ratio is 0.3925.

Porous Net, Coatings, Filters, Needles, Sponges

Pore size and shape usually determine the application area of PS. There are several pore morphologies, such as cylindrical, funnel shape, square, and triangular and several pore sizes which all have been reported [35]. Pore growth direction depends on the crystal orientation of the wafer and growth rate depends on the doping level. In some cases, branching of the pores occurs. In this section, some interesting morphologies realized in the anodization of different PS samples are discussed. Figure 2.16 shows some of the anomalies observed in p-type anodizations. Figure 2.16 (a) shows a PS net. This sample was anodized at a high current 6 mA/cm^2 and the resulting surface was highly porous. The sample was left in HF:MeOH (1:10) solution for few days to get rid of the partial oxidation on the surface. The resulting surface corresponds to a network of pores. It appears that the top layer of the porous film is etched in the horizontal direction faster than the bottom layer. As a result, the pore openings on the top surface begins to merge. On the other hand, the vertical etch rate (R_v) at the bottom of the porous layer is still much faster than the horizontal etch rate (R_h). In Figure 2.16 (b-c), we depict SEM

images of the surface coverage with Si/SiO2 flakes in two different magnifications. These flakes seem to be formed by cracking and peeling from the top surface later. EDS measurements were done on the surface to investigate any sort of contamination. The two peaks observed are a Si peak (1.7 keV) and a stronger than usual O peak (0.5 keV). The flake dimensions observed in similar experiments seem to vary. Soaking the sample for in a diluted HF:MeOH (1:20) solution results in stripping of the surface coating in most cases.

Jenna Campbell and Dr. Jimmy Corno began working on the development of PS filters in the Gole laboratory [13,14]. An example is depicted in Figure 2.17. Campbell et. al. claims that after an initial pore propagation in the (100) direction, the bottom of the pores start to expand increasing the pore tip radius [13]. This is the exact opposite of the process described in Figure 2.16 (a). In filter formation, the horizontal etch rate at the bottom of the pore starts to increase catching the vertical etch rate. When the pore radius becomes comparable in length to the initial pore spacing, the bottom layer of the film becomes fragile. If the etch is stopped at this point, the film can be easily scraped from the Si wafer using a razor blade. If the etch process is continued, the pore expansion results in the lift-off of the porous film and porous sections can easily be observed by the naked eye in the etch solution. In most experiments, there is also the possibility of a white foam formation due to the high level of oxidation on the surface. Campbell et. al. reported good control of the film thickness. However, the problem with this process is that film formation does occur on partial regions, not on the whole anodized surface. Therefore, finding a way to control the area of the PS film is still not clear and under continued investigation. One way to attack this problem is to change the applied current during the anodization process. In this way, it is possible to control the thickness and uniformity on the anodized area by sending shock currents, very large compared to the pore propagation current, when the micofilter area is close to the final lift-off stage. For this purpose, the original Labview code written for one current step by Dr Lewis is

modified (The details of the code can be found in Appendix IV). This Labview code will be especially useful for researching different pore morphologies and various types of filters.

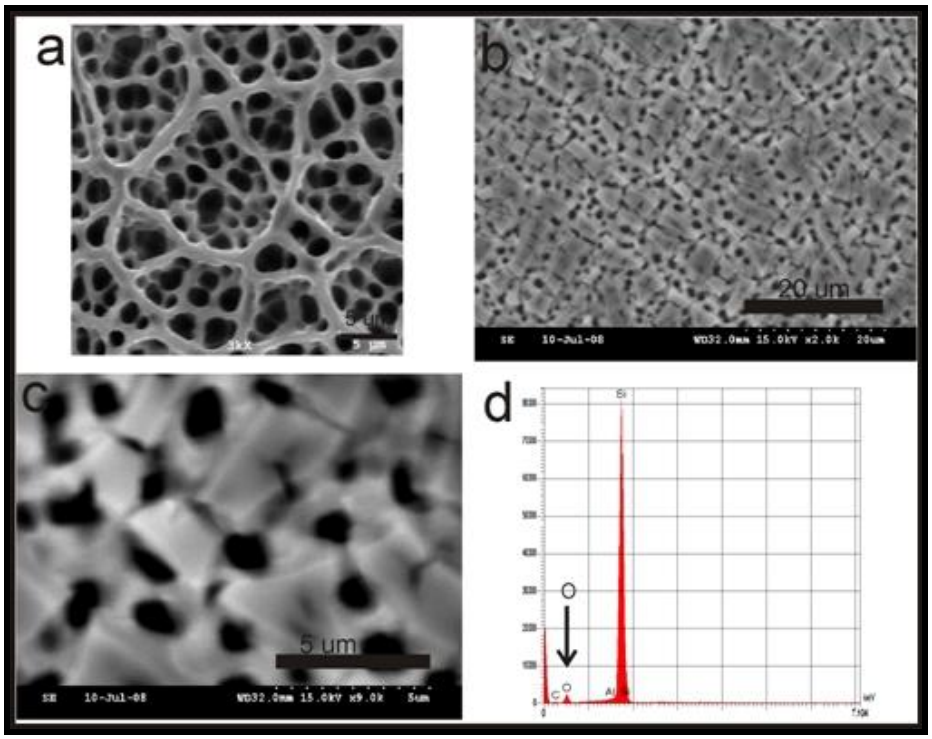

Figure 2.16 (a) A PS net. (b) PS is covered with oxidized silicon pieces. (c) A higher magnification of the surface depicted in (b). (d) EDS measurement done on the same surface which shows a strong O peak.

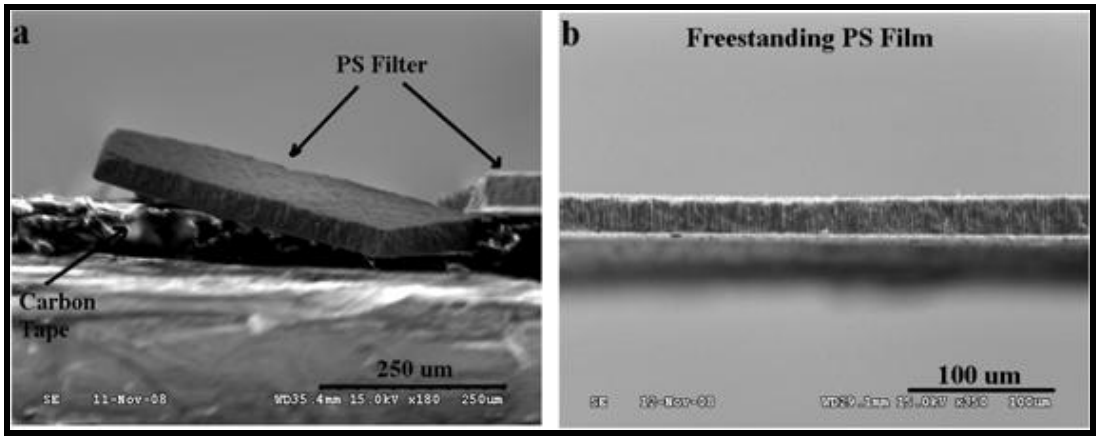

Figure 2.17 Porous filter films. a) SEM image of side view of PS filter. A ~ 500 μ x 500 μm film is broken on the carbon tape due its fragile nature. b) An SEM image of a freestanding PS film is depicted. Film thickness is about 50 μm. For closeup views, see Ref-13.

An anomaly in a PS etch is depicted in Figure 2.18. This sample is anodized in HF:MeCN (1:20) solution with 8mA/cm^2. The middle figure shows the peeling off of the porous layer in the central region of the anodized surface. The high porosity top surface shows triangular and square pore nucleation sites. A number of steps on the top surface are clearly observed. Step heights are about 10 μm. A closer view of the steps shows a porous ramp formation where pore propagation direction is not in the (100) direction for any pore. Porous films of various steps heights can be useful in Bragg reflectors or PS photonic crystals.

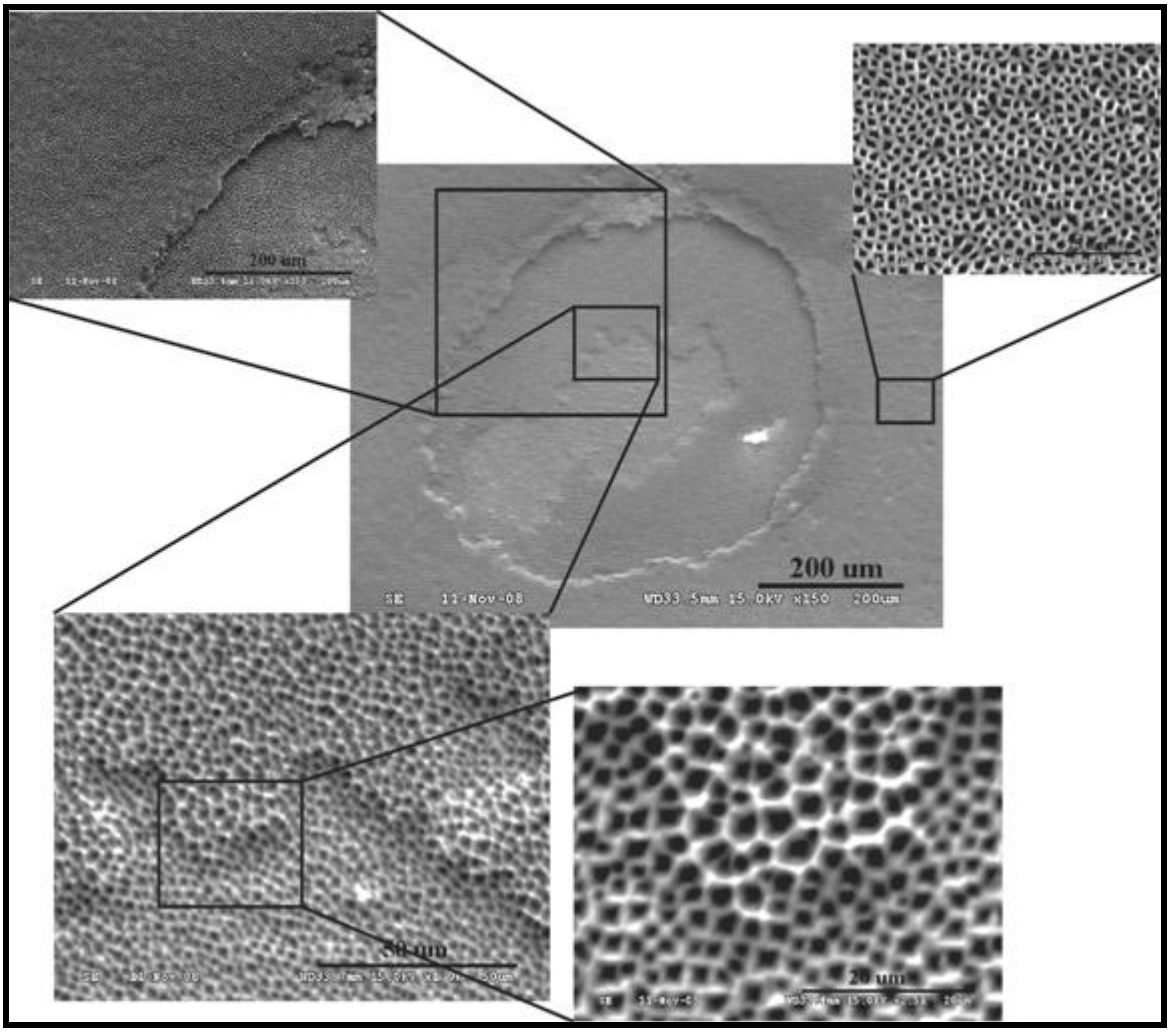

Figure 2.18. SEM images of a number of porous steps (ramps) on the same anodized highly porous surface.

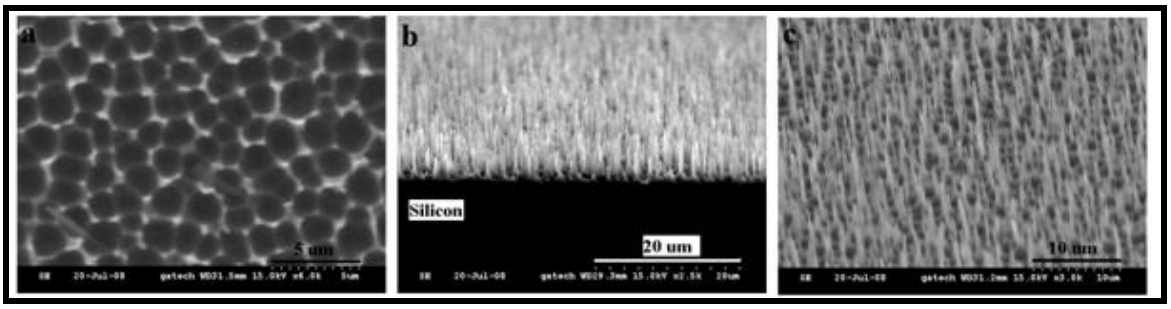

Figure 2.19 SEM images of needles formed in an electrochemical etch. a) Highly porous top view. b) Side view. Needles are about 10 μm in length. c) SEM images of side view of needles taken at an angle.

In Figure 2.19 SEM images of needles formed in an electrochemical etch are depicted. Figure 2.19 (a) shows a very highly porous top surface. Pore walls are very thin. Figure 2.19 (b-c) shows a side view of the same layer. The needles have a length of 10 μm and tips of the needles are in nm size. A similar study was reported by Giuly et. al. [36]. In this publication, the formation of needles (~1 μm) was achieved by dipping shallow high porosity PS in an ultrasonic bath breaking pore walls. High density porous films are mechanically weak. A tensile force can easily break the pore walls. The drying of PS, ultrasonic bath treatment or hydrogen bubble formation at high levels may break or crash the thin walls of the high porosity PS (Figure 2.19 (a)), resulting in a similar structure. In this study, longer needles (10 μm) were realized in a one step electrochemical etch of silicon. It has been observed that stirring the solution with a magnetic bar at much faster speeds aids the needle formation. This kind of needle structure may be useful in various application areas. The surface of the needle can be smoothened by plasma processing and this surface might be functionalized after a thin layer of gold deposition. Nanoneedles garnered a great deal of attention for cell membrane manipulation including adding a gene or a protein inside cells. However, fabrication methods proposed for Si nanoneedle patterning may have many complicated steps [37]. Electrochemical etching serves as a, simple one step alternative for nanoneedle fabrication.

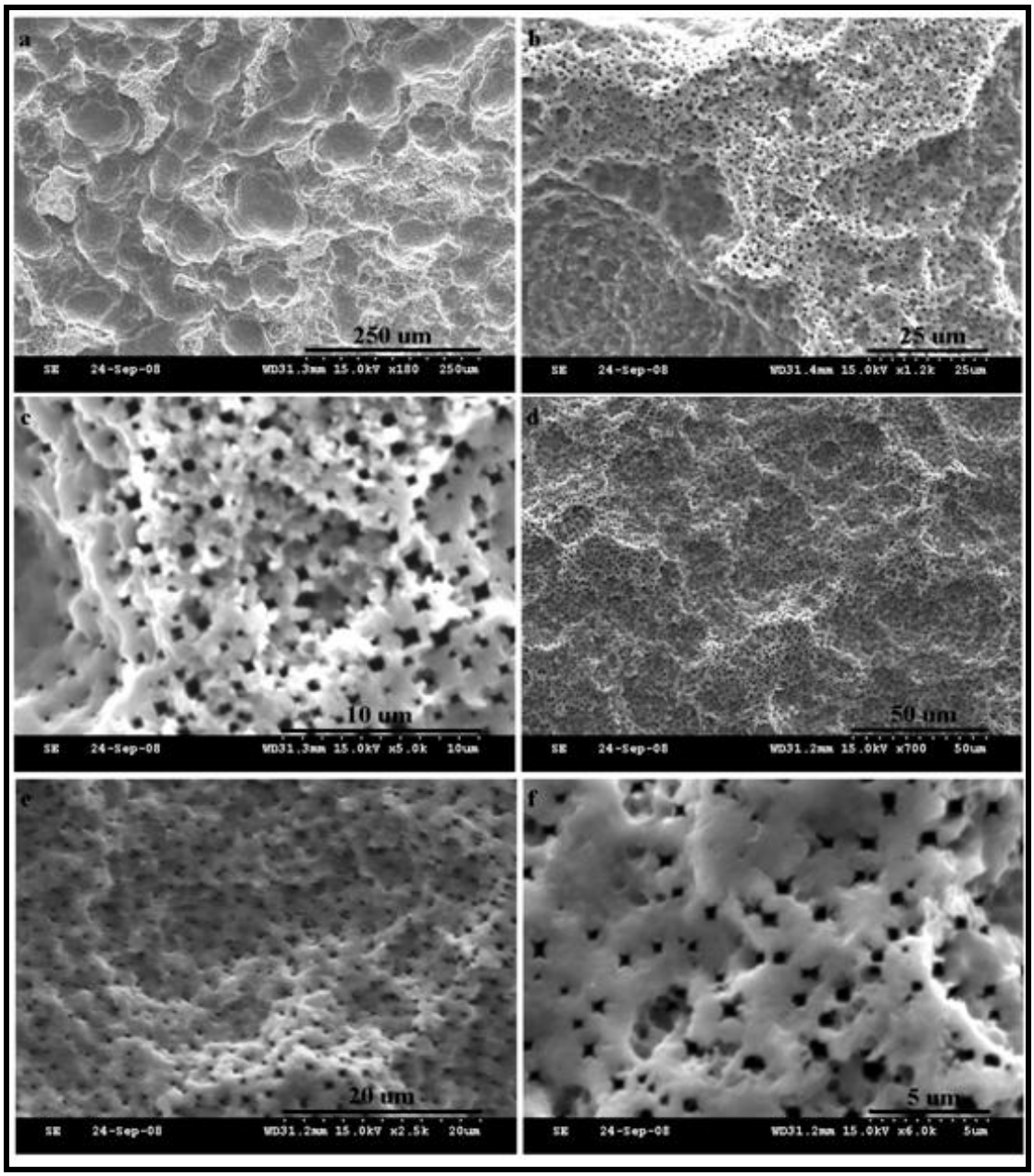

Figure 2.20 Top view SEM. Sponge structures from two different samples: Sample 1 (a-c), Sample 2 (d-f). The majority of the pore diameters are less than 500 nm. The surface is highly photoluminescent and orange in color.

A sponge structure (from two different samples), named after sea sponges because of their resemblance, is depicted in Figure 2.20. The silicon surface is very rough compared to the previously discussed anodization experiments which have pore

formation on a smooth Si surface. The surface is highly photoluminescent and orange in color. The wafer (p-type, (100)) was anodized in HF:MeCN (1:30) solution at 4 mA/cm^2. Pore sizes vary on the surface from 50 nm to 1μm. The structure looks like conglomerates of layers. PS sponges may be used for trapping biomolecules or bacteria inside. A similar application of porous aerogels which are used as biosensors to detect viral particles by bacterias immobilized in its pores is discussed in Ref-38.

2.3 Microfabrication

Microfabrication of the sensors is performed in the MIRC Cleanroom at Georgia Institute of Technology. It requires a 5 step process: SiC deposition, photolithography, reactive ion etching, electrochemical anodization, and metallization.

2.3.1 Silicon Carbide (SiC) Deposition

For the local formation and patterning of PS, SiC is an excellent etch mask. SiO_2 cannot be used as an etch mask to create sensors from PS because of the high dissolving power of HF. SiC and Si_3N_4 are good candidates as etch masks. SiC has an etch rate of a few Å per minute ~ 1/10 that of the etch rate of Si_3N_4 in the hybrid etch solution [39].

Before the PS anodization step, the Si wafer is cleaned in HF (49 %) and a SiC layer (~2000 Å in thickness) is coated onto the polished surface by plasma enhanced chemical vapor deposition (Unaxis PECVD in MiRC cleanrooms [40]). The thickness of the SiC layer is chosen to be less than 2000 Å so that the gold deposition in the metallization step will have electrical continuity between PS and the measurement pads. The color of the SiC layer is dark green/blue. The deposition duration is about 20 minutes. The thickness variation of a SiC layer is depicted in Figure 2.21. The average thickness is 1771 Å with a standard deviation of 16.6 Å with very good uniformity. Before each deposition, a chamber cleaning recipe is run for an hour to prevent any type of contamination. The Unaxis PECVD is also used for coating the oxide and nitride

layers. Any oxide contamination in the SiC layer due to an initially contaminated chamber will cause partial dissolution of this layer during the electrochemical etch. In each run, four 2" wafers are deposited with SiC.

PECVD utilizes a plasma to enhance the chemical reaction rate of the precursors. One advantage of PECVD is the availability of low substrate temperatures compared to other CVD techniques. A radio frequency (RF) plasma is used to replace thermal energy as the energy source needed for chemical reactions. In the reaction chamber, the reactants are adsorbed onto the silicon wafer surface, undergo a chemical reaction, and the products migrate forming a film. SiH_4 (5 % in He, 300 sccm), He (700 sccm) and CH_4 (100 sccm) gases are used to deposit SiC at 250 ^{0}C. The process pressure is 800 mTorr and the applied power for plasma initiation is 50 W.

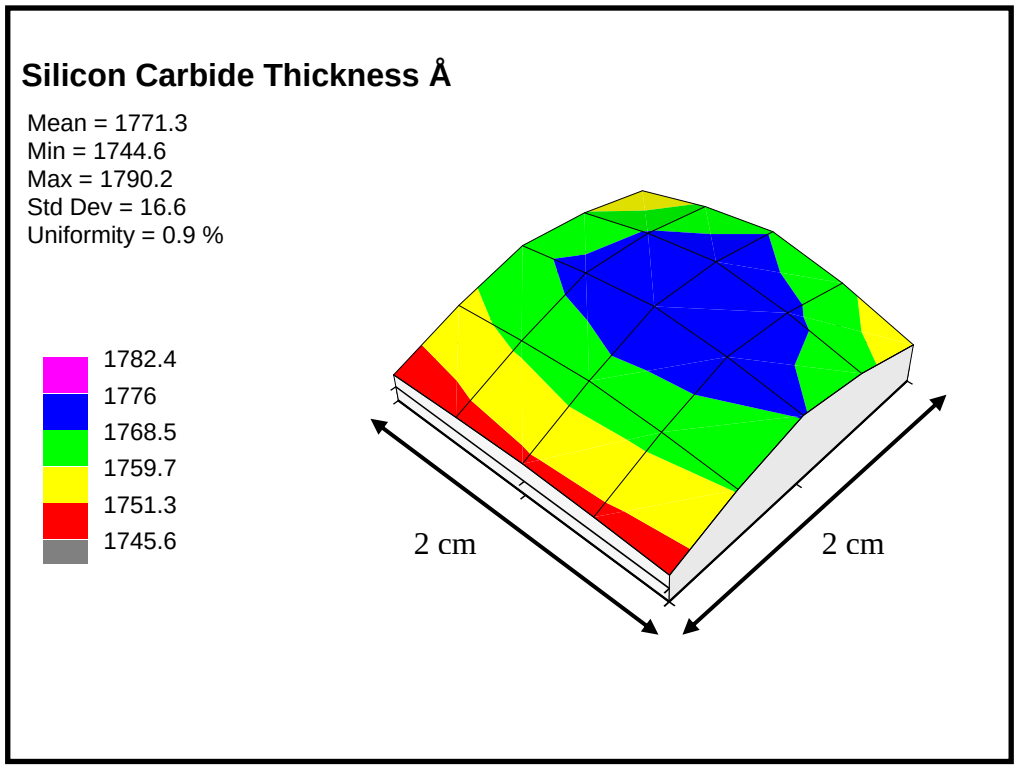

Figure 2.21 Thickness variations of SiC deposited on Si in Unaxis PECVD in Mirc at Gatech. The measurement is taken by an ellipsometer. SiC is used as the masking layer since it is highly durable in HF-containing solutions.

2.3.2 Photolithography

The patterning of the SiC layer is done via photolithography. Photoresist is a photosensitive polymer. When it is exposed to UV light, bonds in the polymer either weaken (positive resist) or strengthen (negative resist). A positive photoresist, Microposit 1827 from Shipley Co., is used for photolithography. The wafer surface is covered with photoresist at a spinning rate of 3500 rpm for 30 s to ensure uniform coverage. The photoresist thickness is inversely proportional with the square root of the spin speed. A thinner photoresist layer is better for patterning smaller features. An adhesion promoter (e.g. HMDS) is not used for the process. At the soft bake stage, the wafer is heated at 95 ^{0}C for 2.5 minutes. This step hardens the photoresist, increases adhesion, and prepares the wafer for exposure. A Karl Suss MA-6 Mask Aligner is used to expose the treated wafer [40]. This mask aligner uses a mercury lamp as a UV source. It has two channels calibrated to 5mW/cm^2 at 365 nm and 20mW/cm^2 at 405 nm. 200 mJ/cm^2 is a good dose level for exposure. A schematic of the mask used in the process is depicted in Figure 2.22. 12 sensors are produced on each wafer as the final product and each sensing area is 2mm x 5 mm. Chrome covered areas on the mask do not allow UV to pass through and in this way certain areas of the photoresist are exposed to UV selectively. After the exposure, the photoresist is developed in Microposit MF 319 developer for about 30 sec. UV exposed areas of the photoresist dissolve in the developer solution. After this step, the wafer is cleaned with DI water and hard baked at 120 ^{0}C for 10 min. The post bake step removes adsorbed water, and any traces of solvent or developer from the photoresist. It also hardens the surface and prepares it for a wet or plasma etch. It also eliminates any bursts in the vacuum chamber. The next step is reactive ion etching for the patterning of the SiC through openings in the photoresist.

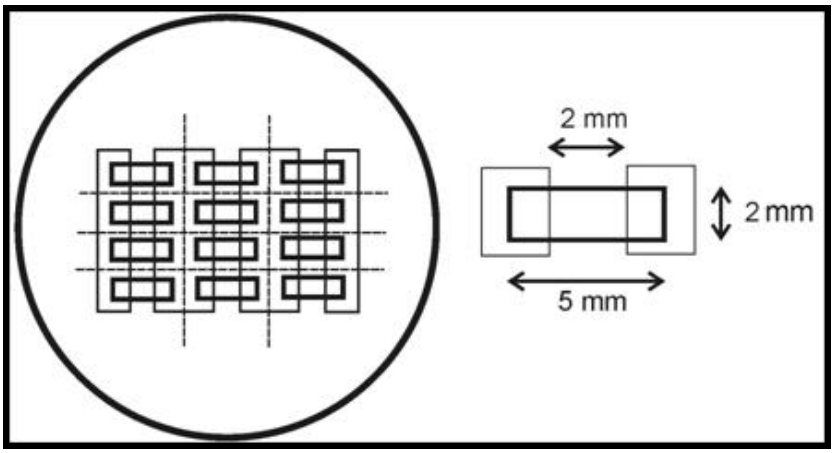

Figure 2.22. Left: Schematic of the mask used for optical lithography. The final process produces 12 sensors. Dashed lines represent the dicing paths. Right: The physical dimensions of one sensor are given.

2.3.3 Reactive Ion Etching (RIE)

The basic steps in a reactive ion etching (RIE) are adsorption of the chemical species on the surface, chemical reaction, and desorption of products from the surface. Plasma etching is anisotropic and it has a low selectivity compared to chemical etching. An ordinary plasma produces energetic free radicals that attack the surface physically and knock out atoms by momentum transfer. In RIE, the plasma is chemically reactive with the surface. RIE may also be used for eliminating roughness on the micro pore walls to create smooth pores. The RIE process is done in a Plasma-Therm RIE [40]. The gases used in the process are Ar (10 sccm), O_2 (7 sccm), and SF_6 (13 sccm) at a total pressure of 60 mTorr. The RF power used is 200 W. The photoresist blocks the plasma from attacking the covered areas on the surface, acting as a mask. 2mm × 5 mm windows are opened in the SiC layer after the RIE process. It takes approximately 1 min to etch 2000 Å of SiC. The etched regions are inspected via a Nanospec Refractometer for any residue of SiC. After the SiC layer is etched entirely from the unmasked regions, the photoresist is stripped off in acetone. When necessary, putting the wafer in an ultrasonic acetone bath aids the removal of sticky photoresist.

2.3.4 Porous Silicon Etch

After the SiC layer is patterned, the PS anodization is done as explained in the previous section. This is the most important step of fabrication. After this process, a gas sensitive layer is formed in the SiC openings.

2.3.5 Gold Deposition

The next step in the process is gold metallization for electrical contact and measurements. It has been observed that any use of photoresist on the PS surface after the anodization step degrades the PS sensor performance [9]. For this reason, shadow masking techniques are utilized for metal deposition. All metallization processes are performed in a CVC E-beam Evaporator [40]. In an e-beam evaporating system, the pure metals which will be evaporated onto the wafer surface are kept in crucibles and heated by electron beams diverted onto the crucible by magnetic coils. The wafer is mounted above the crucible and there is a shutter in between to control the amount of condensation on the wafer. The operating pressures are chosen below 10^{-7} Torr to prevent any type of contamination. After the anodization process, a gold layer (3500–5000 Å) is coated onto the sensor following an initial Ti layer (~ 200 Å) deposition used to obtain better adhesion. The shadow masks of various dimensions for different porous layers are shown in Appendix V. The shadow masks are made from stencils by laser cutting and ordered from Stencils Unlimited Inc. [41].

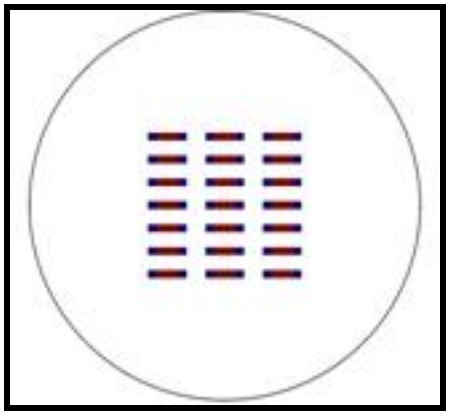

Figure 2.23 A schematic of the shadow mask for the gold deposition step.

After the metallization step, the sensors are diced into individual sensors (See Figure 2.22 for dicing paths). A schematic of the sensor (Figure 2.24-Left) and a photo of a real sensor (Figure 2.24-Right) are shown in Figure 2.24. The resistance change of the porous layer is measured via precision microprobes. The base resistance variation of sensors fabricated on the same wafer is depicted in Figure 2.25. The mean resistance of this batch of sensors is 906 Ω with a standard deviation of 179 Ω.

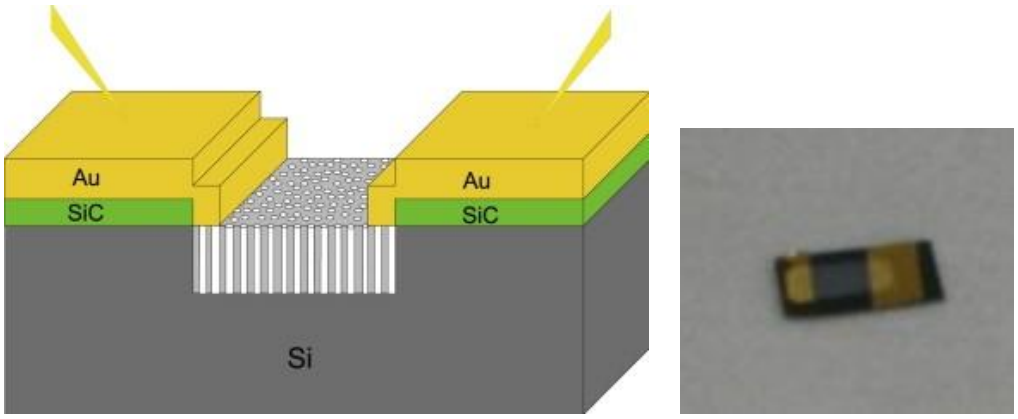

Fig. 2.24. Left is a Porous Si gas sensor schematic. The resistance change is measured via precision microprobes when the porous silicon interface is exposed to a test gas. A SiC layer also serves as an insulation layer as the resistance response of the porous layer is measured through gold contacts. Right is a photo of a real sensor.

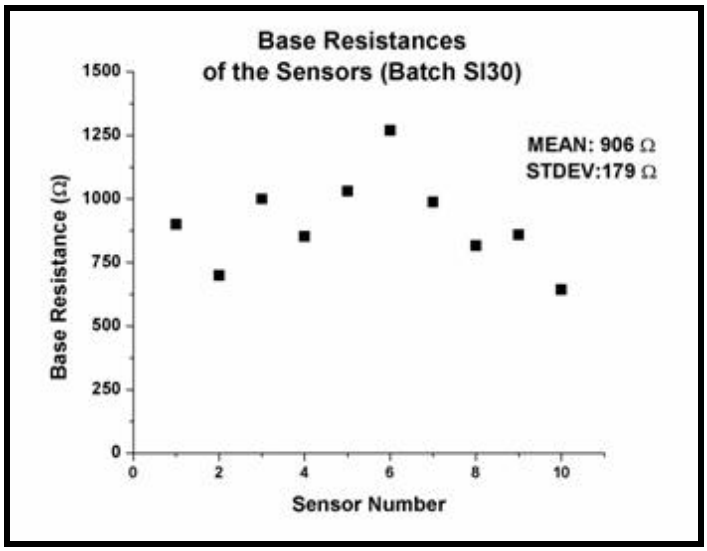

Figure 2.25 Variations in the base resistance of sensors produced from the same wafer. For this batch the mean is 906 Ω and the standard deviation of the base resistances is 179 Ω.

2.4 Gas Testing Setup

Various high quality test gases (NH_3, NO, NO_2, PH_3, SO_2, N_2 etc) are purchased from Mathesontrigas Inc. The majority of the tanks (size 3R) correspond to 1000 ppm of the gas of interest diluted in N_2. A separate MKS 1179 mass flow controller (MFC) is used with each test gas. The connections between the MFCs and the tanks are made with 1/8 inch stainless steel (SS) tubing. The SS lines are heated regularly to prevent any contamination. The MFCs are flushed with N_2 when they are not in use for extended periods. In an MFC, the flow is divided into two channels. It is measured in a small channel parallel to the major flow line by measuring the heat gradient, which varies as a function of mass flow, between the two ends of the channel. The flow levels of the MFCs are calibrated over the 10-50 sccm range for the test gases and 100-2000 sccm for the dilution gas (N_2). These calibrations are also checked with a separate mass flow meter (MFM). The MFCs are controlled by two types of power supply/read out systems; MKS 246 and 247. The MKS 246 power supply is a one channel system and the MKS 247 is a 4 channel system. In the majority of the experiments, the MKS 246 is computer controlled via a DaqPad 6015 (National Ins.) and a Labview program (Please see Appendix IV for details of the Labview Code). The MKS 247 is controlled manually and is used for the dilution gas, N_2. The flow of the dilution gas might be varied from 100-500 sccm. In all the experiments presented here, the mixing of the gases is performed in a mixing junction [9]. However, a mixing chamber is designed for future experiments to enable multiple gas mixing in a uniform, controlled way. The schematic of the designed system is depicted in Figure 2.26. The mixing chamber is cleaned with hexane to remove oil contaminants, and then DI water to rid the surface of water soluble contaminants. Diethy ether is applied as the drying agent. Before mixing the gases, this system enables the evacuation of the chamber through a mechanical pump. A MFM is used to measure the flow of the mixture onto the sensor. The entire experimental set up, except the N_2 gas tank, is kept in a chemical hood.

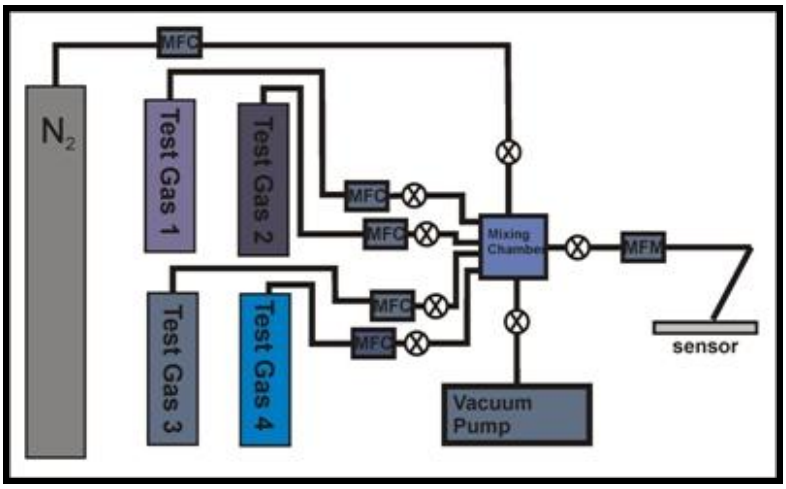

Figure 2.26 A schematic of the multiple gas testing setup (not to scale). 4 test gases may be diluted in a mixing chamber which can be pumped down initially.

The conductometric PS gas sensors typically operate in the 1–5 V range, but it is possible to use the sensors with a 100 mV or smaller bias voltage [9]. The voltage is applied and the current is measured using the DaqPad 6015. In Figure 2.27, a resistance measurement with the precision probes on an n-type sensor is shown. The test gas flows onto the sensor at a 45^{0} angle to ensure both penetration into the pores and the flow onto the sensors. The noise characteristics of the testing environment in a chemical hood have been evaluated in earlier studies [9].

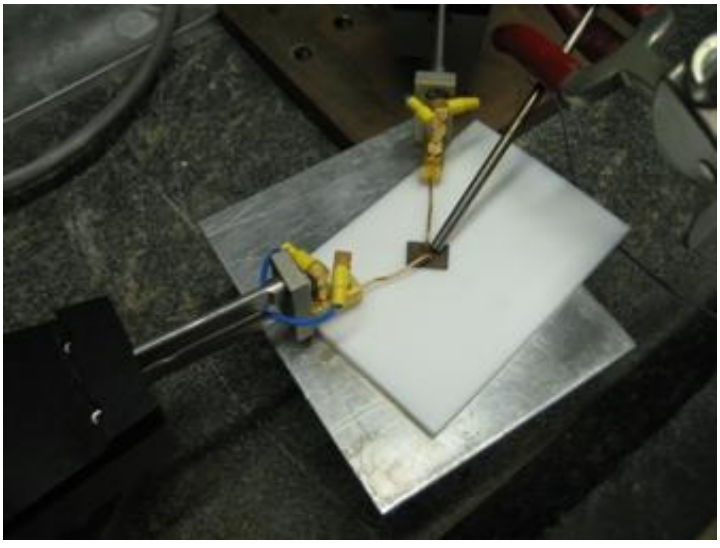

Figure 2.27. A photo of the resistance measurement on an n-type sensor is shown.

A portable measurement system which was developed by Dr Mark Jones is depicted in Figure 2.28. The advantage of this system is that an array of 4 or 8 sensors can be mounted on packages (Figure 2.28-Top left) and an array response can be used in identifying the concentration of gas in a better and more efficient way. The sensors are wire bonded to the packages with an ultrasonic wire bonder in the MIRC. Gold wires of 12 μm diameter are used for the wire bonding. The portable system does have an inlet and an outlet for inflow and the removal of the test gas. It can operate at 3 different pumping speeds. It can be battery powered, applying 3V across each sensors. It is computer controlled through a serial connection. The demonstration of this concept is shown Figure 2.29. A package of 4 sensors is used to measure an NH_3 response. The top graph shows the response to uncoated and gold nanoparticle treated sensors. The second graph shows the response to a tin treated sensor and the last graph shows the response of a NiO_x nanoparticle treated surface. While the untreated and gold treated surfaces show a good response, in this preliminary experiment, the SnO_x and NiO treated sensor responses exhibit some noise.

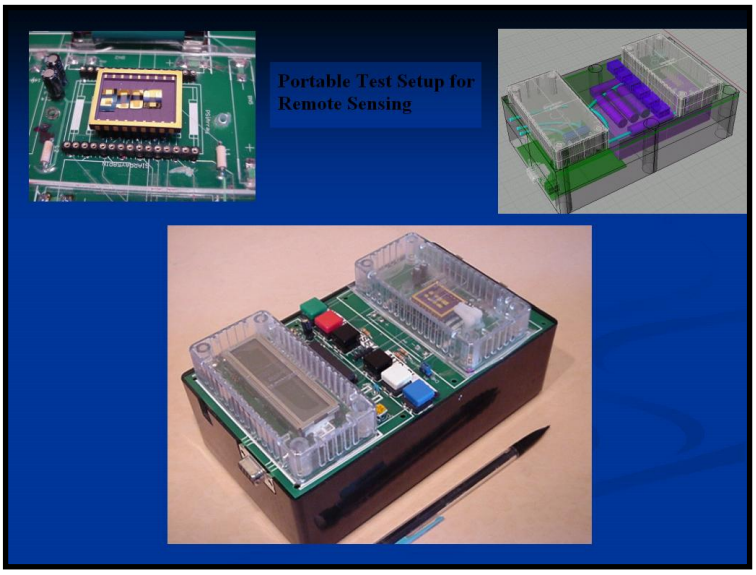

Figure 2.28 Portable remote sensing system.

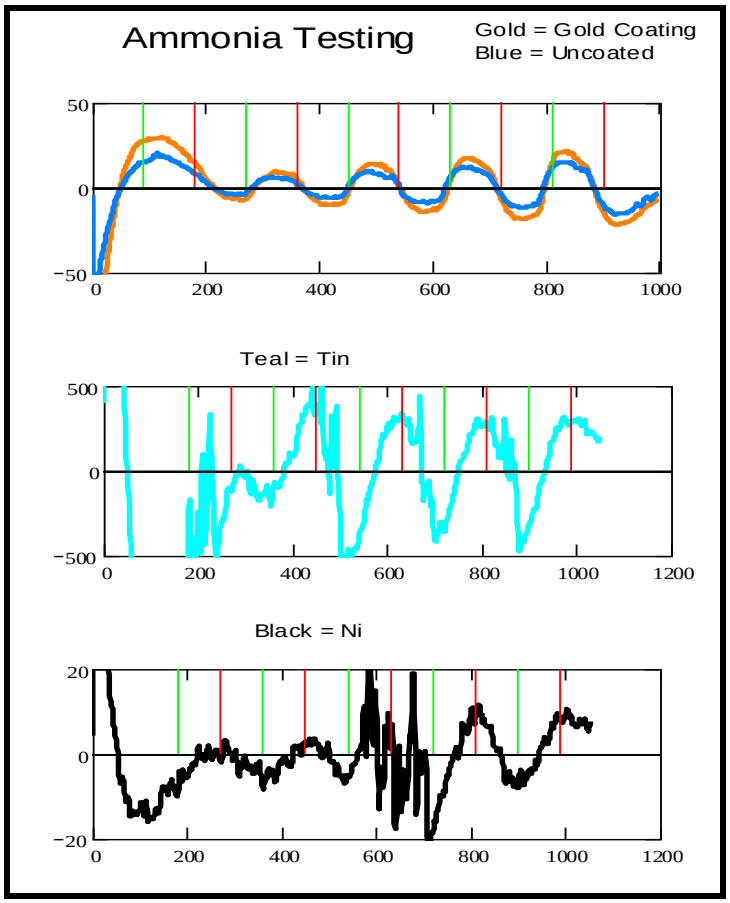

Figure 2.29 NH_3 test done with portable device with 4 different sensors.

2.5 References

[1] F.M.Smits, The Bell Technical Journal 37, 711-718 (1958).

[2] Valdes, L. G., Proc. I.R.E., 42, pp. 420-427 (1954).

[3] Fundamentals of Microfabrication: The Science of Miniaturization, Second Edition, Marc J Madou, CRC Press; 2 edition, 2002, pg 206.

[4] http://grover.mirc.gatech.edu/processing/processmenu.php?m=p&l=3&s=8 (Accessed March 4, 2011)

[5] The Science and Engineering of Microelectronic Fabrication, Stephen A. Campbell, Oxford University Press, 2nd edition, USA, 2001,

[6] A. Uhlir, “Electrolytic Shaping of Germanium and Silicon” Bell Syst. Tech. J., 35, 333 (1956).

[7] L.T. Canham, MRS Bull., vol. 18, p22 (1993).

[8] Seals, L., et al., “Rapid, reversible, sensitive porous silicon gas sensor”, Journal of Applied Physics, 91(4): p. 2519-2523 (2002).

[9] Lewis, S., The creation of a Viable Porous Silicon Gas Sensor, 2006, Georgia Institute of Technology: Atlanta.

[10] Serdar Ozdemir, James L. Gole, “The Potential of Porous Silicon Gas Sensors”, Current Opinion in Solid State and Materials Science, 11, 92-100 (2007).

[11] J.L. Gole, J.A. Corno, S. Ozdemir, S. Prokes, H-C. Shin,”Active microfiltered sensor interfaces, photocatalytic reactors, and microbatteries using combined micro/nanoporous interfaces” Phys. Status Solidi C, 6, No. 7, 1773-1776 (2009).

[12] JL. Gole, S. Lewis, S. Lee “Nanostructures and porous silicon: activity at interfaces in sensors and photocatalytic reactors”, Physica Status Solidi A, Vol 204, Issue 5 , 1417-1422 (2007).

[13] J. Campbell, JA. Corno, N. Larsen, JL Gole, “Development of porous-silicon-based active microfilters” J. Electrochem. Soc., 155 (2), D128-D132 (2008).

[14] J. Corno, “Structural and Chemical Moidification of Porous Silicon for Energy Storage and Conversion” 2008, Georgia Institute of Technology, Atlanta, GA.

[15] H. Foll, M. Christophersen, J. Carstensen, G. Hasse “Formation and application of porous silicon”, Materials Science and Engineering R 280, 1–49 (2002).

[16] K. W. Kolasinski, “Charge Transfer and Nanostructure Formation During Electroless Etching of Silicon” J. Phys. Chem. C. 114, 22098-22105 (2010).

[17] Kui-Qing Peng, Xin Wang, and Shuit-Tong Lee “Gas sensing properties of single crystalline porous silicon nanowires” Appl. Phys. Lett. 95, 243112 (2009).

[18] C. Chartier, S. Bastide, C. Levy-Clement , “Metal-assisted chemical etching of silicon in HF–H2O2”, Electrochimica Acta, 53, 5509–5516 (2008).

[19] http://en.wikipedia.org/wiki/Chemical-mechanical_planarization (Accessed on March 1, 2011).

[20] V. Lehmann and U. Gosele “Porous silicon formation: A quantum wire effect”, Appl. Phys. Lett., Vol. 58, No. 8 (1991).

[21] Materials Science and Engineering, ” On the morphology and the electrochemical formation mechanism of mesoporous silicon”, B69–70, 11–22 (2000).

[22] Kurt W. Kolasinski, Surface Science: Foundations of Catalysis and Nanoscience, 2nd Edition, Wiley,Great Britain, 2008, p.377.

[23] E. A. Ponomarev, C. Lévy-Clément “Macropore Formation on p-Type Si in Fluoride Containing Organic Electrolytes” Electrochemical and Solid State Letters, 1 (1), 42-45 (1998).

[24] E.K. Propst and P.A. Kohl, J. Electrochem. Soc. 141,1006 (1994).

[25] R.L. Smith, S.D. Collins, J. Appl. Phys. 71, R1 (1992).

[26] James L. Gole, Erling Veje, R. G. Egeberg,A. Ferreira da Silva, I. Pepe, David A. Dixon. "Optical Analysis of the Light Emission from Porous Silicon: A Hybrid Polyatom Surface-Coupled Fluorophor" J. Phys. Chem. B, Vol. 110, No. 5 (2006).

[27] Private communication with Prof Levy-Clement.

[28] Ju-Young Lee, Hyuckmo Lee and Jae-Ho Lee ,“Electrochemical Etching of p-Si for the Double Layer Porous Silicon Fabrication”, Abstract 1663, 218th ECS Meeting, Las Vegas (2010).

[29] http://www.mgchemicals.com/products/841.html (Last Accessed on March 1, 2011).

[30] S. Lewis, J. DeBoer, J.L. Gole and P. Hesketh, Sensitive, selective, and analytical improvements to a porous silicon gas sensor, Sens. Actuators B 110 (2005), pp. 54–65.

[31] J.L. Gole, S. Lewis and S. Lee, “Nanostructures and porous silicon: activity at interfaces in sensors and photocatalytic reactors”, Phys. Stat. Sol. A 204 (2007), pp. 1417–1422.

[32] S. Ozdemir, J.L. Gole, ”A Phosphine Detection Matrix Using Porous Silicon Gas Sensors”, Sensors and Actuators B, 151, 274-280 (2010).

[33] D. Brumhead, L.T. Canham, D.M. Seekings, P.J. Tufton. “Gravimetric analysis of pore nucleation and pore propogation in anodizaed silicon”, Electrochimica Acta, vol. 38, no2/3, pg 191-197 (1993).

[34] http://en.wikipedia.org/wiki/Ellipsometry (Last Accessed on March 6, 2011)

[35] L.T Canham “Pore type, shape, size, volume and surface area in porous silicon”, pg 81. in Porous Silicon, Edt. L.T. Canham, INSPEC, England, 1997.

[36] R. Giuly, J.A. Corno, J.L.Gole “A simple method for generating nano-pillars and uniformly separated nano-needle arrays on silicon” Materials Letters, vol:62, Issue:17-18, pg. 2704-2706 (2008).

[37] A. Shalek, J. T. Robinson, E. S. Karp, J. S. Lee, D-R. Ahn, M-H. Yoon, A. Sutton, M. Jorgolli, R. S. Gertner, T. S. Gujral, G. MacBeath, E. G. Yang, H. Park, “Vertical silicon nanowires as a universal platform for delivering biomolecules into living cells,” Proc. Natl. Acad. Sci. USA 107, 1870-1875 (2010) .

[38] Power M, Hosticka B, Black E, Daitch C, Norris P, "Aerogels as biosensors: viral particle detection by bacteria immobilized on large pore aerogel" Journal of non-crystalinne solids, vol 285, 1-3, pg 303-308 (2001).

[39] ‘Local formation and patterning of porous silicon’ A.G Nassiopoulos in “Properties of porous silicon” in Porous Silicon, Edt. L.T. Canham, INSPEC, England, 1997. pg 77.

[40] http://grover.mirc.gatech.edu/equipment/ (Last Accessed on March 6,2011).

[41] https://www.stencilsunlimited.com/ (Last Accessed on March 6, 2011).

CHAPTER 3

SURFACE FUNCTIONALIZATION

Untreated porous silicon (PS) sensors are responsive to various gases. One way to increase the sensitivity and selectivity of this sensor configuration is achieved by functionalizing the surface with nanoparticle depositions. Tin oxide (SnO_x), nickel oxide (Ni_xO), copper oxide (Cu_xO), gold (Au), zirconia (ZrO_x), and alumina (Al_2O_3) nanoparticles are prepared by solution chemistry and vapor liquid solid (VLS) processes and applied to the sensor surface to provide a change in sensitivity and improved selectivity. A schematic of these nanoparticle depositions onto the PS surface is depicted in Figure 3.1.

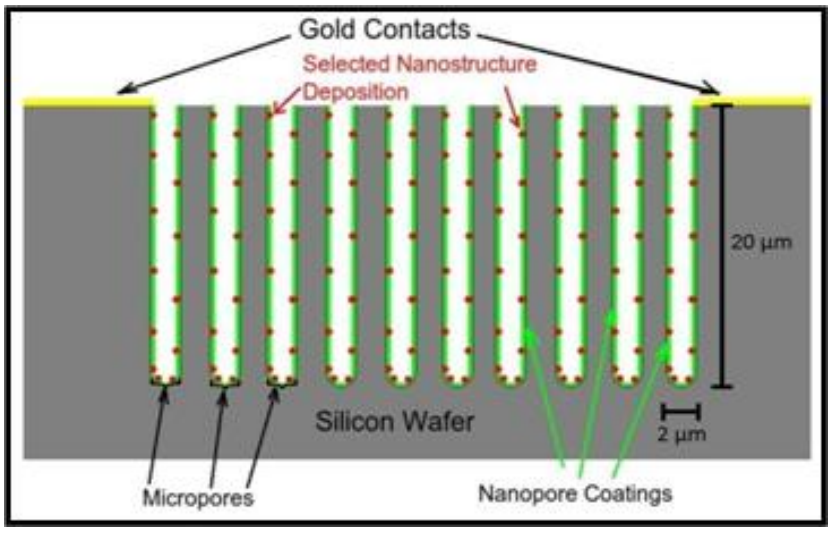

Figure 3.1 Schematic representation of the PS hybrid sensor structure and selected nanostructure depositions.

In order to obtain a tin oxide nanostructured deposition on the PS interface, an electroless tin coating is formed from 0.33 M tin chloride, 1.92 M sodium hydroxide, and 0.66 M sodium citrate mixed at 70 °C [2]. The solution is stirred until it cools to room temperature. PS is immersed into the solution for 25 s in order to obtain the desired SnO_2 coating. After immersion, it is placed in DI H_2O and MeOH for consecutive 30 s periods.

An electroless copper solution is prepared from $CuSO_4 \cdot 5H_2O$ (0.76 g), sodium tartrate (4.92 g), formaldehyde (2 mL 0.27 M formaldehyde), and NaOH (0.8 g) diluted to 200 mL in deionized (DI) water [3]. Porous Si sensors are again dipped into the electroless solution for 30 s and then again placed in DI H_2O and MeOH for about 30 s. The electroless nickel solution [4] contains nickel chloride (20 g/L) as the nickel source, sodium hydroxide (40 g/L) as a complexing agent, sodium borohydride (0.67 g/L) as a reducing agent, and ethylene diamine (44 g/L) as the stabilizer. PS is exposed to the electroless Ni solution for 25 s, then placed in DI H_2O and MeOH, each for about 30 s. For the electroless gold coating [5], we have used a commercially available electroless gold metallization solution (Transene) and treated the sensor for 30 s. Afterwards the sensor was cleaned with DI water and MeOH. For each nanostructured deposit, instead of forming a film on the porous surface, islands of nanostructured metal oxides are formed with an emphasis on short duration exposures to the electroless solutions. Alumina nanostructures were deposited directly to the PS interface. The Al_2O_3 nanocoating was prepared [6] using Boehmite (Wako Chamicals). Here, 0.1 g of Boehmite ($AlO(OH) \cdot nH_2O$) was mixed with 100 ml of DI water and the pH adjusted to 4.5 by adding a few drops of HNO_3. The solution was stirred at 40 °C for about 10 days as, each day, the pH was additionally adjusted with HNO_3. After this stabilization, the sensors were coated for 1 min by immersing them into the prepared solution. The Boehmite coated sensor was then heated at 400 °C in an 100 sccm O_2 flow at 300 Torr for 4 h to convert the Boehmite to γ-Al_2O_3.

We have examined the PS interface with a scanning electron microscope (by LEO 1520 SEM and Hitachi SEM 3500 H [7]) after the electroless depositions were used to deposit metal-based nanostructures to the PS surfaces. SEM analysis shows that the nanopore radius varies from 10's of nanometers to a few 100 nm (Fig. 2.13). Any surface roughening and deformation due to the presence of hydroxide is not easy to observe after

the short duration of the electroless solution treatments (≤30 s) used in this study. Further, we are not able to establish whether or not a gestation period is necessary for any hydroxide etch in these systems. The nanoparticles deposited on the surface are clearly observed via SEM analysis (Fig. 3.2) [8]. In Figure 3.3 (a), Ni_xO and Cu_xO solutions are depicted. The particles in these solutions can agglomerate as the solutions grow older. Stirring the solutions continuously with low stirring speeds may help prevent agglomeration. In Figure 3.3, an SEM image of the spherical Ni_xO agglomerates deposited onto a clean Si surface is shown. The Ni_xO clusters have an average diameter close to 300 nm. Smaller nanoparticles around the agglomerate may also be observed clearly in the image. Figure 3.3 (c) shows copper agglomerates of larger size (few μm). A clear Cu peak in the EDS (Noran EDS System on Hitachi 3500 H [7]) measurement of the surface is depicted in Figure 3.3 (d). We have observed that optimum selectivity is achieved with nanoparticle depositions onto the porous network, forming nanoparticle islands. These depositions must be sufficiently dilute to avoid cross talk between the nanoparticle islands. Thin film depositions and large agglomerates of nanoparticles do not improve the sensor response. In most cases, it is extremely difficult to obtain a good EDS spectrum for the nanoparticle depositions and XPS measurements are performed as an alternative.

An alternate method employed for nanoparticle formation is the VLS process [9]. A Lindberg Blue M furnace system (max 1700 ^{0}C) with one temperature zone is used for the process. An Al_2O_3 tube system is placed inside the furnace as the temperature of the central zone is controlled with a thermocouple. One end of the tube is arranged to allow for ports used to obtain an O_2 and Ar entrainment flow inside the furnace region. O_2 is carried to the central region through 1/8 inch stainless steel tubing with a nozzle on one end. The gas flow for each gas is controlled with MKS mass flow controllers. A water cooled condensation plate, is connected to the other end of the alumina tube. This end is

also connected to an MKS Baratron and a mechanical vacuum pump (Welch 1397) to control the pressure inside the alumina centered tube furnace. To form ZrO_x nanoparticles, high purity $ZrCl_4$ (Alfa Aesar), used as the main constituent, is placed in a crucible in the central zone. The flow of the gases (5-15 sccm for O_2, 10-30 sccm for Ar), temperature (250-500 ^{0}C) and total pressure (100-300 Torr) of the system are varied to produce various ZrO_x structures. A typical sample is produced with 8 sccm O_2 and 20 sccm Ar flow at a 300 Torr system pressure where the $ZrCl_4$ is heated at 300 ^{0}C for 12 hrs. A TEM image of the sample collected from the water cooled zone under these conditions is depicted in Figure 3.4 (Please see Ref-7 for earlier, detailed TEM analysis on ZrO_x spheres). The particle size varies from 50-100 nm. A 0.05 gr sample of the produced ZrO_x particles is stirred with 20 ml of MeOH for several hours after which a clean wafer was dipped into this solution for 5 minutes. The surface was analyzed with SEM and is depicted in Figure 3.4 (b). We can clearly see the cubical and pyramidal agglomeration of ZrO_x particles.

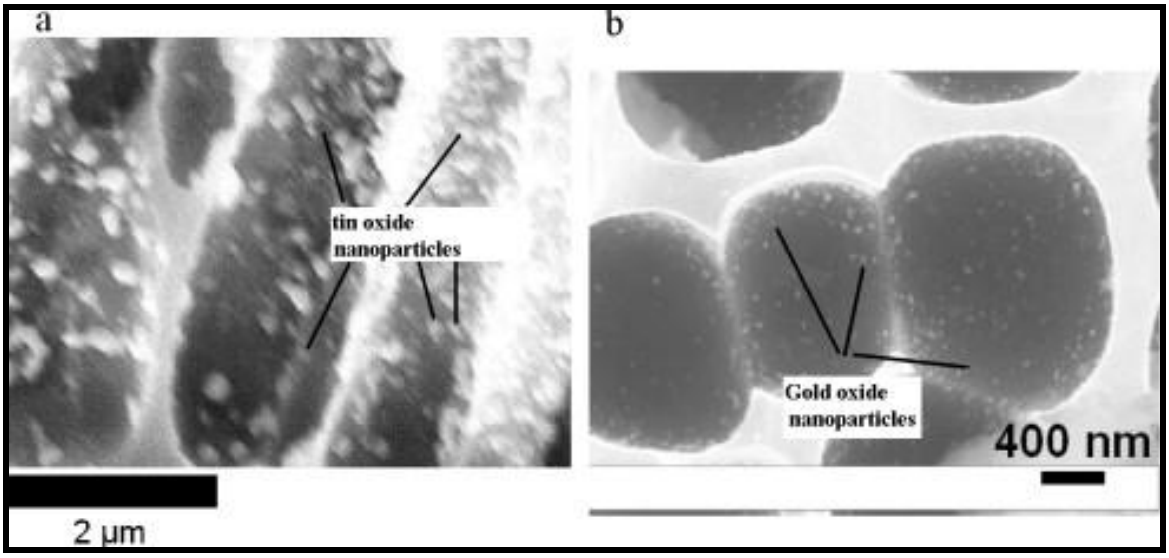

Figure 3.2. (a) Tin oxide nanoparticles deposited onto PS. (b) Gold clustered oxide nanoparticles deposited onto PS.

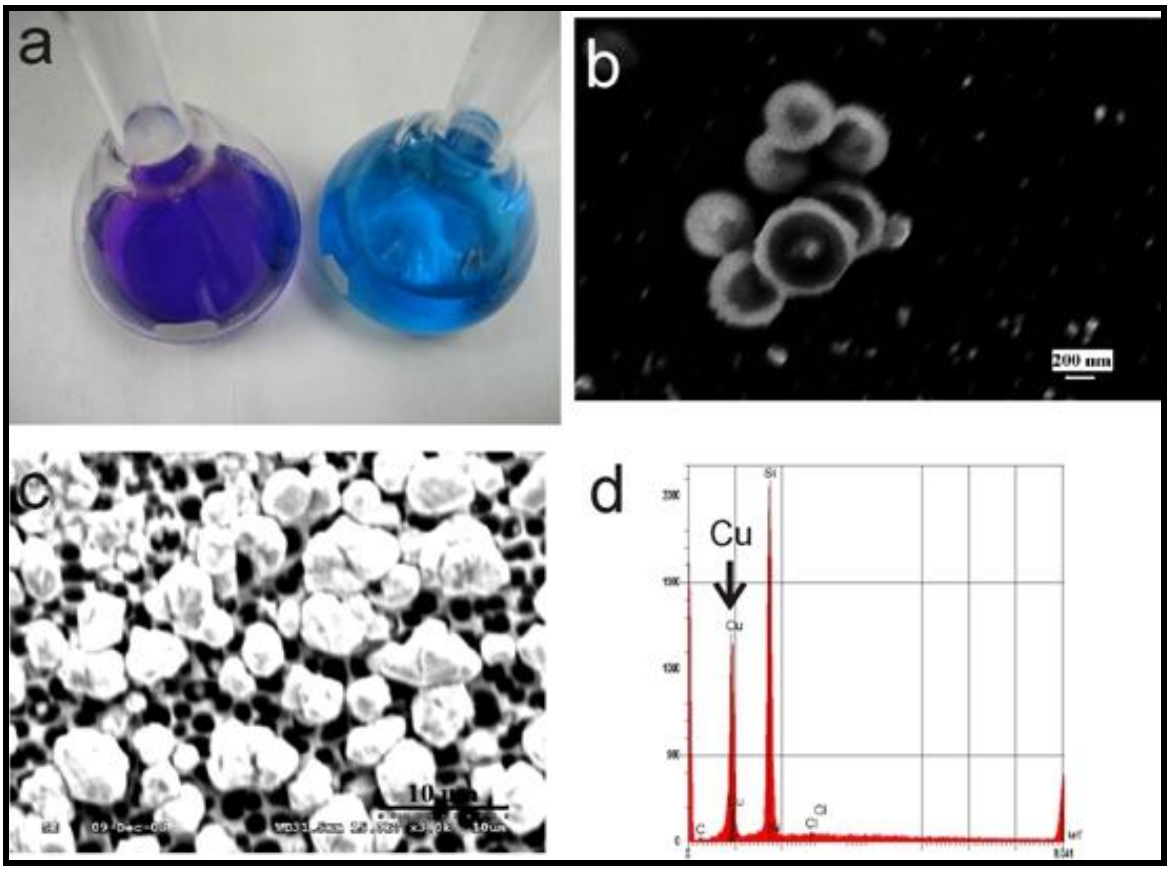

Figure 3.3 a) Nickel solution (left) and copper solution (right). b) Ni_xO spherical agglomerates and nanoparticles are depicted. c) Cu_xO agglomerates deposited onto PS. d) EDS measurement of the Cu_xO deposited surface. When nanoparticles are deposited no clear EDS signal is observed. However, we observe a change of sensor response.

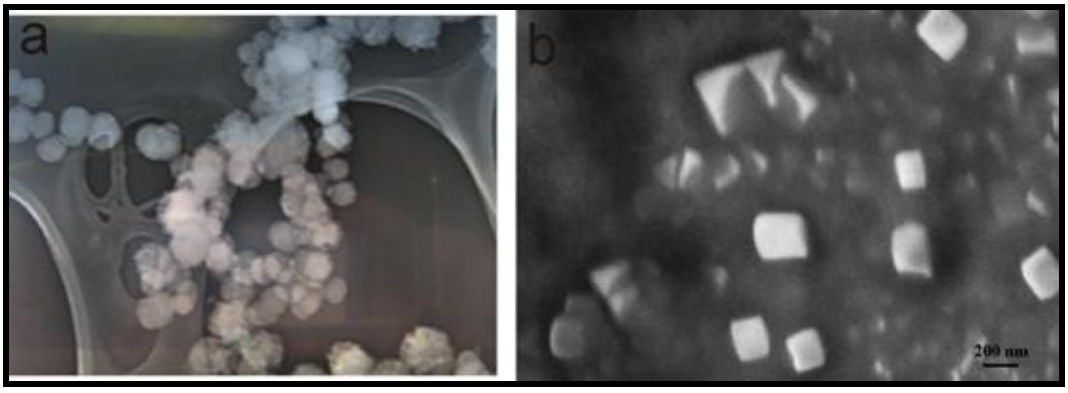

Figure 3.4 a) A TEM image of ZrO_x nanospheres. b) A 0.05 gr sample of the produced ZrO_x particles is stirred with 20 ml of MeOH for several hours as a clean wafer piece is dipped into this solution for 5 minutes. An SEM image of the surface is depicted. Cubical and pyramidal agglomerate formation is observed.

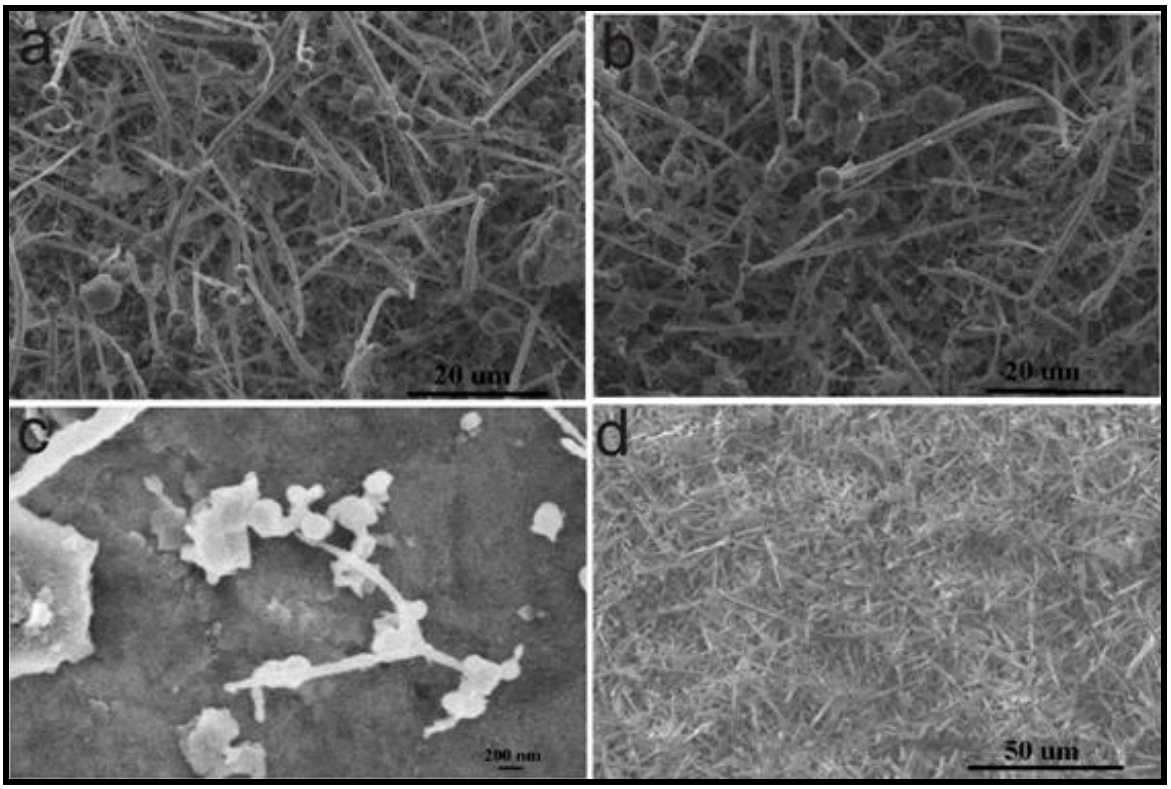

Figure 3.5 SEM images of SiO_x wires produced by the VLS process. (a)-(b) Nanowires are deposited with TiO_2 and $TiO_{2-x}N_x$ by immersion. A non uniform TiO_2 deposition on wires is observed. c) A closer look at the non uniform deposition. Some particles are crashed during immersion and TiO_2 solution stirring. d) SEM image of a more uniform deposition at a larger scale is depicted.

A similar system is used to produce silica nanospheres and nanowires. The entrainment gas in this case is still Ar (100 sccm), but no O_2 is needed for the process. A mixture of high purity Si:SiO2 (1:1) is heated at typical operating temperatures which range from 1400 to 1550 ^{0}C for 12 hrs and an operating pressure of 200 Torr. Detailed information about earlier work in Prof Gole's group on Si nanowires may be found in Ref-10. The collection of SiO_x nanowires on the cold finger changes color from white (1400 ^{0}C) to brown (1550 ^{0}C) as the oxidation state of the wires change. The brown particles collected correspond primarily to nanowires and are very hydrophobic. The SEM images of the observed wires are shown in Figure 3.5. The nucleation of the wires begins from spherical agglomerates which have diameters of about 1-2 μm and the

nanowires can be a few 100 μm long. We have done several experiments with nanowires and tried to deposit TiO_2 nanoparticles onto their surface. SEM images of the produced materials are shown in Figure 3.5. Both TiO_2 and $TiO2_{-x}N_x$ nanoparticles were produced using sol gel methods [11,12]. These particles are diluted at various concentrations in MeOH and the nanowires produced by the VLS process are coated by immersion. Figure 3.4 (d) shows a reasonably uniform coating at large scale.

3.1 XPS Analysis

XPS measurements on nanostructure deposited sensors are presented in Fig. 3.6 and Fig. 3.7. All of the XPS measurements are done using a Thermo K-Alpha XPS system. The X-ray source is Al Kα and the spot size is 400 μm^2. Each scan is repeated 10 times. For charge compensation, an electron flood gun is used. The experiments are conducted at pressures below 10^{-8} mbar. Fig. 3.6(a) depicts the XPS spectrum of a dominantly SnO_x nanostructure deposited PS surface. SnO (Sn^{2+}) has peaks in the range of 485.6–487.0 eV, SnO_2 (Sn^{4+}) has peaks in the range of 486.1–487.1 eV. There are also Sn^{2+} and Sn^{4+} peaks located in the range 487.0–488.0 eV [13]. These data are therefore consistent with the deposition to and oxidation of tin nanoparticles which are deposited and rapidly oxidized on the PS surface. Fig. 3.6(b) depicts the XPS spectrum for Ni nanostructure deposition. Nickel has an oxidation peak ($2p_{1/2}$) located ~ 871.8 eV for NiO (Ni^{2+}) and has peaks ($2p_{3/2}$) in the range of 853.6–857.2 eV. Ni_2O_3 (Ni^{3+}) shows peaks ($2p_{3/2}$) from 855.8–856.5 eV [13]. Thus the observed XPS spectrum is consistent with the deposition and oxidation of nickel nanoparticles. Fig. 3.6(c) depicts the XPS spectrum for a dominantly Cu_xO nanoparticle deposition. CuO (Cu^{2+}) has peaks ($2p_{1/2}$) in the range 952.5–952.7 eV and has peaks ($2p_{3/2}$) in the range 933.3–934.3 eV. Cu_2O (Cu^{1+}) has peaks in the range 932.0–932.8 eV [13]. Thus, this spectrum demonstrates the deposition to and oxidation of copper nanoparticles at the PS surface. The observed Au

$4f_{5/2}$ and $4f_{7/2}$ doublets and curve fit to the experimental data for the XPS spectrum obtained for gold deposition are depicted in Fig. 3.6(d) [13].

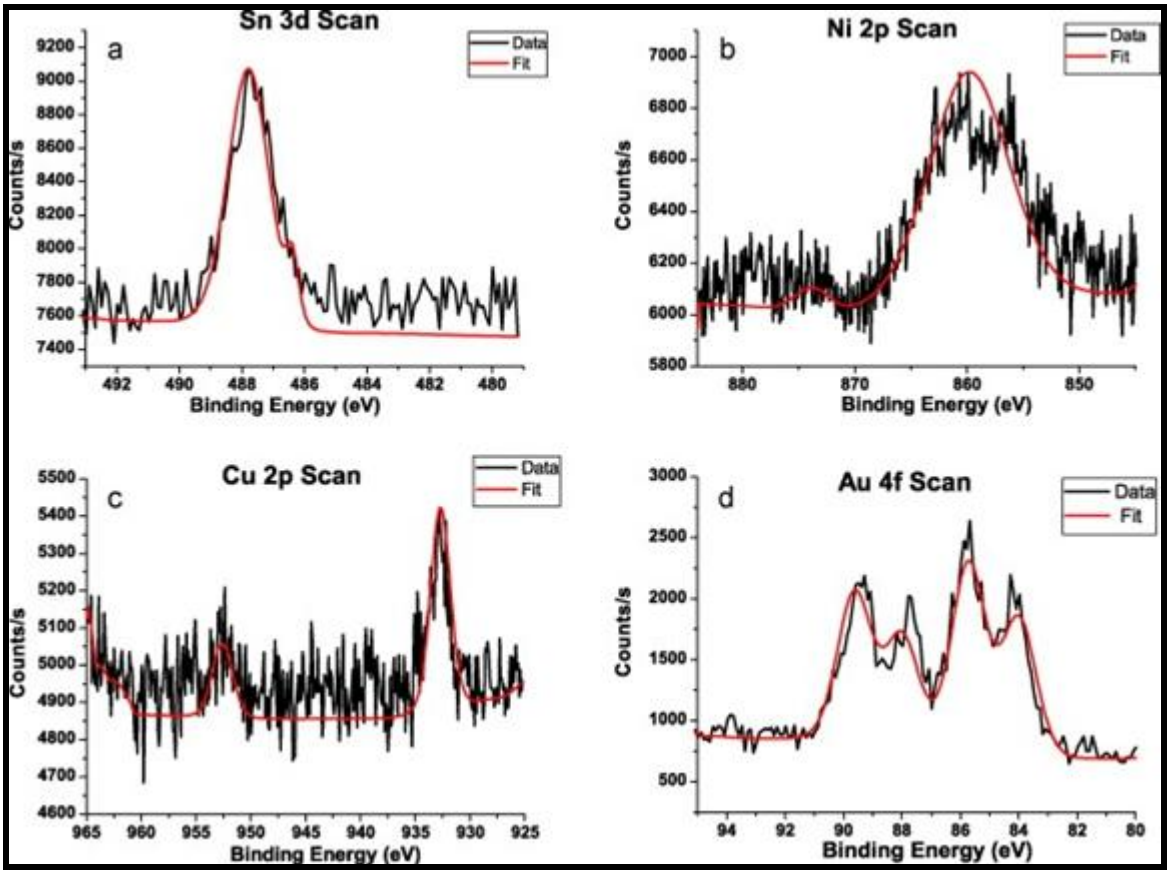

Figure 3.6. XPS spectra of metal-based nanostructure deposited PS sensors and fitting curves (in red) to the spectra. (a) XPS spectrum of a dominantly SnO_x deposited sensor. SnO (Sn^{2+}) has peaks in the range of 485.6–487.0 eV, SnO_2 (Sn^{4+}) has peaks in the range of 486.1–487.1 eV. (b) XPS spectrum of a dominantly Ni_xO deposited sensor. Nickel has an oxidation peak ($2p_{1/2}$) located ~ 871.8 eV for NiO (Ni^{2+}) and has peaks ($2p_{3/2}$) in the range of 853.6–857.2 eV. Ni_2O_3 (Ni^{3+}) shows peaks from 855.8 eV to 856.5 eV. (c) XPS spectrum for a dominantly Cu_xO deposited PS surface. CuO (Cu^{2+}) has peaks ($2p_{1/2}$) in the range of 952.5–952.7 eV and has peaks ($2p_{3/2}$) in the range of 933.3–934.3 eV. Cu_2O (Cu^{1+}) has peaks in the range of 932.0–932.8 eV. (d) XPS spectrum of Au $4f_{5/2}$ and Au $4f_{7/2}$ doublets [13] which demonstrate minimal oxidation.

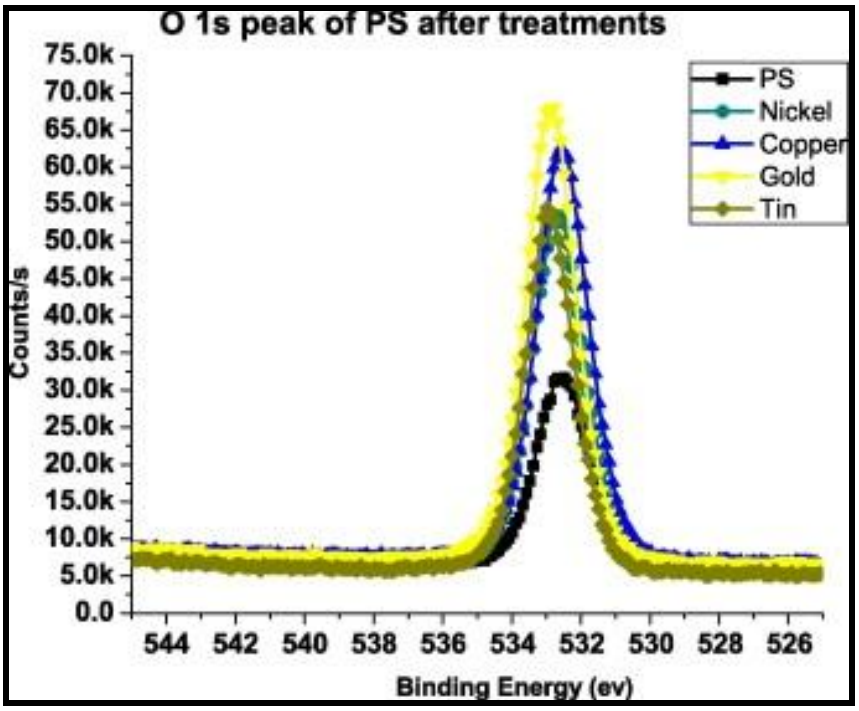

Fig. 3.7. O 1s spectra of untreated and nanoparticle treated PS surface.

The corresponding O 1s spectra associated with the PS surface and the Sn 3d, Ni 2p, Cu 2p, and Au 4f XPS data in Fig. 3.6(a)–(d) are depicted in Fig. 3.7. There are several important characteristics of these O 1s spectra. The peaks are quite symmetric; in other words, we observe no clear shoulder features at the higher (or lower) binding energy side of the O 1s features associated with copper, nickel, or tin which might be correlated with the significant presence of OH groups [14] and [15] (and water). Further, the NIST data compilation [14] suggests that surface-layer OH binding energies should well exceed those of the oxides. The most recent data for the OH binding energy peaks associated with H_2O suggest values of 534.8 [16] and 538 eV [17]. Further, in a very interesting recent article on hydroxylated nickel oxide (1 1 1), Ciston et al. [18] note a significant shoulder in their O 1s XPS spectrum, to higher binding energy, which they associate with OH. In correlation with the data in Fig. 3.6(a)–(c), it is suggested that the XPS spectra are to be attributed to oxidation dominated by the formation of metal oxide nanoparticles on the PS surface. It is further to be noted that the O 1s spectra in Fig. 3.7

are shifted in the order gold ≈ tin > nickel > copper. This suggests that the spectral shifts cannot be correlated with the degree of oxidation but rather with the positioning and accessibility of the interactive nanostructured oxides on the walls of the nanopore covered microporous array (Fig. 3.1) associated with PS [19]. The O 1s XPS spectrum of the native silica coating associated with PS is notably weaker and shifted to somewhat lower binding energy. This, we suggest, should be attributed to the more accessible nature of the metal oxides and gold clustered oxide deposits on the PS surface [8] and [19].

XPS measurements of both treated and untreated PS surfaces show virtually identical C peaks due to CH_3OH treatment at various steps of the sensor fabrication and exposure to reproducible concentrations of hydrocarbons in the hood environment in which the sensors are tested, suggesting that the changes in sensitivity observed in the present study, which we outline below, cannot be associated with a variable sensitivity of these hydrocarbons to the analytes considered. The XPS spectra are consistent with a pronounced oxidation of the Ni, Cu, and Sn nanoparticle depositions. In contrast the XPS spectra obtained for Au are consistent with a much milder oxidation and the formation of the gold clustered oxides, Au_xO.

3.2 Summary

Nanoparticles of various types, sizes and shapes are produced via solution chemistry and VLS techniques. These particles are analyzed with SEM, EDS and XPS. These particles are deposited onto PS for selectivity improvements of the sensors and their affect will be discussed in the following chapters

3.3 References

[1] ”A Phosphine Detection Matrix Using Porous Silicon Gas Sensors” S. Ozdemir, J.L. Gole, Sensors and Actuators B, 151, 274-280 (2010).

[2] Modification of procedures in H.M. Van Noort, B.C.M. Meenderink, A.J. Molenaar, In situ ^{119}Sn conversion electron Mössbauer study of the surface of tin layers as deposited by an electroless process, J. Electrochem. Soc., 133, 263–265 (1986) by L. Seals and J.L. Gole.

[3] E.K. Yung, L.T. Romankiw and R.C. Alkire, "Plating of copper into through-holes and vias", J. Electrochem. Soc. 136, pp. 206–215 (1989).

[4] L. Seals, private communication.

[5] In: M. Schlesinger and M. Paunovic, Editors, Modern Electroplating, 4th Edt., Wiley, New York (2000).

[6] D.S. Horn and G.L. Messing, "Alumina monolith formation by flocculation of boehmite sols", J. Am. Ceram. Soc., 72, pp. 1719–1721 (1989).

[7] http://grover.mirc.gatech.edu/equipment/ (Last Accessed on March 7,2011)

[8] J.L. Gole, S. Lewis and S. Lee, "Nanostructures and porous silicon: activity at interfaces in sensors and photocatalytic reactors", Phys. Stat. Sol. A, 204, 1417–1422 (2007).

[9] James L. Gole, Sharka M. Prokes, John D. Stout, Orest J. Glembocki, and Rusen Yang, "Unique Properties of Selectively Formed Zirconia Nanostructures", Adv. Mater. 18, 664–667 (2006).

[10] J. L. Gole and J. D. Stout, W. L. Rauch, Z. L. Wang, "Direct synthesis of silicon nanowires, silica nanospheres, and wire-like nanosphere agglomerates", Appl. Phys. Lett. Vol 76,17, 2346-2346 (2000).

[11] C. Burda, Y.Lou,X. Chen, A. C. S. Samia, J. Stout, J. L. Gole, "Ehanced Nitrogen Doping in TiO_2 Nanoparticles" Nano Lett., Vol. 3, No. 8. (2003).

[12] J. L. Gole, J.D. Stout, C. Burda, Y. Lou, X Chen, "Highly Efficient Formation of Visible Light Tunable $TiO_{2-x}N_x$ Photocatalysts and Their Transformation at the Nanoscale" J. Phys. Chem. B, 108, 1230-1240 (2004).

[13] NIST X-ray Photoelectron Spectroscopy Database, Version 3.5 (National Institute of Standards and Technology, Gaithersburg, 2003) http://srdata.nist.gov/xps/. (Last Accessed on March 7, 2011).

[14] NIST X-ray Photoelectron Spectroscopy Database, Version 3.5 (National Institute of Standards and Technology, Gaithersburg, 2003) http://srdata.nist.gov/xps/. (Last Accessed on March 8th, 2011).

[15] In: J.L.G. Fierro, Editor, *Metal Oxides: Chemistry and Applications*, CRC Taylor & Francis, Boca Raton, FL (2006).

[16] M. Lundholm, H. Siegbahn, S. Holmberg and M. Arbman, J. Electron Spectrosc. Relat. Phenom., 40, p. 163 (1986).

[17] J. Russat, Surf. Interface Anal. 11, p. 414 (1988).

[18] J. Ciston, A. Subramanian, D.M. Kienzle and L.D. Marks, Surf. Sci., 604, pp. 155–164 (2010).

[19] J.L. Gole and S. Ozdemir, "Nanostructure directed physisorption vs. chemisorption at semiconductor interfaces: the inverse of the hard-soft acid–base (HSAB) concept", ChemPhysChem 11, pp. 2573–2581 (2010).

CHAPTER 4

RESULTS & DISCUSSIONS

Conductometric porous silicon (PS) sensors have been evaluated with various gases. A typical sensor response is depicted in Figure 4.1. A high quality sensor gives no response when there are no target species in the environment. This nonresponsive state is referred to as the *base line*. Gas sensors might be responsive to various gases at certain levels. We can introduce *selectivity* as the ability to distinguish responses for different target gases. A high quality sensor should provide a maximum response to a test gas and a minimum response to other gases in its environment. As soon as a stimulant is introduced at t_1, the sensor gives a response (solid line in Figure 4.1). Sensors must operate at a dynamic range where the shape of a response curve depends on the concentration of the target species. For example, some of the commercial conductometric gas sensors [1] explain the concentration dependence as

$$R = R_0 + ac^{-b} \qquad \text{(Equation 4.1)}$$

where "R" is the resistance, "R_0" is the base resistance, "c" is the test gas concentration. "a" and "b" are experimental parameters. The response of a sensor is always determined with respect to the initial unresponsive state. Response reaches a steady state (or a saturated state) after a long enough exposure. *Response time* is the duration for a sensor to reach 90 % of the steady state response and *recovery time* is the duration it takes for a sensor's response to return to its base line. The s*ensitivity* of the sensor depends on the slope of the response curve.

Previous experiments performed with PS gas sensors have been based on impedance analysis. All of the data presented in this chapter is based on resistance measurements. Although an impedance analysis can improve response time, we have observed that with an optimized PS creation process, we can obtain significantly higher sensitivity with a simpler measurement technique. Gas sensors are flushed with UHP N_2

before each test for extended periods of time (1/2 hr to 1 hr) to maintain a stable base resistance before any target gas exposure.

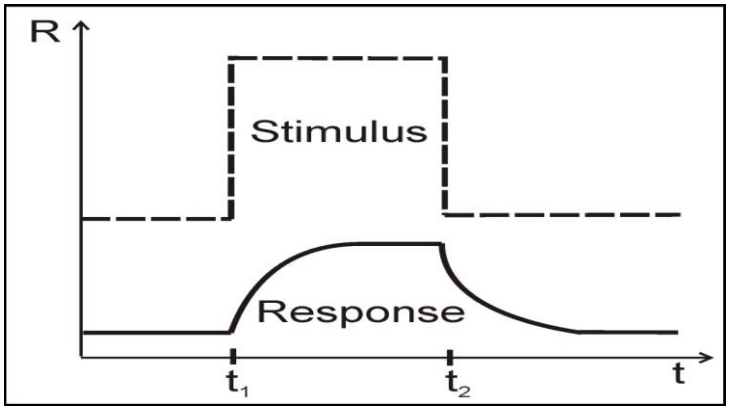

Figure 4.1 A schematic of a typical, "saturated" gas sensor response is depicted (solid line) under the influence of a stimulus (dashed line). Here, the y-axis is the response (e.g. resistance) and x-axis is time. The sensor gives a saturated response as soon as the test gas begins operating at t_1 and goes back to its initial no response state as the test gas is cut off at t_2.

Previous studies [2,3] had suggested that the proper combination of nanostructure coating techniques on the PS hybrid structure can be used to produce devices of varying sensitivity and selectivity and that a matrix of array responses can be generated to analyze gas mixtures. For example, an array of an untreated PS sensor, SnO_2, and gold clustered oxide nanodeposited sensors could be used to sensitively test for the presence and relative concentrations of ammonia and nitric oxide [2] and provides a basis for developing a very sensitive room temperature nitric oxide detector that could be installed in a simple sensor system for asthmatics [2]. The outlined nanodeposits are formed using electroless metal solutions [4,5]. There are several other complimentary methods that might be used to produce gas selective nanocoatings on the nano/micropores of PS. These include short-term electron beam deposition, atomic layer depositions, and direct nanoparticle diffusion into the PS micropores. An extension to the detection of several additional gases including PH_3 [6] , acetone [7], and benzene [8] (in addition to NH_3 [2,9] and HCl [2,9]) can be made possible using specially designed aluminum oxide (atomic layer deposition or e-beam) or aluminosilicate nanostructured surfaces [6], nickel (electroless) or

zirconium oxide based (nanostructured ZrO_2 nanoshells [10] deposited into the micropores of PS) nanostructured surfaces [10], and nitrided titanium dioxide [8] ($TiO_{2-x}N_x$ [9,11]) nanostructured coatings. It is possible to expand the list of gases with the development of a more general selective coating technology based on the extrapolation of the concepts of hard and soft acids and bases.

In this chapter, an overview of the gas testing experiments performed with NH_3, PH_3 and NO_x will be discussed.

4.1 Ammonia (NH_3) Testing

Ammonia is a colorless gas with a characteristic pungent odor. It has been used mainly in producing fertilizers, explosives and cleaners. 1000 ppm NH_3 (Matheson) is diluted in N_2 for all of the testing experiments. A typical NH_3 response is depicted in Figure 4.2. In this figure, the surface of an untreated PS sensor is exposed to 1,2,3,4,5 ppm of NH_3 every 300 s. The measured resistance response is not saturated and depends on the gas concentration linearly.

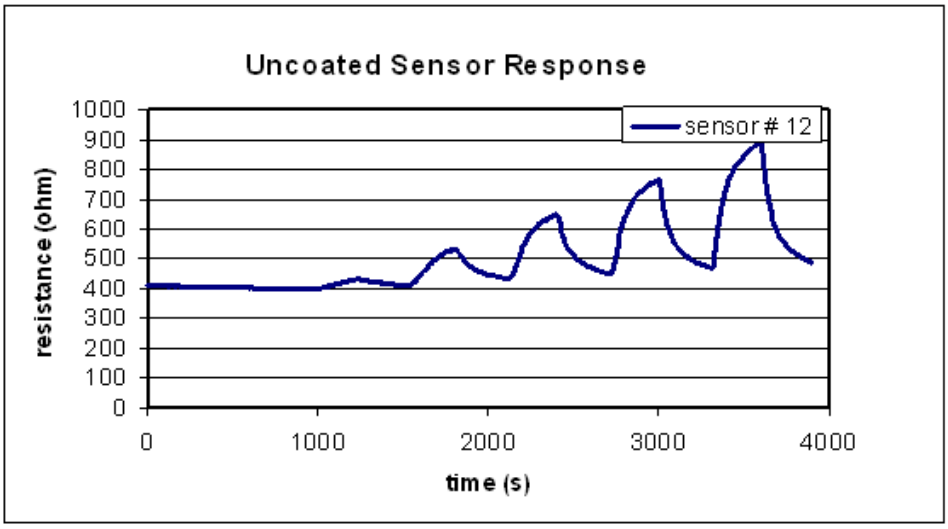

Figure 4.2. An untreated PS surface is exposed to NH_3. The PS surface is purged with N_2 for an initial period of 1200 s. After gas stabilization is achieved, 1,2,3,4,5 ppm of NH_3 are pulsed onto the sensor every 300 s (300 s ON, 300 s OFF).

An important characteristic of any high quality sensor is the reproducibility of the sensor response to exposure to the same analyte concentration. The reproducibility of a PS sensor under 5 ppm NH_3 exposure is depicted in Figure 4.3. Although there is a drift in the overall exposure due to the many cycles of NH_3 pulsing, the response is about 70 Ohms for each 5 ppm pulse. We have observed that the recovery time for PS sensors is greater than response which will cause the drift of the base resistance as depicted in Figure 4.3

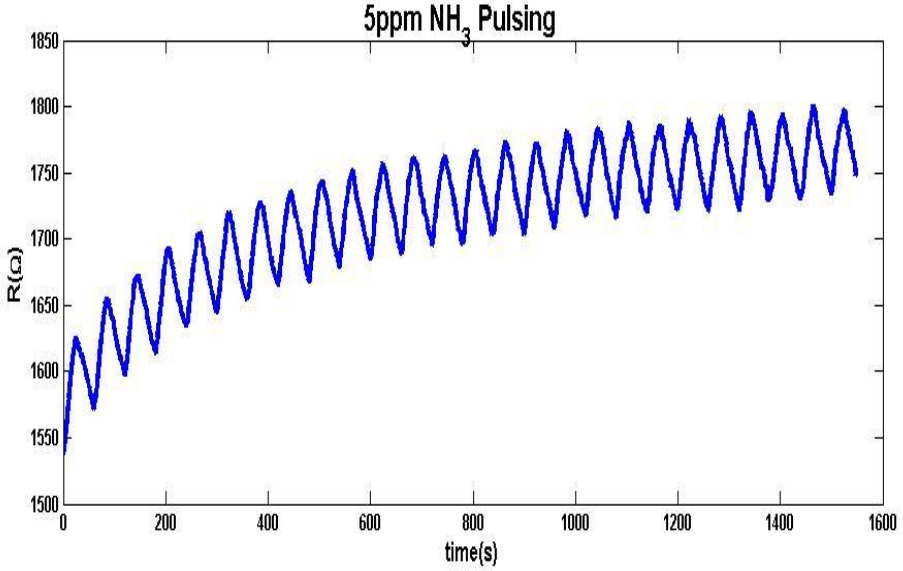

Figure 4.3 The reproducibility of the sensor's response was tested in order to control the stability of the sensing layer. The figure corresponds to 5 ppm ammonia pulsing on a porous silicon sensor. The ammonia is pulsed on and off every 30 s.

For a noise reduction or separation, we have developed a gas pulsing method [2]. Porous silicon gas sensors exhibit important characteristics for their application in a wide number of areas. They can be operated over a broad range of environmental temperature, pressure, and humidity fluctuations as it is possible to eliminate response variations due to such enviromental factors by operating in a gas pulsing mode. Through the introduction of this technique and frequency analysis, the linear low pressure gas response of the PS sensor can be separated from the effects of pressure, temperature, and humidity, and acquired, and filtered on a drifting baseline, further increasing sensitivity.

Figure 4.3 shows a typical pulsing experiment. The baseline for the device increases and plateaus as the adsorption and desorption of ammonia begin to equilibrate, but the signal is not saturated. However, the system might also be affected by low frequency changes in temperature and pressure. By introducing a Fast Fourier Transform (FFT) analysis to the PS gas sensor, the gas response can now be acquired and filtered on a drifting baseline or in the presence of these external noise sources. Since the applied pulse frequency is known, external noise can be eliminated and false positives can be evaluated.

Figure 4.4 shows the response of 30 ppm NH_3 on n^+ and n-type PS sensors. The sensor response is higher and response time is shorter for the n^+-type semiconductor interface compared to an n-type sensor because of the increased charge density on the surface. However, this response is limited by the surface morphology of PS. N-type PS anodization usually creates pores of a few 100 nm diameter on the surface and therefore the porosity of n-type wafers is lower compared to p-type PS surfaces. Another interesting point is that the response characteristics change as the type of majority carriers on the surface change. The p-type sensor resistance increases as opposed to a decrease for n-type sensors when the sensor surface is exposed to NH_3.

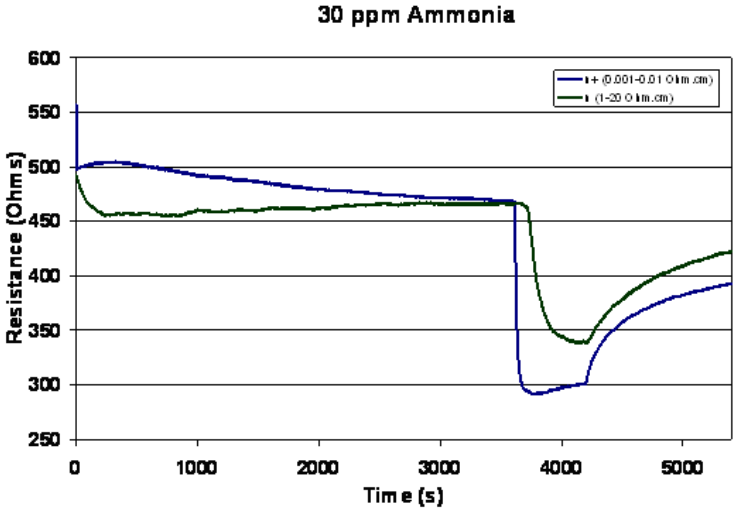

Figure 4.4. A comparison of the response to a 30 ppm NH_3 test on n^+ (blue) and n (green) -type PS sensors is depicted. The n^+-type sensors shows slightly better response time and strength.

The introduction of Au_xO nanostructures to the micro/nanoporous framework produces an enhanced sensitivity. The nanopore coated micropores (Figure 3.1) provide interaction sites for electroless gold coating, decrease the base resistance of the sensor significantly, resulting in lower heat dissipation and enabling lower power consumption. Results for gold deposition are depicted in Figure 4.5. An untreated sensor is tested before and after gold nanoparticle deposition with 1,2,3,4,5 ppm of NH_3, leading to a significant response increase.

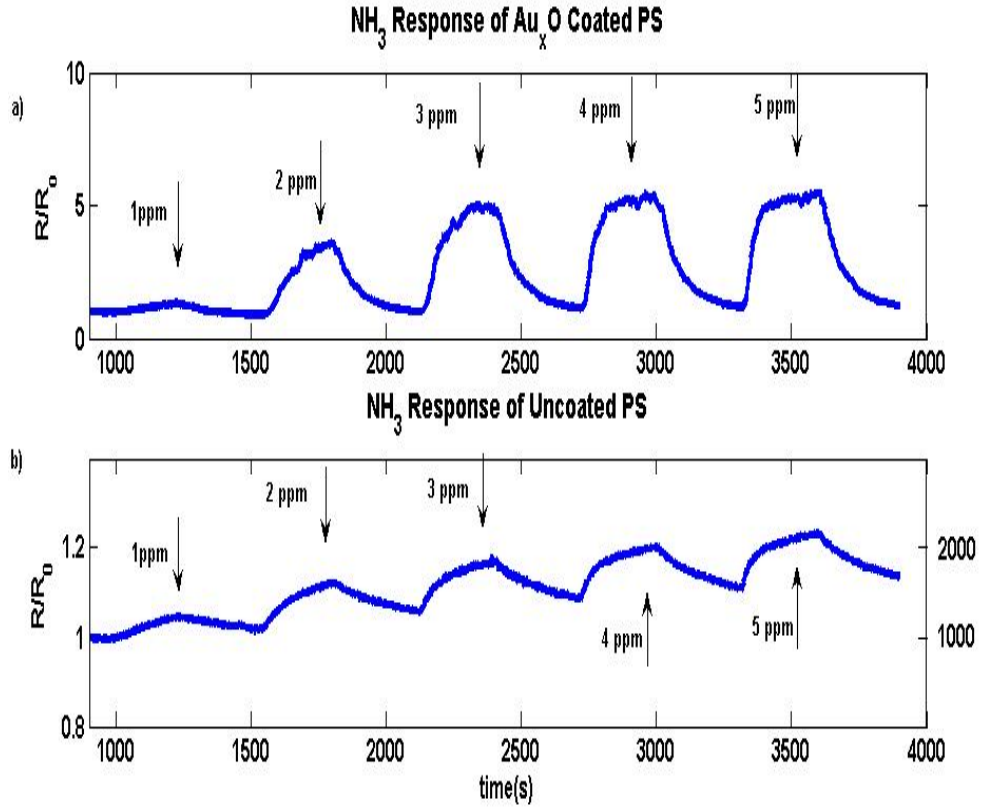

Figure 4.5 The bottom figure depicts an untreated PS sensor response when the PS surface is exposed to 1,2,3,4,5 ppm of NH_3. The top figure shows the response under the same test conditions after the PS sensor surface is treated with gold.

The introduction of gold to the micro/nanoporous PS framework, through electroless metal treatment, selectively modifies the resistance response to considerably improve the detection of NH_3 as shown in Figure 4.6. In this figure, we compare the current response to the previously published result [2] with the new results achieved

using the described fabrication methods. The same sensor is tested under the same conditions with 20 ppm NH_3 before and after electroless gold treatment. The new results, with an optimized PS surfaces show a several hundred ohm resistance change upon exposure to ammonia and, in addition, indicate that the gold treatment increases the sensitivity to ammonia by almost three times. The response is also reversible and the sensor resistance goes back to its base resistance at the end of each pulsing run. Thus, the response is found to be reproducible. The results also suggest a physical interaction between the sensor and the sensed gas which is consistent with the application of an acid-base concept. For both the untreated and gold treated sensor, 3V is applied to the pore region.

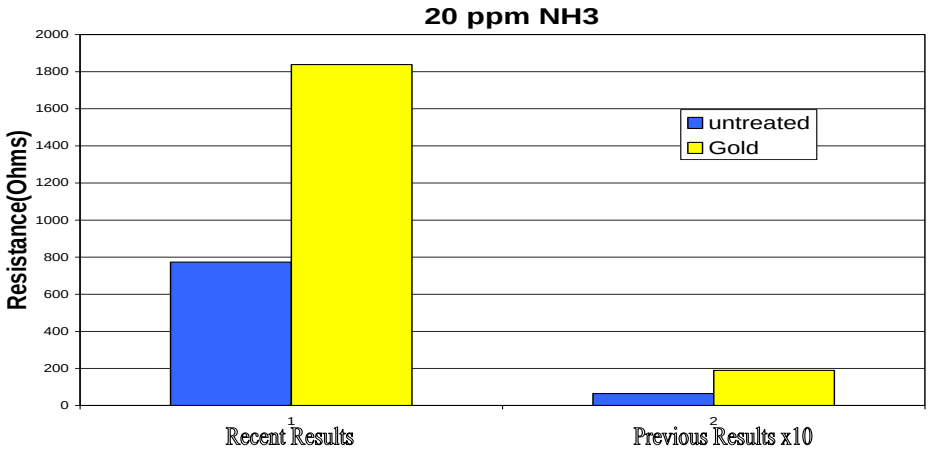

Figure 4.6. Response to 20 ppm NH_3 for both an untreated and a Au_xO coated PS sensor for 600 s pulse periods.

An important problem which plagues chemical sensors is the potential contamination of the sensor surface and the elimination of the sensor response over a long period of time. We have managed to treat sensors which have stopped responding for over one year as we rejuvenate their response. The ammonia response of such a sensor to 1,2,3,4,5 ppm of ammonia before and after the rejuvenation process is shown in Figure 4.7. The recovery of the sensor is clearly indicated.

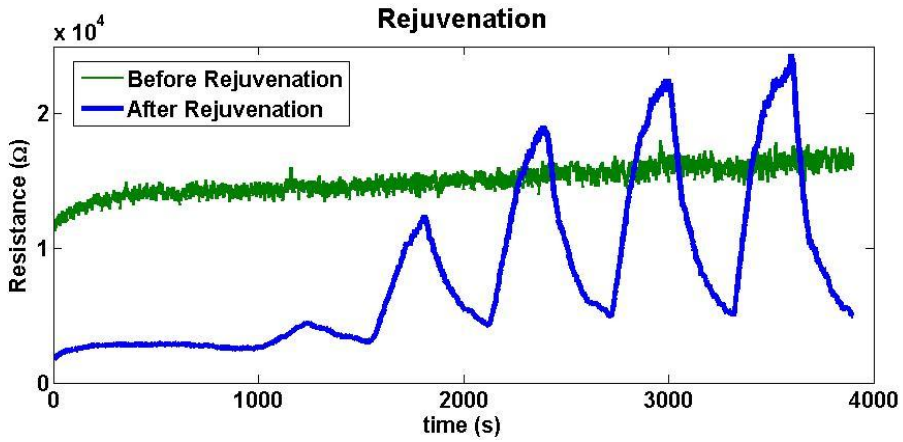

Figure 4.7. Response to 1 to 5 ppm NH_3 before and after rejuvenation of an old sensor.

4.2 Phosphine (PH_3) Detection

In this section, we discuss the selective modification of porous silicon (PS) conductometric gas sensors for phosphine detection. Tin, nickel, copper and gold are electrolessly deposited onto nanopore covered microporous porous silicon surfaces forming SnO_x, NiO, Cu_xO and Au_xO nanostructured centers (Figure 3.1). Further studies have also been carried out with nanostructured alumina coated porous silicon. The sensitivity change of these modified porous silicon gas sensor surfaces has been measured under 1–5 ppm PH_3 exposure. An improved sensitivity, of the order of 5 times that of untreated porous silicon, for 1 ppm exposure is observed for gold treated sensor surfaces. The selection of the nanostructure deposition, which will be discussed in detail in Chapter 5, is based on the hard to soft acid character of the nanostructured deposit and its subsequent effect on the physisorption of PH_3. We have focused on the application of simple nanostructured deposits on a hybrid PS interface to significantly change the interface sensitivity. The application of nanostructured metals, metal oxides, and nanoparticle catalytic coatings promotes considerable enhancement of the PS interface sensitivity. We have developed nanopore covered microporous Si surfaces subsequently treated with minimal procedures to form nanoparticle and cluster deposited surfaces that

can be used in combination to form gas sensor arrays. To facilitate this array design, a better understanding of the selection of nanostructured materials to modify the PS framework is necessary. An approach to predict significant changes in sensor surface response for a variety of gases, based on a modification of the concept of hard and soft acid and base interactions, has been investigated by testing the sensitivity of several nanostructure modified interfaces.

Phosphine is an extremely toxic gas widely used in agriculture for fumigation [12]. It is the only widely used fumigant that kills insects rapidly without leaving residues on the product. An additional application area is in the semiconductor industry as a dopant in silicon processing. PH_3 is also an illicit product of methamphetamine (meth) labs [13]. There is a recent considerable need for locating the signatures of these illegal meth labs without breaking and entering the large number of small scale facilities which are producing "meth" and continue to increase throughout the United States. The Occupational Safety and Health Administration (OSHA) sets a limit of exposure of 0.3 parts per million (ppm) PH_3 for an 8 h workshift, and 40 h a week [14]. Here, we outline the use of a PS gas sensor to detect PH_3 and investigate response variations to the deposition of a variety of nanostructured metal oxide deposits.

The sensor testing experiments are performed in a chemical hood at room temperature, atmospheric pressure, and virtually constant humidity. Our objective is to use PS sensors to detect hazardous gas mixtures in cleansed air with a sensor array format of various nanoparticle depositions. PH_3 (1000 ppm diluted in N_2 – Matheson) is diluted to the specific desired concentrations via mixing with ultra high purity (UHP) N_2 (Matheson 99.999%) employing computer controlled mass flow controllers. This analyte is exposed to an untreated and four distinct nanostructure modified PS surfaces (sensors). The appropriate treatments (see Chapter 3) create SnO_x, NiO, Cu_xO, and Au_xO nanostructured islands on the PS surface. Microprobes are utilized to measure the

resistance change of the sensors when different concentrations of nitrogen entrained PH_3 are pulsed onto the sensor at room temperature (Please see Chapter 2 for details of the experimental apparatus). Each sensor is tested before and after electroless deposition. The base resistance of the sensor is typically a few hundred ohms, but can range to a few kΩ. The surface of the sensor is flushed with UHP N_2 for 30 min to 1 h to assure base resistance stabilization at the beginning of each experiment. Further, the data in Fig. 3.7 obtained for the O 1s XPS peak for the five surfaces considered demonstrate an extremely low OH concentration. This may result from the hydrophobic nature of the PS surface [15] and the nature of the limited nanostructure deposits to this surface. One might envision these nanostructured islands as enhancing sites for the dominantly PS structure.

We summarize the response changes after SnO_x, NiO, Cu_xO and Au_xO nanostructures are deposited to the native PS interface in Fig. 4.8(a)–(d), respectively. Since there may be OH groups and hydrocarbons originating from the air deposited onto the sensor surface, we always perform relative measurements, comparing the untreated PS sensor and nanoparticle deposited PS. These relative measurements are depicted in Fig. 4.8. Following a base resistance stabilization with a greater than atmospheric pressure N_2 flow for 30–60 min at room temperature, PH_3 is pulsed onto the sensor every 300 s in half cycles. The UHP N_2 purge for extended periods at a base stabilized resistance suggests that water condensation on the PS surface is at a minimum. The N_2 flow onto the sensor is kept constant at 100 sccm at all times during the experiment and diluted PH_3 is mixed with the N_2 flow as we test the sensor response to phosphine. The peaks in Fig. 4.8 correspond to an exposure to 1, 2, 3, 4, and 5 ppm of test gas, respectively. After the 300 s half cycle, we cease flowing PH_3 onto the sensor and refresh the surface with UHP nitrogen, decreasing the resistance of the PS layer as a result. All sensors are evaluated in an unsaturated mode since the time scale for reversibility may become an issue in a long term saturated mode and these longer term exposures are not necessary. Although we operate the sensors in an unsaturated mode, the sensor response and recovery times are distinctly different and full time recovery from the gas exposure

takes longer than 300 s which is the exposure time duration in the present configuration (Fig.4.8). However, the onset of the sensor response remains clearly visible. This behavior suggests that the PH_3 response on PS is that of a 'sticky' gas whose interaction may be dominated by physisorption but which also displays weak chemisorption. Purging the sensor surface with UHP N_2 for longer durations improves the gradual shift to the initial base line. The return to baseline can also be further improved by more tightly constraining the gas flow path to the sensor surface [16].

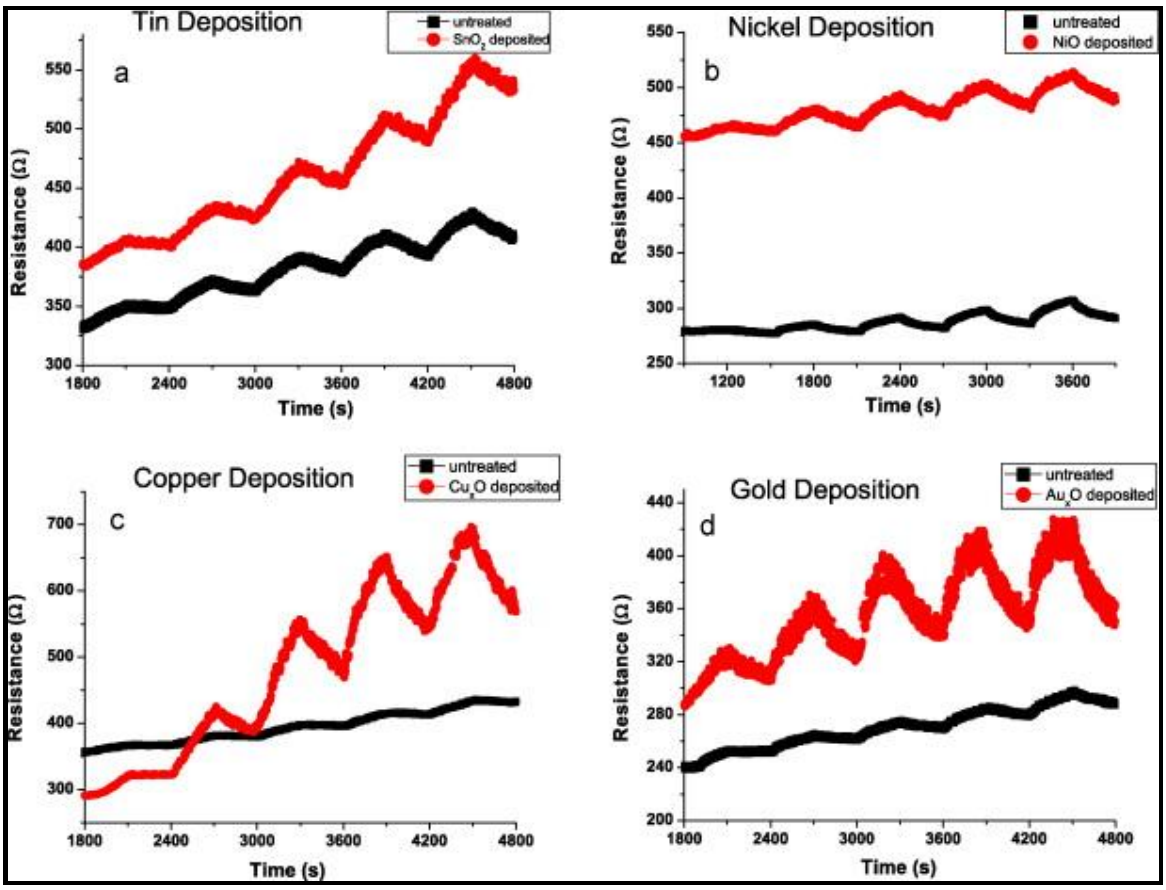

Figure 4.8. PH_3 response to different nanostructure depositions. 1, 2, 3, 4, and 5 ppm of PH_3 is pulsed onto metal oxide nanostructure modified sensors with a 300 s half cycle followed by a 300 s half cycle UHP N_2 cleaning.

We have observed an increase in response with respect to PS for the applied nanostructured deposits (SnO_x, NiO, Cu_xO, Au_xO) with the exception of Al_2O_3, as they form interactive nanostructured oxides on the PS surface. However, the responses for

each deposit are distinct and do not have the same magnitude for the same concentration of the tested gas. This feature allows us to begin to develop a selectivity matrix for the PS gas sensor, and PH_3 detection. For a 1 ppm exposure, the amount of resistance change per base resistance (Equation 4.2) for the nanostructure deposited and untreated sensors, is summarized in Table 4.1. The maximum enhancement per base resistance (a factor of approximately 5) is observed when the PS sensor is treated with electroless gold to form Au_xO deposits. The minimum change in relative resistance results from the use of Al_2O_3 followed by the most investigated gas sensing material, tin oxide. The relative response of the hybrid PS structure and an initially generated "Al_2O_3" nanostructure treated surface (see Section 2) appear to be virtually identical (Table 4.1), demonstrating that alumina may not offer the best advantages for PH_3 detection as previously envisioned [Chapter 1-Ref 55]

$$\Delta = \frac{\Delta R(treated)/R_0(treated)}{\Delta R(untreated)/R_0(untreated)} \qquad \text{(Equation 4.2)}$$

Table 4.1. Response increase (Eq. 4.2) for different catalytic metal depositions for 1 ppm exposure to PH_3.

Deposits	**SnO_2**	**Al_2O_3**	**NiO**	**Cu_xO**	**Au_xO**
$\Delta_{1\ ppm}$	2	1	2.5	4	5

For this series of experiments, the tin and gold treated PS surfaces (formation of SnO_x and Au_xO), base resistance change after surface modification is of the order of 50 Ω for the PS surface prepared in this study. We find that the formed NiO deposited sensor shows a large increase in base resistance. In contrast, the copper deposition levels used in the present experiments lower the base resistance of the sensor by approximately 50 Ω. This could indicate that the Cu_xO deposits are at too high a concentration on the porous layer and demonstrates the importance of controlling the nanostructure deposition to a

low level. This can be accomplished by varying the duration of the immersion of the sensor in the electroless copper solution (typically a time scale of tens of seconds). By analyzing the change in the base resistance drift, it is also possible to determine the necessary exposure for electroless metal deposition (the desired Cu_xO nanostructure concentration for a given base PS structure).

We have defined the sensitivity as the slope of the response per initial base resistance [2] of the PS layer and summarized the results for each of the considered electroless deposits for 1–5 ppm PH_3 exposure in Fig. 4.9. Up to the 3 ppm level, the sensitivity is approximately linear for all of the nanostructured deposits exposed to PH_3. At higher concentrations, the sensitivity begins to level off and decrease. This behavior suggests that the nanostructured deposits are most effective at lower concentrations and that they appear to display an irreversible degradation at higher concentrations of PH_3, which might, in fact, be the result of sensor poisoning due to strong chemisorption. The sensor response is primarily proportional to the strength of the interaction between the metal depositions on the PS interface and PH_3, whereas the reversibility of the response is inversely proportional to this interaction. Although the sensitivity inherent to the Cu_xO deposition seems to reach higher levels with an increase in PH_3 gas concentration as shown in Fig. 4.8, the Au_xO deposition is a better candidate for PH_3 detection. This follows from the behavior recorded in Fig. 4.8(c) where the drift in the average resistance increases drastically, implying a notable decrease of reversibility with increasing concentration. These results suggest that it is more practical to use the tuning of interspersed nanoparticle/cluster deposits on the PS surface so as to adjust response strength and ease of reversibility, and that this tuning has associated with it an optimum nanostructured oxide concentration.

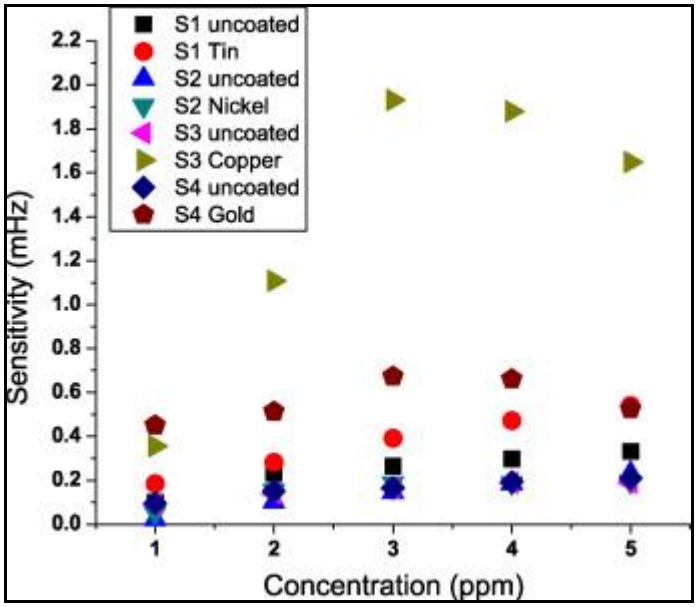

Figure 4.9. Sensitivity change for metal oxides formed with electroless metal treatments.

4.2.1 Metal oxide nanostructure deposit selection for PH_3

Nanostructured metal oxide treatments to modify the surface activity of PS have been employed to modify the physisorption/weak chemisorption for a PH_3, PS gas sensor. In order to explain this behavior, we have developed a complementary concept to that formulated by Pearson [17] for hard and soft acid base (HSAB) interactions. In the HSAB concept [17], which was developed for aqueous solutions, the interaction strength is correlated with the relative acidity and basicity of several surveyed reactants which are exemplified in Table 4.2. The ions and molecules indicated in this table, as they interact to form complexes and molecules are classified as strong, borderline, or weak acids and bases dependent on their binding as ligands. Hard species, both acids and bases, tend to be small slightly polarizable species and soft acids and bases tend to be larger and more polarizable. Further, the Pearson principle states that strong acids react with strong bases and weak acids interact with weak bases, resulting in significant ionic and covalent bonding, respectively. In contrast, we have found that the nanostructure treated PS gas

sensor behaves in the physisorption/weak chemisorption regime, and we have developed an inverse IHSAB concept to explain this behavior in a recent study [16]. Here, the physisorption process is found to dominate for primarily strong acid–weak base and weak acid–strong base interactions. By assessing these trends in IHSAB, a first order selection can be made for the appropriate modification of the porous Si hybrid interface with nanostructured metal/metal oxide deposits to create a range of sensitivities for a number of gases.

Table 4.2 Hard, soft and borderline acid and bases are cataloged.

Table 2
Some examples of hard and soft acids and bases.

	Hard	Borderline	Soft
Acids	H^{+*}, Li^+, Na^+, K^+, Be^{2+}, Mg^{2+}, Ca^{2+}, Cr^{2+}, Cr^{3+}, Al^{3+}, SO_3, BF_3, Sn^{4+}, Ti^{4+}	Fe^{2+}, Co^{2+}, Ni^{2+}, Cu^{2+}, Zn^{2+}, Pb^{2+}, SO_2, BBr_3, Sn^{2+}, NO_2	Cu^+, Au^+, Ag^+, Tl^+, Hg^+, Pb^{2+}, Pt^{2+}, Hg^{2+}, BH_3
Bases	F^-, OH^-, H_2O, NH_3, PH_3	NO_2^-, Br^-	H^-, R^-, CN^-, CO, I^-

This (*) standard notation does not indicate an ion, but rather the effective charge of elements bound to a ligand. For example SiO_2 corresponds to Si^{4+} and SiO corresponds to Si^{2+}.

PH_3 is a moderately hard base. Thus, its position among the bases is indicated in Table 4.2. Table 4.2 summarizes primarily the acid–base strength of ions associated with the oxides. From this table, the inverse HSAB model suggests that PH_3 will give the best reversible response with Au_xO and Cu_xO deposits since Cu^+ and Au^+ are weak acids. $Ni^{2+}O$, a borderline acid (Ni^{2+}), provides a decreased response as it lies closer to PH_3, however this response is notably better than that for Al_2O_3 (Al^{3+}). The NiO response is also greater than that for $Sn^{4+}O_2$, however, the response to SnO_2 exceeds that for Al_2O_3 as the Al^{3+} ion represents a weaker acid which is even closer to PH_3. The inverse HSAB model [16] suggests that the proper combination of nanodeposition techniques could be employed to produce combinations of array based multiple sensor devices of varying sensitivity to a variety of gases and that a matrix of array responses can be correlated to selectivity for a given gas mixture.

4.2.2 Comparison to previous studies

The results we obtain in this study suggest the importance of gold clustered oxide nanostructures for the detection of PH_3 and correlate well with the observations of Nakano and Ogawa [18], made in the preparation of thin gold film electrodes for electrochemical sensors for phosphine and arsine. However, the present sensors are far more easily constructed than those obtained from ion plating into the surface of a polytetrafluoroethylene (PTFE) membrane. In concert with the results we have obtained previously for ammonia [19], the range of behaviors which we observe for phosphine with SnO_2 (Sn^{4+}), Al_2O_3 (Al^{3+}), NiO (Ni^{2+}), Cu_xO ($Cu^{1+,2+}$), and Au_xO ($Au^{0,1+}$) correlates well with the relative gas basicity of phosphine and ammonia which have measured proton affinities of 185 ± 4 [20] and 207 kcal/mol [21].

We suggest that a matrix of distinct and separable responses for PH_3 can be generated using the relatively simple deposition techniques that we have outlined and that this approach presents a cost effecting alternate to the more complicated copper [22] and combined zirconium–palladium doping of SnO_2 films [23]. The former study with copper is likely influenced by the known sensitivity of copper for phosphine used in fumigation. Further, the present studies demonstrate that alumina or the alumino silicates may not present surfaces which are as promising as those nanostructured metal oxide depositions whose response is depicted in Fig. 4.8. The data in Table 4.2, in fact, suggest that Sn^{4+} should represent a more sensitive nanostructured depositions than Al^{3+} to phosphine as the acidic character of Al^{3+} more closely matches the basic character of PH_3 [16]. This means that a stronger chemisorption by the Al_2O_3 seeded surface can compete with reversible physisorption.

4.3 Gas Transport and Response

The diffusion of the analyte species has been investigated in the nanopore and micropore regimes by numerical analysis. Comparing the response time of the hybrid porous sensor surface with numerical diffusion calculations on the pores, it has been suggested that Knudsen diffusion time scales dominate the sensor response. Knudsen diffusion is used to describe the behavior of gas molecules in narrow nanopores and suggests that collisions between gas molecules and pore walls are dominant interactions in the diffusion process. Fickian diffusion is used to describe the movement of gas molecules in larger pores (micropores in PS) where the collisions between gas molecules are the dominating interactions in the diffusion process. A transduction model is proposed based on nanopore limited gas diffusion and the experimental response and recovery data. In this section, by proposing a response mechanism which leads to an identifiable trend in PH_3 sensitivities, we provide simulations of our data using a 1D diffusion equation. Results obtained for an untreated PS sensor saturated response to PH_3 allow the characterization of the dimensions for the hybrid PS interface.

The PS gas sensor provides a response to the concentration of PH_3 through a change in the sensor resistance. The response is the result of the interaction of basic PH_3 molecules and the acidic porous Si reactive surface. The hybrid PS interface has two characteristic length scales. The first involves a microporous structure, 1-30 μm in length, and 1-2 μm in diameter, easily observed with SEM. The second is the nanoporous surface coating on the micropore walls. The gas response results as the analyte gas has diffused through the pores at these two length scales. While not evaluating the complete transduction mechanism, we propose a first order approximation for the experimental results in order to understand the time scales and diffusive properties of the PS gas sensor.

Monte Carlo simulations in micro and nano porous media has been used to understand the flow parameters in these regimes [24, 25]. In contrast, we start with the 1D diffusion-reaction equation (Equation 4.3) and solve it incorporating assumptions based on experiment, comparing these results with the experimental sensor response. In this equation, C is the concentration, D is the diffusion constant, and k is an experimental reaction parameter. L is the length of the pore. In order to model the diffusion associated with the PS gas sensor, we make two important assumptions. We assume that the hybrid porous silicon structure of the gas sensor has two characteristic pore scales; nanopore and micropore. We represent the entire sensor as a single pore-like structure assuming that the response change for one pore and the entire sensor response are directly proportional to each other. Here, the proportionality is a constant corresponding to the pore density on the surface. We assume that if one pore gives a ΔR resistance change in the response, N pores will give N times ΔR, which will be the total resistance change when the surface is exposed to a test gas. Since N is just a constant, we model the total response on the analyte diffusion in one pore.

$$\frac{\partial C(z,t)}{\partial t} = D\frac{\partial^2 C(z,t)}{\partial z^2} - kC(z,t) \qquad \text{(Equation 4.3)}$$

To identify the response change for each concentration of PH_3, we suggest a simple approach attributing the change of the resistance to the concentration of the gas in the saturated mode as indicated in Equation 4.4.

$$R = R_0 + C(t)S \qquad \text{(Equation 4.4)}$$

Here R is the resistance of the conductometric sensor. R_0 is the base resistance and S is an experimental sensitivity parameter which is calculated using experimental data obtained in the pulsing mode (Figure 4.10 (a)). Solving the diffusion equations with

experimental boundary conditions and incorporating the simulated C(z,t) into the response equation, we calculate a gauge parameter D/L^2. Since the diffusion constants and pore length scales in Fickian and Knudsen Diffusion are very different, D/L^2 in these two regimes is very distinct [Table 4.3]. We can compare the gauge parameter extracted from experimental response data with the average parameters calculated in these regimes and say in which regime the PS gas sensor is operating.

In the unsaturated mode of operation, the 1-5 ppm PH_3 response of an uncoated PS gas sensor and the results of the numerical simulations are shown in Figure 4.10(a). The duration of exposure is 600 s for both the experiment and simulation. Although the base resistance drift due to the variation between response and recovery duration is not incorporated in the simulations, we obtain reasonably good agreement with the non-saturated response. For the saturated case, we calculate the gauge parameter D/L^2, and vary this parameter to obtain the best fit from the combination of experiment and simulation. When the gas density is very low and the diffusion length is small, collisions between molecules can be ignored. This type of diffusion is common in nanoporous materials and is known as Knudsen Diffusion. The order of magnitude of the gauge parameters calculated for Fickian diffusion and Knudsen diffusion is summarized in Table 4.3.

Table 4.3: Fickian vs Knudsen Diffusion parameters with typical pore sizes.

	Fickian Diffusion	Knudsen Diffusion
D	$\sim 10^{-5}$ m^2/s	$\sim 10^{-7}$- 10^{-6} m^2/s
L_{pore}	1-20 μm	$< .1$ μm
R_{pore}	1-2 μm	1-10 nm
D/L^2	$\sim 10^5$ s^{-1}	$\sim 10^8$ s^{-1}

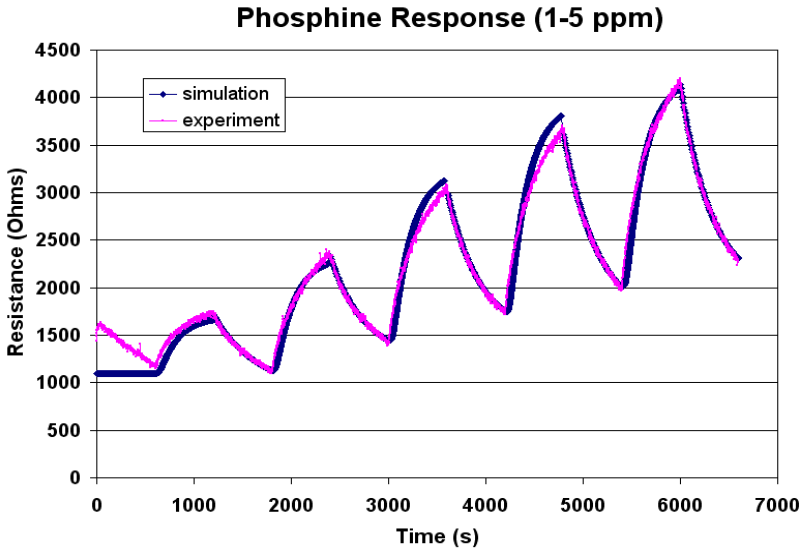

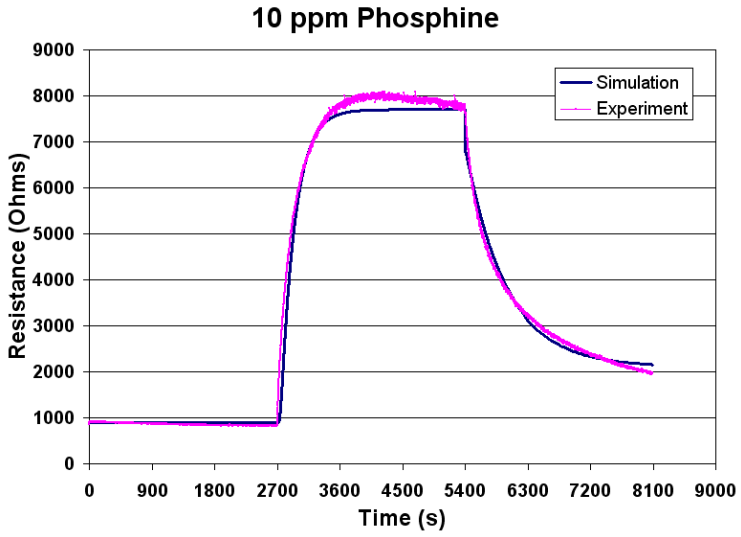

Figure 4.10 a) PH_3 response (1-5 ppm), experiment vs simulation in pulsing mode. b) PH_3 response (10 ppm) experiment vs. simulation in saturation mode.

We observed that the diffusion process (first term in Equation 4.3) is limiting the sensor response in the initial part of the gas pulsing. When the gas pulsing stops in the second part of the response graph where resistance starts to drop, the second term in Equation 4.3 (reaction term) dominates the response. The sensitivity which is around 600 Ω/ppm level starts to drop slowly as we test at higher concentration levels in Figure 4.10

(a). The reaction term, k, also varies for different concentration levels, which shows that response and recovery time scales are different.

To characterize a naked PS gas sensor, we have suggested a simple response description. We solve the 1D diffusion equation numerically by comparing with the experimental sensitivity. We have evaluated the order of magnitude dimensions of the hybrid PS porous layer, and the dominance of Knudsen diffusion, taking into account the time scales of the response process for both Fickian and Knudsen diffusion. Further improvements of the numerical model can be accomplished by working in higher dimensions as well as with more diverse pore structures. The response equation can also be improved by addition of other variables including the sticking coefficient, temperature, and humidity parameters. However, the results obtained clearly demonstrate the dominant effect of diffusion.

4.4 Nitric Oxide (NO) and Nitric Dioxide (NO_2) Detection

Porous silicon (PS) conductometric gas sensors have been developed to create a sensitivity matrix for the room temperature detection of NO_x (NO, NO_2). "P-type" nanopore coated microporous silicon is treated with tin, nickel, copper, and gold, electrolessly deposited onto the PS surface to form SnO_x, NiO, Cu_xO, and Au_xO nanostructured centers, The relative sensitivities of these modified PS gas sensor surface sites have been measured under 1-5 ppm NO exposure. An improved sensitivity of up to 10 times that of untreated PS is observed for a 1 ppm exposure of an SnO_x nanostructure deposited hybrid PS interface. The choice of the indicated nanostructured deposits is again based on the hard to soft acid character of the nanostructured metal oxide islands that are fractionally deposited on the semiconductor interface and their effect on the physisorption of NO, a weak base, dictated by an inverse pattern (IHSAB) to the hard-soft acid base concept. NO, a free radical, can interact with oxygen sites on the modified

PS sensor interfaces, to effect a transient NO_2 signal unique to PS-based NO sensors, which is not observed as other basic analytes including NH_3, PH_3, H_2S, SO_2, and CO interact with "p-type" PS.

Previously, we have outlined an approach which combines the concepts of acid/base interaction and the properties of extrinsic semiconductors, suggesting a general procedure to optimally design sensors with improved and variable sensitivity for a variety of gases, operating at room temperature in an array-based format [16,26,27]. The IHSAB concept is designed to facilitate highly variable physisorbed surface interactions using a diversity of nanostructured "*fractional*" oxide depositions which form islands on a porous silicon interface. These islands act as antennas to focus the nature of the *physisorbed* surface-interface interaction, while minimizing the chemical interaction of an acidic or basic analyte with the semiconductor. We promote electron transfer to (base) or from (acid) the surface of an extrinsic semiconductor and an interaction with the majority carriers for this extrinsic semiconductor. Here, using "p-type" porous silicon, we apply this approach to a study of the weak base, NO, and the moderate acid, NO_2, which can be formed from the interaction of NO with oxygen.

NO and NO_2 play important roles in disease detection [28,29] and in vehicle exhaust emissions[30-39]. Methods for non-invasive disease detection can provide highly desirable clinical probes [28,29] and NO, in particular, that is predominantly generated in the bronchial system, is a dominant indicator for asthmatic conditions and the inflammation which they cause. Further, the large quantities of NO produced in an asthmatic attack can combine with O_2 in breadth to produce NO_2. A simply constructed portable sensor capable of measuring significant NO (and NO_2) concentration changes in breath might be used on a regular basis to signify the onset of asthma attacks.

NO_2 also represents a toxic air pollutant emitted by combustion engines and has been the focus of several research efforts in sensor technology [30-41] where levels as

low as 12 ppb in dry air and 50 ppb in humid air have been reported for a p^+ substrate-based porous silicon sensor [30].

In this section, we demonstrate the development of an NO (NO_2) detection matrix, creating an array of nanostructure modified "p-type" *porous silicon* (PS) gas sensors whose distinct sensitivities, in part, take advantage of the weak basic character of NO in contrast to the moderately strong acid character of NO_2. In the course of this study, we observe the result of the interaction of NO with oxygen sites, on several of the modified porous silicon sensor interfaces, in a process that would appear similar to, but distinct from, that previously reported [31,32] for thin film n-type SnO_2 sensors at elevated temperatures, viz

$$NO + SnO_2 (O^-) \rightarrow SnO_2 (NO_2^-) \qquad \text{(Equation 4.5)}$$

$$SnO_2 (NO_2^-) \rightarrow SnO_2 (e^-) + NO_2 \qquad \text{(Equation 4.6)}$$

We study the room temperature detection of NO and its interaction to extract surface-based O atoms from both p-type PS and nanostructure modified p-type PS surfaces. Our observations suggest a process whereby O^- atoms are extracted from these PS surfaces. The mechanism of this process must involve either the transient removal of an electron from the PS interface or the formation of a transient acidic "NO_2" species, rapidly attracting the electron to form the moderately strong base NO_2^- adsorbed to the PS surface. Subsequently, both NO_2^- as a moderate to strong base and NO as a weak base can contribute electrons to the PS and treated PS interface as NO_2 desorbs and NO continues to interact. The behavior associated with NO, a free radical weak base, is distinctly different from that of NH_3, PH_3, H_2S and several additional basic analytes where the conductometric sensor signal does not indicate interaction with oxygen sites. We will suggest that this observed NO (NO_x) sensor behavior can be correlated by considering the coupling of acid/base theory with the properties of majority carriers in an extrinsic semiconductor [16,26].

We summarize the response changes of a native porous silicon interface to NO in Figure 4.11. Since there can be OH groups and hydrocarbons originating from the air deposited onto the sensor surface, we always perform relative measurements, comparing nanoparticle deposited PS with an untreated PS sensor. An N_2 flow onto the sensor is kept constant at 100 sccm at all times during the experiment and diluted NO is mixed with the N_2 flow as we test the sensor response to NO. The peaks in Figure 4.11 correspond to an exposure to 1, 2, 3, 4, and 5 ppm of test gas. This recorded signal corresponds to a quite respectable 2 Ohms/ppm. The signal is exactly reproducible after 5 pulsing cycles. In contrast to NO, it is to be noted that the introduction of NO_2, a moderately strong acid, to the "p-type" PS surface used in this study leads to a significant drop in resistance as demonstrated in Figure 4.12. By comparison, NO_2^- a moderate to strong base, is expected to produce a signifigant increase in resistance as it interacts and transfers an electron to p-type PS or nanostructure treated PS. The experimental observations can be correlated with the acid/base character of these analytes.

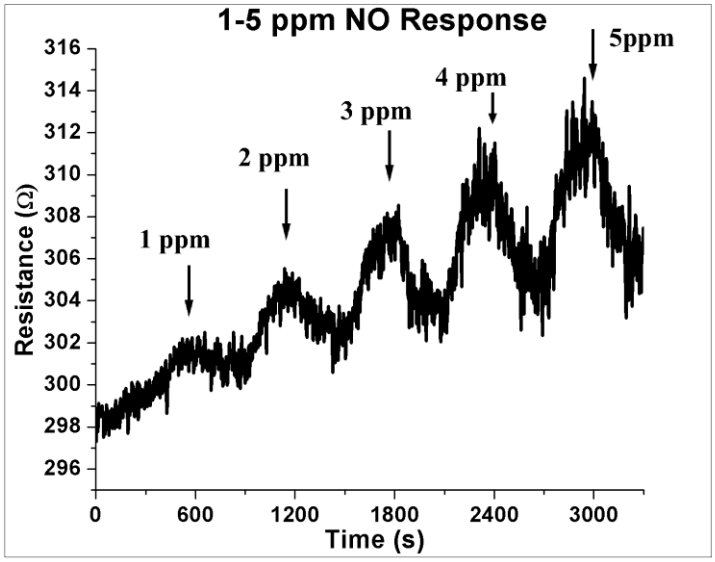

Figure 4.11. Relative sensitivity of PS to 1,2,3,4, and 5 ppm of NO for an untreated PS surface. The response is linear and close to 2 Ohms/ppm.

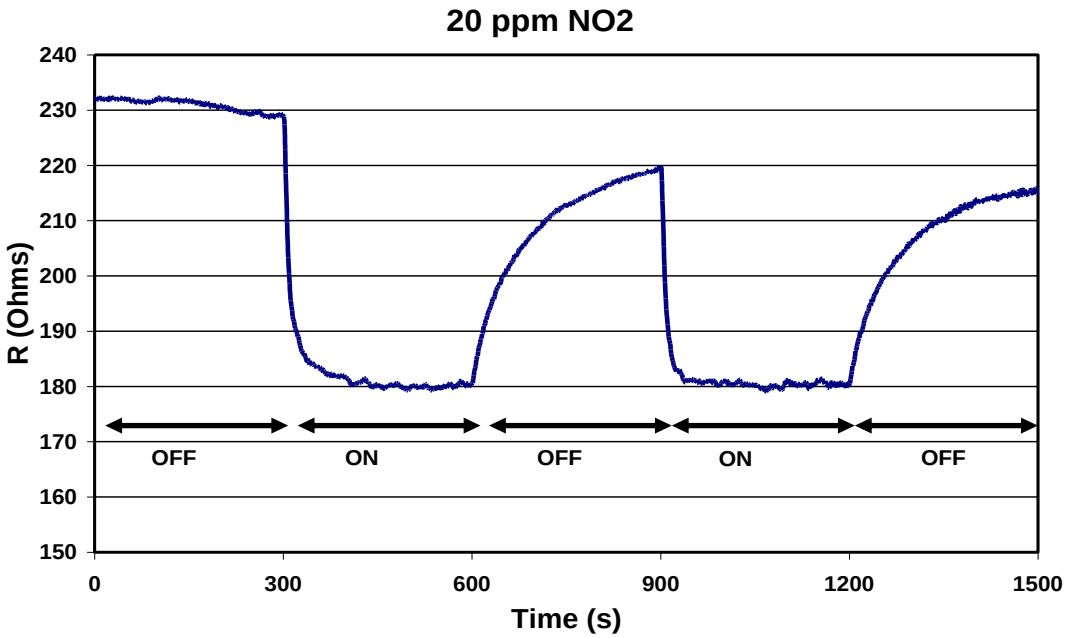

Figure 4.12: Response of NO_2 to the "p-type" PS sensors used in this study. The return to baseline is not complete at this concentration as NO_2 sticks to the surface in this open experimental configuration (Ref. 40-Fig. 2).

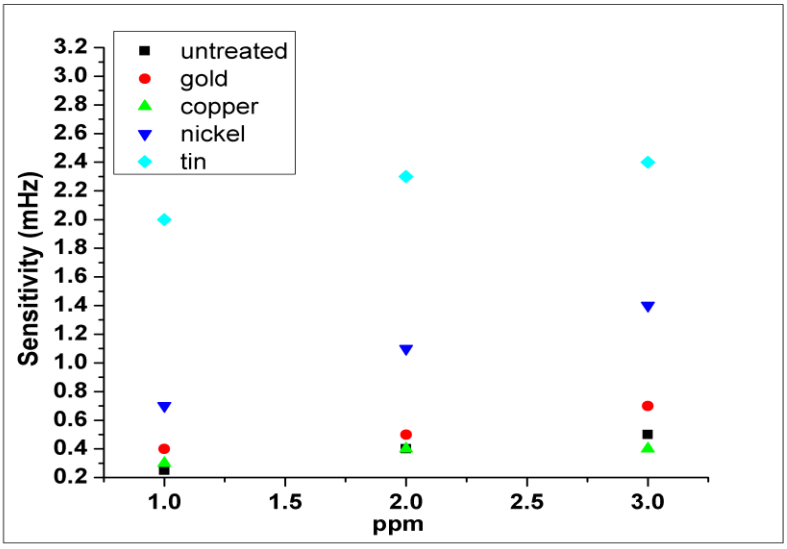

Figure 4.13: Sensitivity change for metal oxides formed with electroless metal treatments. The sensitivity is highest for SnO_x and NiO depositions.

We summarize the response changes to NO relative to native PS after SnO_x, NiO, Cu_xO, and Au_xO nanostructures are deposited to the PS interface in Figure 4.13. We have observed a clear increase in the response for NO with respect to PS for the surfaces treated with nanostructured deposits of SnO_x, NiO, and Au_xO (x>>1). Cu_xO, however, appears to offer little improvement. The responses for each nanostructure deposited surface are distinct and do not have the same magnitude for the same concentration of the tested gas. This feature allows us to begin to develop a selectivity matrix for the PS gas sensor-NO detection. For a 1ppm exposure, the amount of resistance change per base resistance for a nanostructure deposited vs. an untreated sensor, Equation 4.17, is summarized in Table 4.4. The maximum enhancement per base resistance (a factor of approximately 7-10) is observed when the PS sensor is treated with electroless tin to form SnO_x deposits (islands) on the PS surface. The minimum change in relative resistance results from the use of electroless copper and the formation of nanostructured Cu_xO islands on the PS surface [27].

$$\Delta = \frac{\Delta R(deposited)/R_0(deposited)}{\Delta R(untreated)/R_0(untreated)} \qquad \text{(Equation 4.7)}$$

Table 4.4. Approximate response increase (Eq. 5) for different catalytic metal oxide coatings for 1 ppm exposure to NO (vs. an untreated PS surface).

Deposits	SnO_2	NiO	Cu_xO	Au_xO
Δ_{1ppm}	7–10	3.5	1	1.5-2

The free radical nature of NO and its potential for the trapping of oxygen atoms on a semiconductor surface can provide an intriguing active environment. There are additional response changes as an NO gas flow is introduced to the PS interface and the SnO_x, NiO, Cu_xO, and Au_xO nanostructure deposited PS interfaces. The relative responses observed during cycles of NO introduction to each of the nanostructure deposited vs. untreated PS interfaces, are depicted in Figs. 4.14 (a-d). The resistances indicated on the right horizontal axis for the SnO_x and Au_xO treated PS surfaces increase

relative to that of untreated PS whereas the resistance for Cu_xO remains the same and that for NiO decreases. These trends in resistance change are difficult to correlate with an n or p-type character associated with the deposited nanostructure islands, a resultant semiconductor junction with the p-type PS surface, or the observed trends in response given in Table 4.4. Following a base resistance stabilization with a greater than atmospheric pressure N_2 flow for 30-60 min. at room temperature, NO was pulsed onto the sensor every 300 s in half cycles. After a 300 s half cycle, we cease flowing NO onto the sensor and refresh the surface with UHP nitrogen. All sensors are evaluated in the saturation mode, however, we have indicated the long term steady-state response as the sensor reaches saturation for the SnO_x treated PS surface in Figure 4.14 (e).

The data in Figure 4.14 demonstrate a distinctly different initial response to NO than that observed for other basic gases including NH_3, PH_3, and H_2S. After an initial baseline stabilization, the introduction of NO to either an untreated or nanostructure deposited PS interface at first produces a "surprising" sharp spike-like drop in resistance. This is followed by a gradual increase in resistance until the signal plateaus and subsequently the NO introduction ceases. The sensors, then bathed in UHP N_2, return to their baseline resistance. The process when repeated will produce a series of spike-like features of diminishing intensity (Fig. 4.15). We interpret the observed process by dividing the data in Figures 4.14(a)-(d) into regions. In the first region, the sensors are baseline stabilized using an N_2 flow. The process of baseline stabilization differs only slightly for each treated sensor. In the second region, NO is introduced and the resistance drops sharply. This result is not indicative of the interaction of a weak base with the PS or treated PS interface. This is a surprising response for the weak base NO, especially upon comparison with the bases NH_3, PH_3, and H_2S (see also Fig. 4.15). It is suggested that this resistance drop results as the NO free radical interacts and extracts oxygen atoms on the nanostructure modified porous silicon surface. In this process, the interacting oxygen atoms can remove an electron from the PS interface, or alternatively a transient ("NO_2"-

A

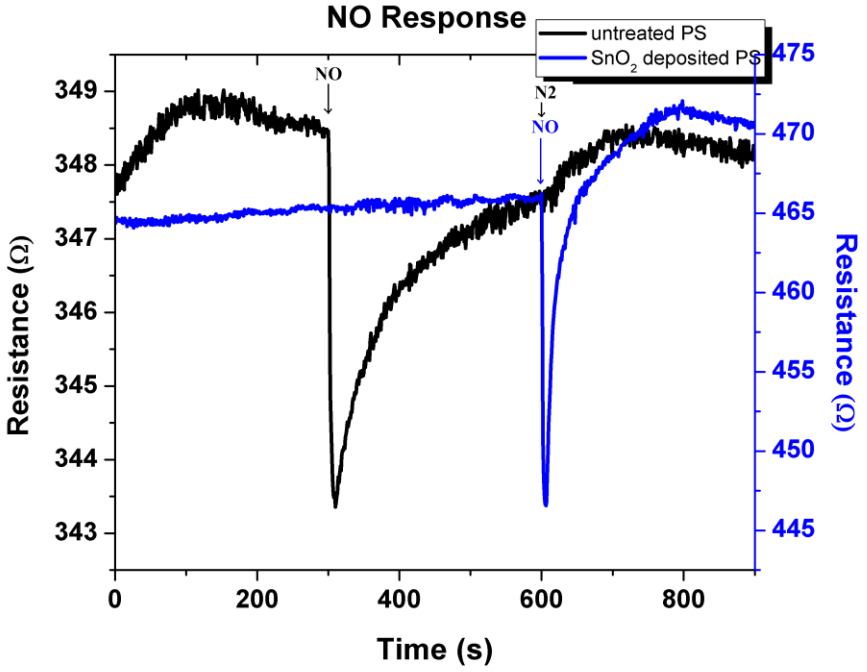
NO Response
untreated PS
SnO2 deposited PS
NO
N2
NO
Resistance (Ω)
Resistance (Ω)
Time (s)
349
348
347
346
345
344
343
475
470
465
460
455
450
445
0
200
400
600
800

B

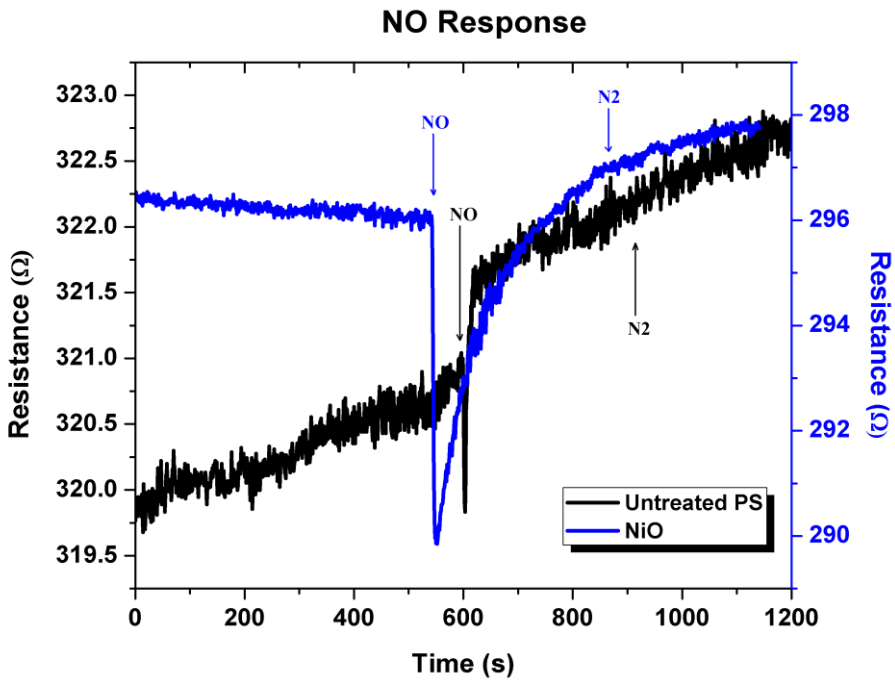
NO Response
NO
NO
N2
N2
Untreated PS
NiO
Resistance (Ω)
Resistance (Ω)
Time (s)
323.0
322.5
322.0
321.5
321.0
320.5
320.0
319.5
298
296
294
292
290
0
200
400
600
800
1000
1200

C

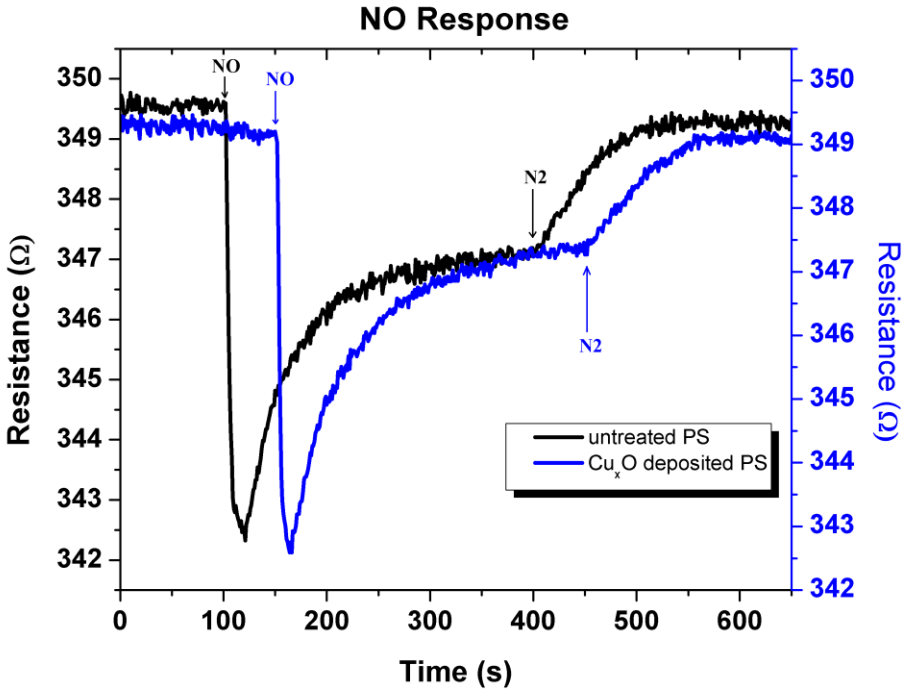
NO Response
NO
NO
N2
N2
untreated PS
Cu$_x$O deposited PS
Resistance (Ω)
Resistance (Ω)
Time (s)
350
349
348
347
346
345
344
343
342
0
100
200
300
400
500
600

D

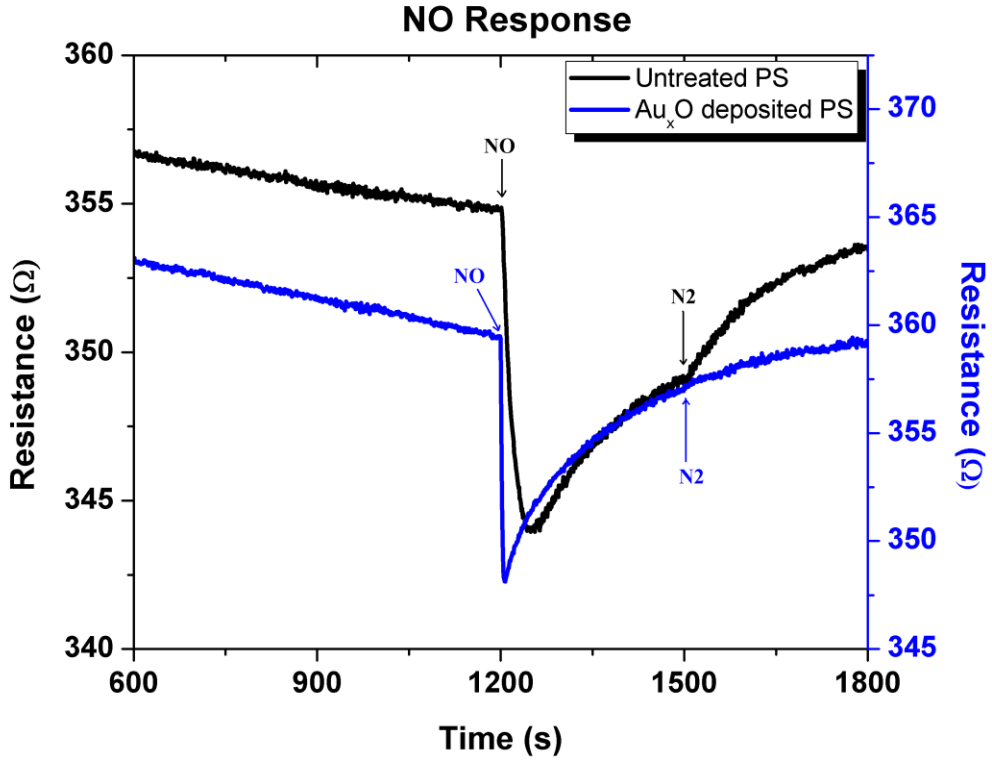
NO Response
Untreated PS
Au$_x$O deposited PS
NO
NO
N2
N2
Resistance (Ω)
Resistance (Ω)
Time (s)
360
355
350
345
340
370
365
360
355
350
345
600
900
1200
1500
1800

E

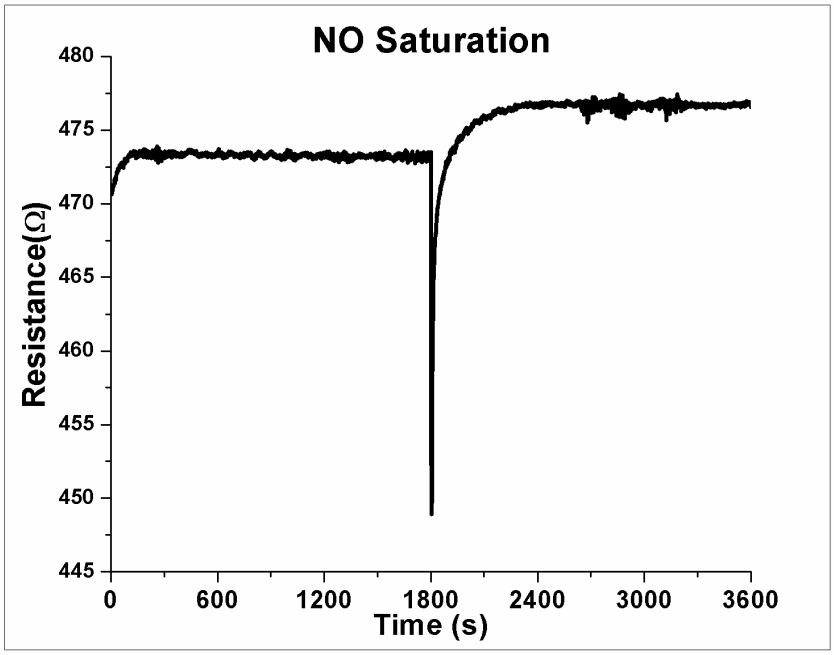

Figure 4.14: 1ppm response of untreated and SnO_2 (Fig. 4.14a), NiO (Fig. 4.14b), Cu_xO(Fig. 4.14c), Au_xO (Fig. 4.14d) nanostructure treated PS to NO. The first region corresponds to an N_2 purge for base resistance stabilization until NO is introduced. After 300 s of exposure, NO is turned off and the surface is purged with N_2. Note the scales to left (PS) and right (treated PS). Here the sensor is operated in an unsaturated mode. The saturation response to 10 ppm NO is depicted in Fig. 4.14 (e). Here, the sensor is exposed to N_2 for resistance stabilization for ½ hr. An initial transient formation due to electron removal and subsequent NO_2 formation is observed after the NO exposure. The sensor is saturated after 5 minutes of NO exposure.

electron) complex can form leading to NO_2^- , the initial transient processes leading to a signifigant decrease in resistance viz

$$NO + O^- \rightarrow NO(O^-) \rightarrow NO_2^-(ads.) \rightarrow NO_2 + e \qquad \text{(Equation 4.6)}$$

This conversion forms the moderately strong base NO_2^- which, as NO_2 desorbs from the PS surface contributes an electron, leading to an increase in resistance. Both NO_2^- formed from NO (Eq. 4.6) and NO can contribute an electron to the p-type PS surface, leading to the observed increase in resistance which follows the initial rapid transient decrease in resistance seen in Figures 4.14 and 4.15. We thus suggest that processes similar to but distinct from the mechanism outlined in Equations (4.3) and (4.4)

postulated previously [31,32] for the interaction of NO with n-type doped SnO_2 thin films at elevated temperatures, produces a transient removal of electrons from both the nanostructure treated and untreated p-type PS surface. This process can lead to the sharp decrease in resistance that is observed in Figure 4.14.

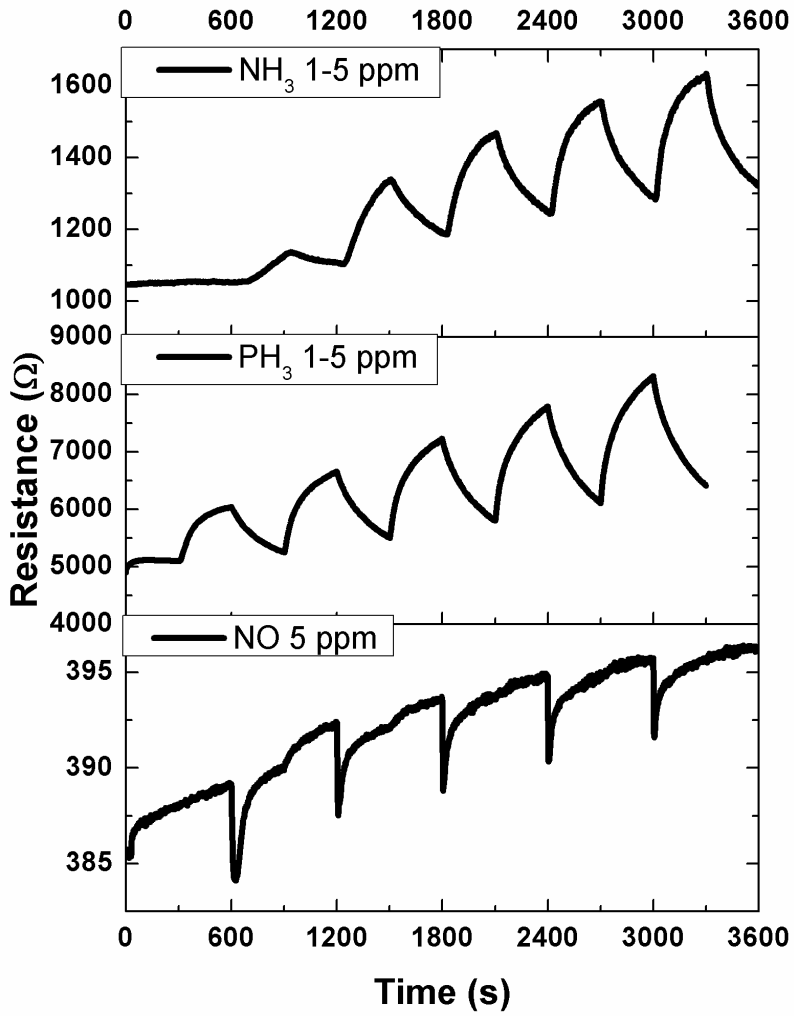

Figure 4.15: a) Sensitivity test for 1,2,3,4,5 ppm NH_3 , b) 1-5 ppm PH_3, and c) 5 ppm NO. The first region (600 s in the NH_3 and NO response and 300 s in the PH_3 response) corresponds to the N_2 purge of the sensor (in an open configuration) to obtain the optimal return to baseline . The sensor is exposed to the test gas for 300 s followed by a cut-off for the next 300 s. This cycle is run for 1 hr. The nanostructure deposition on the PS surface is tin oxide.

Because NO_2^- (ads.) (Eq. 4.6) is produced from the interaction of NO in 1:1 correspondence; we interpret the rise in signal in the region following the resistance minima of Fig. 4.14 as resulting from the interaction of NO with the modified p-type PS interface. We suggest that the resistance increases in response to the direct contribution of electrons from NO and through the contribution from NO_2^- (ads) (Equation 4.6) associated with NO_2 desorption where the NO has depleted the available oxygen atoms at the treated PS surface. In the final region, as the system is returned to the UHP N_2 purge gas flow, the response returns closely to "baseline". We evaluate the response to NO for the untreated and nanostructure treated PS sensors by comparing the resistance minimum and rise in resistance from the minimum point to the point at which the NO introduction to the sensor is terminated. In other words, we compare the resistance recorded at the minimum in the resistance response to that following and corresponding to the plateau region before the NO is no longer introduced to the sensor.

Although we operate the sensors in an unsaturated mode, there is some baseline drift and the sensor response and recovery times can differ. However, the data in Figure 4.14 suggests a rapid initial response and a reasonable recovery to baseline within the 300s window indicated for NO introduction followed by the N_2 purge reintroduction in Figure 4.14. Further, this corresponds to the recovery time for a rather open configuration (Fig. 2 – Ref. 2). The return to full baseline recovery can be further improved by more tightly constraining the gas flow path to the sensor surface as is discussed in Ref. 27. However, the long term return to baseline is indicated for the SnO_x treated PS sensor in Figure 4.14 (e).

4.4.1 Discussion

There have been several previous studies of NO and NO_2 [28-40], however, for the purpose of the present discussion, we will focus on the studies of Williams and Coles [31] and Sberveglieri et al. [32]. These authors have studied the response of several doped

SnO_2 films to NO_x (NO, NO_2). Sbverglieri et al. [32], in studying Cd doped n-type SnO_2 sensors, first observed a transient (~30s) "reverse sensitivity" (increase in conductance) followed by a decrease in the conductance when an NO/dry air mixture was introduced to the doped SnO_2 sensors. The process could not be observed when N_2 and argon were used as carriers. These authors attributed this behavior to the initial reaction of NO with surface oxygen atom species to form NO_2^- (Eqs. 4.5 and 4.6) with the subsequent injection of an electron into the conduction band of SnO_2, thus increasing the conductance. They suggested that this process was followed by NO_2 adsorption to the surface causing an electron depletion (majority carriers), the buildup of a Shottky barrier, and the decrease of the electrical conductance.

Williams and Coles [31] have studied the NO_x response of SnO_2 based sensors, SnO_2-Bi_2O_3, undoped SnO_2 calcined at 1500°C, and thin film SnO_2 generated from a sputtered Sn layer. In monitoring the SnO_2-Bi_2O_3 system at temperatures less than 300°C, the authors also found a transient reverse sensitivity, observed both in dry air and nitrogen gas, implying that NO can react directly with surface oxygen atoms on the semiconductor lattice. In contrast, they found that pre-calcined SnO_2 displayed a conventional (significant increase in sensor resistance) NO_x response for this n-type semiconductor device (at temperatures in excess of 265°C).

The two outlined studies both suggest the potential importance of surface oxygen atom interactions with NO to form NO_2^-. In the present study, carried out on a nanostructure modified "p-type" porous silicon interface at room temperature, we will suggest that the behavior observed in the present observation of a sharp transient dip in resistance can be explained through the coupling of NO_x acid/base chemistry with the properties of an extrinsic "p-type" semiconductor.

NO and NO_2^- correspond to a weak (soft) free radical and moderately strong base whereas NO_2 represents a moderately strong (hard) acid. In concert, the NO doublet free radical has a singly occupied HOMO as compared to the doubly occupied HOMO of

the bases ammonia and phosphine. The open shell nature of NO would suggest the possibility of a distinctly different interaction with "p-type" PS ([16] Please also see Chapter 6) and the nanostructure treated PS interface. In addition, NO can bind an electron which NH_3 and PH_3 cannot. These differences are born out through a comparison of the results displayed in Figure 4.15 where we compare the nature of the PS-based responses for NO, NH_3 and PH_3. We observe the transient decrease in resistance on a "p-type" or modified "p-type" PS interface only for the NO radical and not for the exemplary bases NH_3 and PH_3. In fact, we also do not observe this transient behavior for H_2S [16], SO_2, or CO [4,16], all moderate to weak (soft) bases. Further, as Figure 4.12 demonstrates, NO_2, a moderate acid, induces a decrease in the resistance of a "p-type" porous silicon surface as would be expected when an acid removes an electron from "p-type" PS and thus increases the majority carrier concentration. It is also relevant that the magnitude of the transient resistance decrease in Fig. 4.15 decreases with subsequent cycles. We suggest that this indicates the decrease of available oxygen atom sites available for interaction with NO.

The nanostructured metal oxide islands (Please see Chapter 3 for details) we have deposited to the surface of PS to increase the surface activity of PS have been selected to modify and direct physisorption/weak chemisorption for rapidly responding, reversible PS gas sensors. We have developed a complementary concept [16,27] (IHSAB) to that formulated by Pearson [17] for "hard" and "soft" acid base interactions in order to explain the trends observed in the responses of several PS sensor-analyte systems. In the HSAB concept [17], which was developed for *aqueous* solutions, the interaction strength is correlated with the relative acidity and basicity of several surveyed reactants which are exemplified in Table 4.2. The ions and molecules indicated in this table, as they interact to form complexes and molecules are classified as strong, borderline, or weak acids and bases dependent on their binding as ligands. Hard species, both acids and bases, tend to be small slightly polarizable species and soft acids and bases tend to be larger and more

polarizable. Further, the Pearson principle states that strong acids react with strong bases and weak acids interact with weak bases, resulting in significant ionic and covalent bonding respectively. In contrast, we have found that a nanostructure treated PS gas sensor can be made to behave in a reversible physisorption/weak chemisorption mode, developing the IHSAB concept to explain this behavior [16].

In the IHSAB model, the physisorption process is found to dominate for primarily strong acid-weak base and weak acid-strong base interactions. We force a mismatch between the molecular electronic structure of the treated PS surface and the analyte of interest to (1) maximize the reversible interaction with the surface, and (2) create an array of variable responses which provide a signature for the analyte of interest. By assessing the trends inherent to the IHSAB principle, a first order selection can be made for the appropriate modification of the PS hybrid interface with *fractional* nanostructured metal/metal oxide deposits to create a range of "reversible" sensitivities for a number of gases. It is important to emphasize that the nanostructured oxide deposits to which we refer act to influence the degree of physisorption at the PS interface and that these metal oxides do not coat the PS surface. The response of the sensor system, resulting in an increase or decrease in resistance is dictated to first order by the p or n-type character of the extrinsic semiconductor and whether interaction is with a basic or acidic analyte. Here, the fractional metal oxide deposition serves to enhance the degree of response of the modified "p-type" PS surface.

NO is a soft (moderately weak) base. Thus, its position among several bases as indicated in Table 4.2. Table 4.2 summarizes primarily the acid-base strength of ions associated with the oxides. From this table, the IHSAB model suggests that NO will give the best reversible response with an SnO_x modified PS surface since Sn^{+4} represents a strong acid. $Ni^{+2}O$, a borderline acid (Ni^{2+}), provides a decreased response as it lies closer to the weak base NO, however, this response is notably better than that of the weaker acid (Au_xO) $Au^{0,+1}$ which is again better than that for the somewhat harder acid (Cu_xO)

$Cu^{+1,+2}$. The soft base-hard acid interaction of NO with an SnO_2 nanostructured deposited surface leads to a substantial resistance response increase relative to PS. This is the signature of the reversible interaction of a strongly acidic site with a weak base [16]. The NO response to the gold, copper, and nickel treated PS interface (Table 4.4), while considerably muted relative to the tin treated surface provides distinctly different response changes which might be employed in an array-based format. The data suggests that the acid strength of a (Cu_xO) $Cu^{+1, +2}$ deposited islands on PS is closely matched to the base strength of NO. The gold clustered oxides represent highly weak acids which lie to the weak acid side of NO, again increasing the sensor response as a mild acid-base mismatch is promoted.

The IHSAB model [16] suggests that the proper combination of nanostructure deposition techniques can be employed to produce combinations of array based multiple sensor devices of varying sensitivity to a variety of gases and that a matrix of array responses might be correlated to selectivity for a given gas mixture. It is also important to note that the results in this study and similar studies [2,4,16,27] are obtained at room temperature using nanostructure deposits corresponding to islands on the PS surface and not a film coating. We have also observed that these systems can be operated at notably higher temperatures [42], increasing the observed resistance changes; however, it is important that we maintain a fractional nanostructure surface deposition. We have found that, as the concentration of the nanostructure deposit is increased, we observe the onset of noisy signals followed by a significant signal quenching. We attribute this behavior to increased cross-talk between the deposited nanostructured oxide islands [2,4,16,27] which can lead eventually to an effective shorting of the sensor response.

Within the framework of the IHSAB model, the observed trends are consistent with the observations of Sberveglieri et al. [32] and those of Williams and Coles [31]. The NO_2 molecule, as a moderately strong acid, withdraws electrons from the “p-type” PS surface increasing the majority charge carrier concentration and decreasing the resistance

(Figure 4,12). Thus, if NO_2 is created at the PS interface, we expect to observe a significant transient decrease in the resistance associated with the PS sensor. The process of electron withdrawal creates NO_2^- (ads.). NO_2^- and NO represent moderate and weak bases which both contribute electrons. This is consistent with an increase in resistance resulting as the interaction of the weak base, NO, and the desorption of NO_2 with subsequent transfer of an electron to the PS surface overcome the transient removal of electrons and deplete the majority carrier concentration. As the process indicated in Eq. 4 is repeated, the available surface O atom concentration is depleted and the magnitude of the transient response decreases (Fig. 4.15). By comparison, for an "n-type" semiconductor, the introduction of NO would be expected to increase the majority carrier concentration, leading to a decrease in resistance. The results that we obtain for "p-type" PS at room temperature, therefore suggest that the drop in conductance observed by Sberveglieri et al. [32] may indeed result from the formation of a Schottky barrier as NO_2 absorbs to their "n-type" SnO_2 surface.

It is relevant that we compare the positive aspects of the present sensor and complementary technologies. The present sensor system is capable of monitoring NO at the level of 650 ppb and NO_2 at a much lower level based on several additional tests in our laboratory. Levels of 12 ppb in dry air and 50 ppb in humid air have been reported for PS. These levels compare favorably with inexpensive advertised room temperature Electrochemical sensors (0-2500 ppm NO, 0-500 ppm NO_2)[43]. The notable attributes of the present inexpensive and low power consuming PS devices are detailed elsewhere [16,19]. Electrochemical sensors are also known for their low power operation, rapid response, and insensitivity to humidity and IT Gmbh [43] appears to have developed impressively sensitive and inexpensive devices.

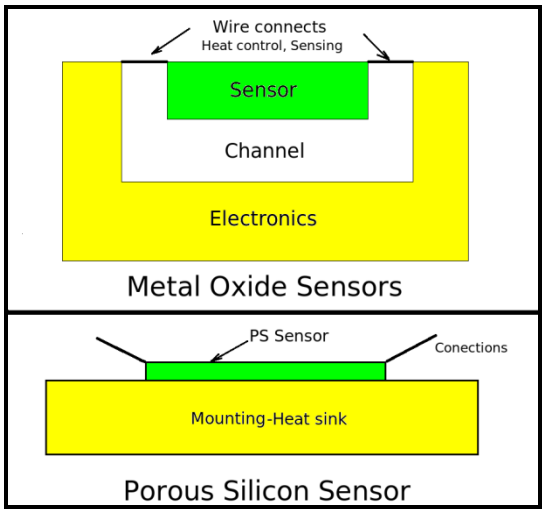

Figure 4.16 [44] Comparison of a metal oxide (usually SnO_2 or WO_3) elevated temperature (150-500C) heat controlled sensors separated from their electronics by a channel with a heat sunk PS sensor operating at room temperature and capable of operation to temperatures of at least 183 ^{0}C.

Traditional metal oxide sensors (Figure 4.16 [44]), when compared to electrochemical sensors are slightly less costly to produce, but are still significantly more complex than the PS sensor system considered in the present and other discussions [2,4,16,27]. Most importantly, they require a sensor element operative at elevated temperatures. The latter requirement can be problematic. First, a power consuming heating element must be provided with the sensor housing to precisely control the temperature of the sensor element. This control is, in large part, intimately tied to the correct identification of the gas of interest. The sensor must operate at well defined elevated temperatures for the valid identification of individual gases. Distinguishing one gas from another thus requires that the heating element and sensor be well separated (channel) from the remaining electronics. This in turn means that this configuration can be greatly affected by an impinging combustion or flue gas, rendering moot the correct identification of gaseous species in the flow. In contrast the PS sensor configuration depicted in Figure 4.16 [44] is far simpler and does not require the complexity of a system separated sensor/heater configuration [16]. In a heat sunk environment, it is potentially capable of operation in a high temperature gas flow. This simplicity and

capability of operation is significant. Further, the attributes of a porous silicon technology developed by combining array generation through the coupling of acid/base chemistry with the properties of extrinsic semiconductors suggests a general road map to array development, and an understanding of the nuances of this process.

4.5 Summary

In this chapter, some of the characteristic properties of the PS gas sensors are introduced. Test experiments performed with NH_3, PH_3, NO and NO_2 are discussed. Various nanoparticle depositions and gas sensor response modifications are investigated. As a result, an approach to understand these interaction strengths are initiated and some of these interesting results will be discussed through IHSAB model in detail in Chapter 5.

4.5 References

[1] http://www.figarosensor.com/gaslist.html (Last Accessed on March 5, 2011)

[2] S. Lewis, J. DeBoer, J.L. Gole and P. Hesketh, Sens. Actuators B: Chem., 110, 54 (2005).

[3] S.E. Lewis, J.R. DeBoer and J.L. Gole. Sens. Actuators B: Chem., 122, 20 (2007).

[4] J.L. Gole, S. Lewis and S. Lee. Phys. Stat. Sol. A, 204, 1417 (2007).

[5] (a) M. Schlesinger and M. Paunovic. Modern Electroplating, 4th Edn., John Wiley and Sons, New York (2000); (b) Fundamentals of Electrochemical Deposition, 2nd Edn., Wiley, New York (2006).

[6] G.L. Weller and S.J. Pratt, in Measuring Phosphine: How Sensors Work, E.J. Wright, M.C. Webb and H. Hightly Editors, Proceedings of the Australian Postharvest Technical Conference, Canberra (2003).

[7] J.A. Dirkson, K. Duval and T.A. Ring. Sens. Actuators B: Chem., 80,106 (2001).

[8] M. Mabrook and P. Hawkins, Sensors, 2, 374 (2002).

[9] L. Seals, L.A. Tse, P.J. Hesketh and J.L Gole, J. Appl. Phys., 91,2519 (2002).

[10] J.L. Gole, S.M. Prokes, O.J. Glembocki and R. Yang. Adv. Mater., 18, 664 (2006).

[11] J.L. Gole, J. Stout, C. Burda, Y. Lou and X. Chen, J. Phys. Chem. B, 108, 1230 (2004).

[12] B. Berck, Sorption of phosphine vy cereal products, J. Agric. Food Chem., 16, pp. 415–419 (1968).

[13] J.L. Burgess, "Phosphine exposure from a methamphetamine laboratory investigation", *J*. Toxicol. Clin. Toxicol. 39 (2001), pp. 165–168.

[14] Phosphine in workplace atmospheres, The Occupational Safety and Health Administration, January 2010, http://www.osha.gov/dts/sltc/methods/inorganic/id180/id180.html. (Last Accessed on, March 6, 2011)

[15] V. Zorba, L. Persano, D. Pisignano, A. Athanassiou, E. Stratakis, R. Cingolani, P. Tzanetakis and C. Fotakis, Nanotechnology 17, pp. 3234–3238 (2006).

[16] J.L. Gole and S. Ozdemir, "Nanostructure directed physisorption vs. chemisorption at semiconductor interfaces: the inverse of the hard-soft acid–base (HSAB) concept", ChemPhysChem 11, pp. 2573–2581 (2010).

[17] R.G. Pearson, "Hard soft acids and bases—the evolution of a chemical concept", Coord. Chem. Rev. 100, pp. 403–425 (1990).

[18] N. Nakano and S. Ogawa, "Preparation of thin gold-film electrode for an electrochemical gas sensor for phosphine and arsine", Sens. Actuators B, 20, pp. 51–55 (1994).

[19] S. Ozdemir and J.L. Gole, "Porous silicon gas sensors for room temperature detection of ammonia and phosphine", Chemical Sensors 8: Chemical (Gas, Ion, Bio) Sensors and Analytical Systems, ECS Transactions vol. 16, pp. 379–387 (2008).

[20] D. Holtz and J.L. Beauchamp, "Relative basicity of phosphine and ammonia in the gas phase", J. Am. Chem. Soc. 91, pp. 5913–5915 (1969).

[21] M.A. Haney and J.L. Franklin, "Heats of formation of H_3O^+, H_3S^+, and NH_4^+ by electron impact", J. Chem. Phys., 50, pp. 2028–2031 (1969).

[22] T. Ratcheva, I. Stambolova and K. Konstantinov, "Copper-doped SnO_2 thin films for PH_3 detection", Thin Solid Films, 207, 187–192 (1992).

[23] T. Ratcheva, I. Stambolova and K. Konstantinov, "PH_3 detection by SnO_2–ZrO_2 thin films", Sens. Actuators B, 20, 199–204 (1994).

[24] K. Malek, M. Coppens, "Knudsen self- and Fickian diffusion in rough nanoporous media", J. Chem. Phys., 119, 2801-11 (2003).

[25] S. Roy, R. Raju, H.F. Chuang, B.A. Cruden, M. Meyyappan, "Modeling gas flow through microchannels and nanopores", J. Appl. Phys., 93, 4870-9 (2003).

[26] JL. Gole, S. Ozdemir, "Efficient Nanostructure Modified Interfaces for Array-based Sensing Based on the Novel Application of Hard/Soft Acid/Base Interactions,", Phys. Stat. Solidi., in press.

[27] S. Ozdemir, JL Gole, Sens. and Actuators B, 151, 274-280, (2010).

[28] (a) W. Miekisch, J.K. Schubert, G.F.E. Noeldge-Schomburg, Clinica Chemica Acta, 347, 25-39 (2004) ; (b) P.P.R. Rosias, E. Doompeling, H.J.E. Hendriks, J.W.C.M. Heijnens, R.A.M.G. Donckerwolcke, Q. Jobsis, Pediatric Allergy and Immunology, 15, 4-19 (2004).

[29] (a) M.R. Zeilder, E.C. Kleerup, D.P. Tashkin, Current Opinions in Pulmonary Medicine, 10, No. 1:31-36 (2004); (b) S.A. Kharitonov, P.J. Barnes, Biomarkers, 7, 1-32 (2002).

[30] L. Pancheri, C.J. Oton, Z. Gaburro, G. Soncini, and L. Pavesi, Sens. and Actuators B, 89, 237-239 (2003).

[31] Geraint Williams and Gary S.V. Coles, Sens. and Actuators B, 15-16, 349-353 (1993).

[32] G. Sberveglieri, S. Groppelli, and P. Nelli, Sens. and Actuators B, 4, 457-461 (1991).

[33] L. Boarino, C. Baratto, F. Geobaldo, G. Amato, E. Comini, A.M. Rossi, G. Faglia, G. Lerondel, G. Sberveglieri, Mat. Sci. Eng. B Solid, 69-70, 200-204 (2000).

[34] S. Ozdemir, J.L. Gole, Curr. Opin. Solid Stater Mater. Sci. 11, 92-100 (2007).

[35] C. Burratto, G, Faglia, E. Comini, G. Sberveglieri, A. Taroni, V. La Ferrara, L. Quercia, and G. Francia, Sens. and Actuators B, 77, 62-66 (2001).

[36] M.J. Sailor, in: L. Canham (Ed.), Properties of Porous Silicon. IEE, London, UK, 1997, pg. 364.

[37] S.R. Morrison, Sensors and Actuators, 2, 329-341 (1982).

[38] S.R. Morrison, Sensors and Actuators, 12, 425-440 (1987).

[39] G. Heiland, Sensors and Actuators, 2, 343-361 (1982).

[40] S.C. Chang, IEEE, Trans. Electron Devices, ED26, 1875-80 (1979).

[41] S.C. Chang, J. Vac. Sci. Technol., 17, 366-369 (1980).

[42] J. DeBoer, S. Lewis, and J.L. Gole, unpublished.

[43] http://www.it-wismar.de. (Last Accessed on March 7, 2011)

[44] Serdar Ozdemir, Thomas B. Osburn, James L. Gole, "A Nanostructure Modified Porous Silicon Gas Sensor Detection Matrix for NO with Demonstration of the Transient Conversion of NO to NO_2" submitted to Journal of Electrochemical Society.

CHAPTER 5

THE INVERSE OF THE HARD SOFT ACID BASE (HSAB) CONCEPT

A concept, complementary to that of hard and soft acid–base interactions (HSAB-dominant chemisorption) and consistent with dominant physisorption to a semiconductor interface, is presented in this chapter. We create a matrix of sensitivities and interactions with several basic gases. The concept, based on the reversible interaction of hard-acid surfaces with soft bases, hard-base surfaces with soft acids, or vice versa, corresponds (1) to the inverse of the HSAB concept and (2) to the selection of a combination of semiconductor interface and analyte materials, which can be used to direct a physisorbed vs chemisorbed interaction. The technology, implemented on nanopore coated porous silicon micropores, results in the coupling of acid–base chemistry with the depletion or enhancement of majority carriers in an extrinsic semiconductor. Using the inverse-HSAB (IHSAB) concept, significant and predictable changes in interface sensitivity for a variety of gases can be implemented. Nanostructured metal oxide particle depositions provide selectivity and complement a highly efficient electrical contact to a porous silicon nanopore covered microporous interface. The application of small quantities (much less than a monolayer) of nanostructured metals, metal oxides, and catalysts which focus the physisorbtive and chemisorbtive interactions of the interface, can be made to create a range of notably higher sensitivities for reversible physisorption. This is exemplified by an approach to reversible, sensitive, and selective interface responses. Nanostructured metal oxides developed from electroless gold (Au_xO), tin (SnO_2), copper (Cu_xO), and nickel (NiO) depositions, nanoalumina, and nanotitania are used to demonstrate the IHSAB concept and provide for the detection of gases, including NH_3, PH_3, CO, NO, and H_2S, in an array-based format to the sub-ppm level.

In order to meet the criteria necessary for the detection, monitoring, and transformation of a diversity of materials and effluents, gas sensors and microreactors adopt a multitude of configurations. Conductometric gas sensors can be made to consist of a sensitive surface layer that can be transformed through the introduction of nanostructures. These sensors, which are conducive to the rapid and reversible transduction of sub-ppm levels of analyte gas, offer a most attractive subgroup [1,2]. Because of the strongly interacting nature of nanostructures, arrayed configurations capable of highly distinct, predictable, and inexpensively calibrated responses for a prescribed set of analyte gases, at room temperature, would represent ideal devices for a diversity of applications [1]. Efforts to form such devices utilizing a hybrid nano/microporous silicon medium as the transduction site have produced individual gas sensors [1-4]. Herein, we outline a concept, based on the inverse of the hard and soft acid–base interaction model (IHSAB), which suggests a general approach to optimally design sensors with improved sensitivity for a variety of gases. This concept also complements microreactor design. The selective fractional deposition of nanostructured materials to the surface of a prepared semiconductor interface can be used to create, in combination, microfabricated arrays with integrated complementary metal oxide semiconductor (CMOS) circuits. The IHSAB principle/approach is complementary to that of hard and soft acid–base interactions (HSAB) first put forth by Pearson, et al.[5] and later correlated within the context of density functional theory (DFT) and chemical reaction theory (CRT) by Pearson, Parr [6,7], and their coworkers. The IHSAB approach to conductometric sensor development that we have developed correlates with a basis in physisorption. In contrast, microreactor design correlates with a basis in chemisorptive interaction. The application of the IHSAB concept creates highly variable surface interactions using a diversity of nanostructured oxide fractional depositions. Nanoporous silicon layers positioned on porous silicon (PS) micropores facilitate the application of nanostructured metals, metal oxides, and catalytic nanoparticles, and provide for notably

higher sensitivities and selectivity. These depositions can be made to produce a dominant physisorptive (sensors) or chemisorptive (microreactors) character at the semiconductor interface as the deposited nanostructured metal oxides act as antennas to focus the nature of the surface interaction. Herein, we primarily consider physisorption as it applies to sensor development. However, complementary principles and the HSAB concept can be applied to microreactor design.

5.1 The IHASB Concept as the Basis for the Construction of Nanostructure-Directed Physisorption at Sensor Interfaces

An analyte can donate electrons to a "p-type" PS semiconductor surface and these electrons combine with holes, thus reducing the number of majority charge carriers. This leads to an increased resistance. The process is reversed for an "n-type" semiconductor as the majority charge carriers, electrons, increase and the resistance decreases. We suggest that the IHSAB concept, as it promotes physisorption, can be applied in concert with, and in complement to, the behavior of an extrinsic semiconductor to provide a range of responses that can be used to design and create sensor arrays.

The concept of chemical hardness/softness, first developed by Pearson, [5] has its basis in the nature of metal ion complexation in aqueous solutions. The HSAB theory is a generalization of the Lewis acid/base concept and correlates with CRT [8]. It was given a deep foundation in DFT [7] by Parr and coworkers, following an initial correlation with the molecular properties established by Pearson and Parr [6]. More recently, conflicts underlying the correlation of the DFT and CRT theories have been largely resolved by Cohen and Wasserman [8] as well as Zhan et al., [9] who have further refined the concepts of electronegativity and hardness.

The properties of acids and bases can be described as hard and soft based upon the correlation of several atomic/molecular properties including the ionization potential (I) the electron affinity (A) and the chemical potential (μ). These can be correlated, in

concert with the HOMO–LUMO gap concept from molecular orbital (MO) theory as the Kohn–Sham orbitals replace the MOs. [7a] Examples in terms of groups of hard, borderline, and soft acids and bases are given in Table 5.1. For a soft acid, the acceptor atom is of low positive charge, of large size, and has polarizable outer electrons. In a hard acid, the acceptor atom is of small size and not easily polarized. In a soft base, in precise contrast to a hard base, the donor atom is of low electronegativity. It is easily oxidized, and highly polarizable, with low-lying unoccupied MOs. The HSAB principle was initially based on empirical observations. Yet, as it groups acids and bases, a basis for the concept has been developed in terms of DFT. This basis follows the principle that soft–soft combinations produce significant covalent bonding and hard–hard combinations produce significant ionic bonding. The HSAB principle states that hard acids prefer to coordinate to hard bases whereas soft acids prefer to coordinate to soft bases. The driving principle to promote physisorption represents the inverse (IHSAB) of the concept to form strong chemical bonds.

Table 5.1 Exemplary Hard, Borderline and Soft Acids and Bases.

Table 1. Exemplary Hard, Borderline, and Soft Acids and Bases[a].

	Hard	Borderline	Soft
Acids	H^+, Li^+, Na^+, K^+ Be^{2+}, Mg^{2+}, Ca^{2+} Cr^{2+}, Cr^{3+}, Al^{3+} SO_3,BF_3,Sn^{+4}, Ti^{+4}	Fe^{2+},Co^{2+}, Ni^{2+} Cu^{2+}, Zn^{2+}, Pb^{2+} SO_2, BBr_3, Sn^{2+} NO_2, NO^+	Cu^+,Au^+,Ag^+,Tl^+,Hg^+ Pd^{2+}, Cd^{2+}, Pt^{2+}, Hg^{2+} BH_3
Bases	F^-,OH^-,H_2O, NH_3 CO_3^{2-}, NO_3^-, O_2^-	NO_2^-, SO_3^{2-}, Br^- N_3^-, N_2, H_2S C_6H_5N, SCN	H^-, R^-, CN^-, CO, I^- SCN^-, R_3P, C_6H_6 R_2S

[a] Inorganic Chemistry, J.E. Huheey, E.A. Keiter, R.L. Keiter, 4th Edition, Harper Collins College Publishers.

In contrast to the driving force of the HSAB concept and chemisorptive interaction, to create sensitive, rapidly responding, and *reversible* porous silicon gas sensors, it is necessary to avoid processes which lead to strong ionic or covalent bonding. Rather, we emphasize the inverse correlation focused on physisorption with minimal chemical interaction. This would suggest the result, which the data in Table 5.2 and the following sections exemplify, that a general approach to conductometric chemical sensor development should follow the inverse of the HSAB concept of acid-base chemical interaction. The changes in response of nanostructure particle modified porous silicon interfaces outlined in the following discussion can be correlated with this inverse (IHSAB) behavior.

5.2 Physisorption and the Response of a Sensor Platform

The introduction of nanostructures to the micro/nanoporous PS framework can selectively modify the resistance response to considerably improve gas detection. In a set of initial experiments [2,4,10], we determined that the concentration of SnO_2 and Au_xO nanostructures on the micro/nanoporous framework needed to produce an enhanced sensitivity for PS (Figure 5.1) is notably less than the nanostructure deposition illustrated in Chapter 3. The deposited nanostructures are sparsely interspersed onto the micro/nanoporous framework. An SnO_x deposited sensor, in particular, allows the room temperature detection of CO at the sub-ppm level considerably below the sensitivity of other PS sensors [11-13]. This SnO_2 deposited sensor can be compared with PS-based sensors whose resistances exceed hundreds of kΩ, operating on a 2 V bias [11], SnO_2 sensors operating at 300°C - 500°C [12], and similar gas sensors operating at 2-5 V. [13] It has been possible to considerably improve the basic hybrid PS sensor micro/nanoporous interface. With this improvement, electroless gold treatments of the PS interface forming Au_xO nanostructured deposits have lead to a substantial increase in sensitivity (signal/noise) for ammonia [4]. However, the ratio of the improvement in

response of the Au_xO nanostructure deposited hybrid PS surface to that of an untreated PS surface closely parallels that for Fig. 5.1 and is again duplicated by the newly expanded and reproduced response array for NH_3 presented in Table 5.2. The results outlined in Figure 5.1 and the newly obtained data in Table 5.2 are fundamental to the development of the IHSAB concept which we outline in this study.

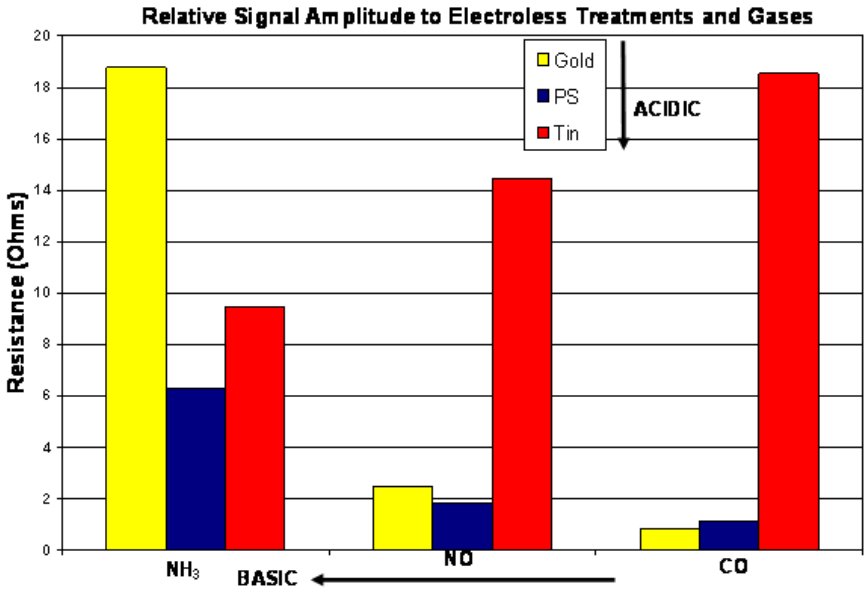

Figure 5.1. Comparison of response for sensors that are untreated, treated with electroless gold, or treated with electroless tin, and tested with 30 repeat pulses of 20 ppm NO_x, NH_3, or CO. The average resistance change is given (data from Ref. 2 in correlation with the Inverse HSAB concept). The increasing basic strength of the test gas and the increasing acidic strength of the nanostructured deposits are shown with arrows.

We have performed extensive additional studies involving the sensing of a number of gases, including the sensing of phosphine, for several nanostructure modified PS surfaces. These specific experiments, carried out in a manner similar to that previously described [2,4,14,15] are summarized in Table 5.2. Table 5.2 presents several correlated responses. The results which we have obtained for phosphine, the most complicated system we have studied, (NH_3 is of similar complexity) are depicted for an Au_xO nanostructure coated micro/nanoporous PS surface in Figure 5.2 [15]. PH_3 is

known to display an even greater degree of interaction with a nanostructured surface and have a higher sticking coefficient than NH_3 [2,14,15]. The tendency toward the equilibration of adsorption and desorption, also manifest in ammonia, can produce a gradual increase in the sensor baseline. Although we operate the sensors in an unsaturated mode [2,14], the sensor response and recovery time scales are distinctly different. The observed baseline drift can also result from weak chemisorptions of PH_3 superimposed on a dominant physisorption [15]. Purging the sensor surface with ultrahigh purity (UHP) nitrogen for longer durations, following exposure to the 300s PH_3 gas pulse (Fig. 5.2), enhances the return to the initial baseline. This return to baseline can also be further improved by more tightly constraining the gas flow path to the sensor surface from its current design for operation at atmospheric pressure (depicted in Ref. 2(a), Fig. 6). In addition, the application of FFT pulsing techniques can be used to average out the effects of the baseline drift.

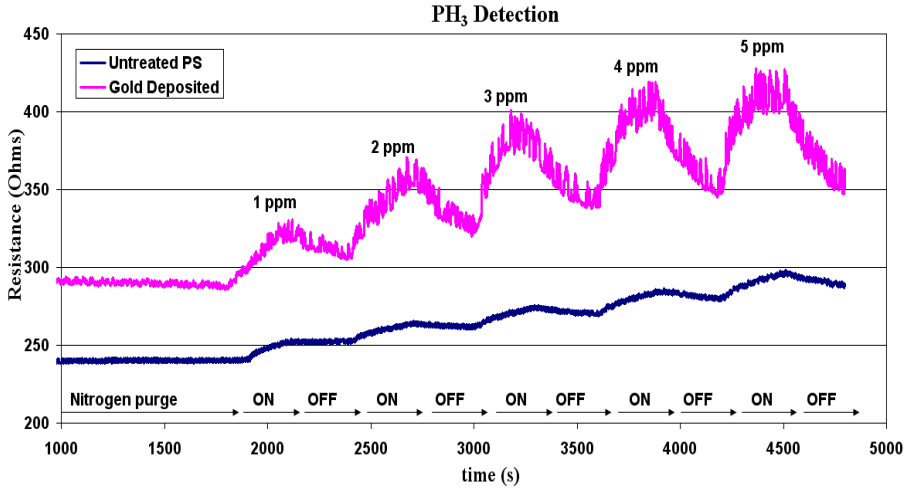

Figure 5.2. Improved PH_3 response to an electroless Au_xO coating. Here, 1,2,3,4, and 5 ppm of PH_3 is pulsed onto the sensor surface every 300s. For the first 1800s an N_2 purge is applied for resistance stabilization [19].

Figure 5.2 demonstrates that the resistance change for PH_3 resulting from an Au_xO nanostructure deposited surface is close to five times that of the untreated surface. Further

data obtained for electroless tin, copper, and nickel treatments are indicated in Table 5.2. Table 5.2 also includes additional new data obtained for NO [16] with electroless tin, copper, nickel, and gold treatments to the hybrid PS interface form Sn^{+4}, $Cu^{+1,+2}$, and Ni^{+2} oxides, and Au_xO [$Au^{0,+1}$] clustered oxide nanostructured deposits. The individual studies, which allow the detection of PH_3 and NO to < 300 and 650 ppb respectively, the prescription for their formation, and their row matrix of responses will be discussed in more detail for each individual gas [15]. However, the summarized improvement obtained for NO with SnO_2 and NiO deposits vs. the hybrid PS structure is apparent.

Table 5.2 ΔR (coating)/ΔR(uncoated) values are shown for PH_3, NO, and NH_3 resistance changes. Comparison is to an uncoated PS sensor for the analyte gases at 1ppm. The nanostructured coatings deposited to the PS surface are indicated in the Table. Base resistances of the sensors used in these experiments vary from 300 to 500 Ω. Further data points for CO (SnO_2), and H_2S (Au_xO) are discussed in the text.

Table 2. Response to Nanostructured Depositions.

	Tin (SnO_x)	Nickel (NiO)	Copper (Cu_xO)	Gold (Au_xO)
PH_3	**2**	**2.5**	**4**	**5**
NO	**7-10**	**3.5**	**1**	**1.5**
NH_3	**1.5**	**(1.5-2)**	**(2-2.5)**	**~3**

Table 5.2 summarizes the results we have obtained for several nanostructure modified PS surfaces for the gases NH_3, PH_3, and NO at the one ppm level. The ratio of resistance changes are given for the various nanostructure deposits relative to an untreated micro/nanoporous PS structure. In addition, the data obtained for CO, a weak base, demonstrates a significant response increase upon exposure of this gas to an SnO_2 (hard acid, Table 5.1) nanostructure coated surface. The response increases by at least an order of magnitude relative to the untreated PS surface. In contrast, although the response of the PS surface is quite small, the Au_xO treated PS surface response has clearly decreased for CO, signalling the chemical interaction of a weak base with a weak acid

interface. Further data obtained for H_2S [10] (an intermediate base, Table 5.1) indicates a significant increase in response (between 1.5 and 2) for an Au_xO nanostructured oxide (weak acid) coated surface relative to the untreated PS surface. The observed ratios in Table 5.2 demonstrate that the same relative signal improvements for NH_3 and NO, for the new data presented in Table 5.2, are as indicated in Figure 5.3. The ratios of responses are thus maintained for an extended group of experiments. For ammonia, the data in Figure 5.1 has been improved to provide responses over two orders of magnitude larger as a result of improvements in the optimization of the anodization and nanostructure deposition processes. The response change, now on the order of 1000 Ω for 20ppm NH_3 with respect to the untreated porous silicon sensor, corresponds to a similar enhancement increase after an Au_xO nanostructure treatment is applied.

Figures 5.1 and 5.2 and Table 5.2 suggest that the proper combination of nanodeposition techniques can be used to produce combinations of array-based multiple sensor devices of varying sensitivity to a variety of basic gases. The matrix of array responses can be correlated to selectively analyze gas mixtures. For example, a sensor array consisting of an untreated, SnO_x nanostructure coated, and gold clustered oxide nanostructure coated sensor can be used to sensitively test for the presence and relative concentrations of ammonia and nitric oxide. A nanostructured $PS/SnO_2/Au_xO$ sensor combination could provide the basis for developing a sensitive room temperature detector that could be installed as a simple sensor system for asthmatics, for example [2].

5.3 Interaction with Nanostructure Modified Porous Silicon Surfaces

Here, we assess whether the underlying IHSAB principle described above dictates the response that we have observed from several sensor, basic gas, interactions. We suggest that this principle can be extended to the detection of additional gases with the development of a selective nanostructure deposition approach which facilitates reversible physisorption. This approach is based on creating those conditions which represent the

inverse of the concept of hard and soft acids and bases developed by Pearson and others [5,9], based on the creation of significant covalent or ionic bonds which should lead to a significant chemisorptive surface interaction. We suggest that, by monitoring the trends in hard and soft acid and base behavior, first order selections can be made for the appropriate modification of the PS hybrid interface with nanostructured metal/metal oxide coatings to create a range of selectivities for a number of gases [4,10(c), 15]. The development of selective nanostructured coatings that reversibly complex with a gas can be based on an IHSAB concept where we now combine hard Lewis acids with soft Lewis bases or soft Lewis acids with hard Lewis bases. To establish this combination, we follow the trends established for the classification of the hard and soft nature of acids and bases [5,7].

A first order comparison of the response data in Table 5.2 with the exemplary list of hard, borderline, and soft acids and bases in Table 5.1 clearly demonstrates that hard bases such as ammonia (and ~ phosphine) respond most strongly (resistance change) when exposed to a nanostructured Au_xO surface corresponding to a soft acid ($Au^{0, +1}$). In contrast, the soft bases CO (and NO) display a maximum response (change in resistance) upon interaction with the borderline to hard acid SnO_x ($Sn^{+2, +4}$). Note also the minimum response of the untreated PS surface to CO and the subsequent *decrease* for the Au_xO nanostructure treated surface displayed in Figure 5.1. These properties have not changed over an extended period as we observe no clearly measureable response with either an untreated or an Au_xO nanostructure treated PS surface. The decrease in an already small if negligible resistance response for hybrid PS is consistent with the expected effect of chemisorption for the interaction of a weak acid with a weak base to create a stronger, more covalent, chemical bond which does not facilitate electron transfer.

The responses outlined in Table 5.2 in concert with Figures 5.1 and 5.2 and Table 5.1 can be correlated further to generate the materials positioning depicted in Figure 5.3.

This positioning diagram is generated based on the relative responses for the gases we have studied, with several nanostructured deposits over an extended period. We position the five bases NH_3, PH_3, H_2S, NO, and CO relative to the porous silicon (Si^{+1to+4}) and the PS modified acidic interfaces generated with a nanostructured SnO_x ($Sn^{+2,+4}$), Al_2O_3 ($Al^{\sim+3}$), NiO (Ni^{+2}), Cu_xO ($Cu^{+1,+2}$), and Au_xO ($Au^{0,+1}$) deposit. The basis for the positioning of H_2S in Figure 3 is the correlation of the relative responses for one ppm H_2S with an Au_xO deposited surface compared to an untreated PS surface[20] and to the data for NH_3, PH_3, and NO in Table 5.2. Based on ionization potential as well as proton affinity data, we suggest that H_2S lies close to but probably to the soft acid side of PH_3. The basis for the positioning of CO is its virtually non-existent response to Au_xO and its substantial response to SnO_2 summarized in Figure 5.1 and re-evaluated in several experimental tests. Data for Al_2O_3 deposits has been generated only for phosphine for which the response is found to be virtually identical to the hybrid PS interface. Thus the acid strength of the alumina modified PS surface as well as the untreated PS surface and the base strength of PH_3 are closely aligned.

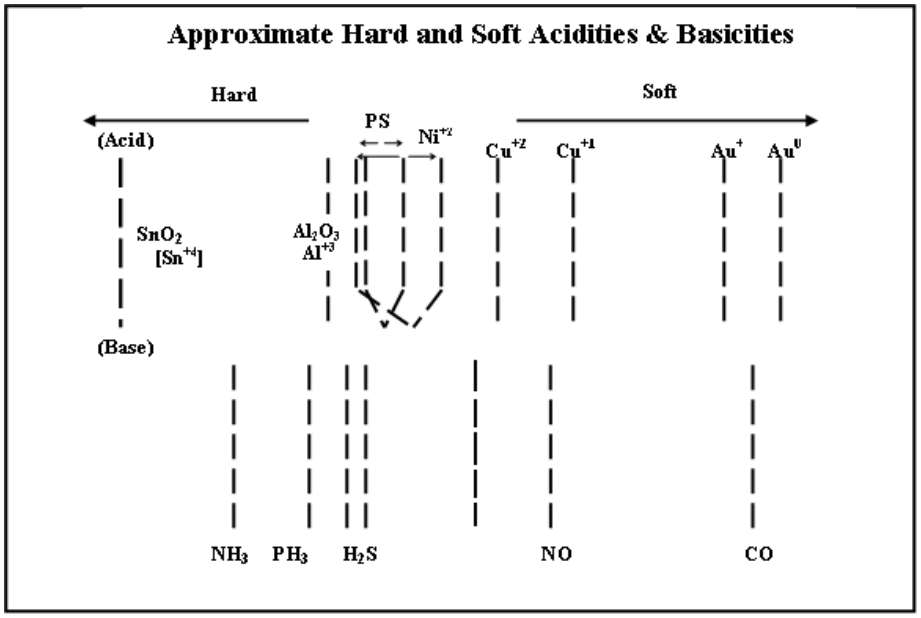

Figure 5.3. Estimated hard and soft acidities and basicities based on resistance changes relative to porous silicon.

We are correlating the interaction of gaseous bases with nanostructured surfaces. The location of each of these bases is evaluated based upon their observed interaction with the range of treated PS surfaces. The data in Table 5.2 suggest that a general approach for optimal PS conductometric sensor response based on physisorption should have as its driving force the combination of a weakly acidic sensor surface with a strongly basic interacting molecule or vice-versa. (Similar comments would apply to a strongly or weakly basic surface). Within the framework of molecular orbital theory, we attempt to promote a mismatch between the HOMO-LUMO gaps associated with the acidic and basic orbitals. This mismatch is, as it should be, to produce rapidly responding, "reversible", sensor configurations, *minimizing* either strong covalent or ionic bonding and maximizing a physisorbed interaction. By promoting this interaction, we minimize the effect of chemical bond formation which inhibits the transfer of electrons to the modified PS interface.

With a focus on sensor array development, the data in Table 5.2, can be correlated with the exemplary information reflected in Table 5.1. The correlation suggests the materials positioning indicated in Figure 5.3 within especially similar molecular analogues. We have constructed Figure 5.3 within the framework of the acid and base character outlined in Table 5.1 considering, to first order, the hard acid strength which we associate with an Sn^{+4} (SnO_2) configuration, the soft acid strength to be associated with an $Au^{0,+1}$ (Au_xO) configuration, and the intermediate (borderline) acid strength we associate with the porous silicon hybrid surface. Here, the silicon oxidation state (Si_xO_y) is considered to vary from +1 to +4 [17]. Superimposed relative to this structure, we insert the results outlined in Table 2 for the intermediate acid Ni^{+2}, the soft and intermediate acids $Cu^{+1,+2}$, and the comparatively strong acid state with which we associate Al^{+3} (Al_2O_3).

There are several additional factors that we take into account in constructing Figure 5.3. A larger resistance change associated with SnO_2 suggests that ammonia lies closer to porous silicon than to the strong Sn^{+4} acid site. The inherently hard basic character of ammonia is also consistent with the strong resistance change observed for its interaction with the Au_xO nanostructure deposited surface (Table 5.2). The behavior of ammonia is also strongly mimicked by phosphine which displays an expected strong increase in resistance change relative to the "p-type" PS surface associated with Cu_xO and Au_xO nanostructure modified surfaces. We observe a decrease in the magnitude of the resistance response increase relative to the untreated PS surface as a result of a (Ni^{+2}) oxide nanostructure deposition. This suggests that the (Ni^{+2}) treated surface lies to the soft acid side of the untreated hybrid PS surface. The remaining interactions with NO and NH_3 suggest a (Ni^{+2}) acid strength in closer proximity to PS. This defines the broader relative response for the Ni^{+2} and hybrid PS regions indicated in Figure 5.3. As we have noted for phosphine, the responses to the hybrid PS structure and an "Al_2O_3" nanostructure treated surface appear virtually identical. Therefore, we anticipate that phosphine lies equally close to Al_2O_3 and PS with NH_3, a stronger base, on the hard base side of PH_3. This also suggests that the acid character of Sn^{+4} considerably exceeds that of Al^{+3}. More recent preliminary results [18] obtained working with MgO treated TiO_2 and TiO_2 nanostructures prepared using sol-gel methods show a 4 to 5 fold increase in resistance change compared to the untreated hybrid PS surface response to PH_3. These responses, thought to be dominated by the action of Ti^{+4}, suggest the response of a harder acid than Sn^{+4} with a moderately strong base, PH_3.

The doublet NO radical has a singly occupied HOMO as compared to the doubly occupied HOMO of closed shell ammonia or phosphine and represents a weak base. The open shell nature of NO would suggest a very different interaction with hybrid PS and the nanostructure treated PS interface. In addition, NO can bind an electron which NH_3 and PH_3 cannot. The soft base-hard acid interaction of NO with a SnO_2 nanostructured

coating leads to a substantial resistance change relative to PS. This is the signature of the reversible interaction of a strongly acidic surface with a weak base. Further, the response to gold, copper, and nickel treated surfaces, while considerably muted relative to the tin treated surface, suggests that NO should be positioned directly below the copper ($Cu^{+1,+2}$) systems and intermediate to gold ($Au^{0,+1}$) and nickel (Ni^{+2}). The interaction of NO with Ni^{+2} suggests a greater separation from nickel than from gold. While PS and Ni^{+2} may lie in a similar intermediate region, the larger resistance change observed for NO with a Ni^{+2} surface suggests that the (Ni^{+2}) modified PS surface lies to the hard acid side of PS, acting as a harder acid deposited to the PS surface. This again suggests a broader range for the relative response of the Ni^{+2} and PS regions as indicated in Figure 5.3.

5.4 IHSAB Model Influence on the Interaction of Analyte Gases with a Semiconductor Surface

Figure 5.3 is constructed within the framework of an Inverse HSAB concept with a focus toward the improvement of surface physisorption based on select nanoparticle deposition. We offer a plausible mechanistic principal for the sensor resistance changes observed for the effectively oxidized gases considered in this study. The introduction of the nanostructured metal oxides to the nanoporous PS surface modifies the sensing process by transforming the surface of the chemically sensitive “p-type” PS nanoporous layer. It is clear that the sensor resistance increases for “basic” gases which are oxidized (NO, CO, NH_3, PH_3, H_2S). This process is amplified through the interaction of a modified acidic metal oxide surface . If an electron is donated to a “p-type” PS surface, this process will act to reduce the number of majority carriers (holes) and thus will promote an increase in resistance. In contrast, the interaction of a gas that is effectively reduced on “p-type” silicon, exemplified by the acidic gas NO_2, leads to the removal of electrons from the “p-type” PS surface, the increase of majority charge carriers, and a

decreased resistance [18]. In effect the nanostructures act as antennas to transduce charge. This process will be reversed for an “n-type” sensor [19] such as bulk tin oxide where the contribution of electrons to the bulk interface contributes to the number of majority carriers (electrons).

The process of physisorption must involve the interaction of high-lying occupied (low lying unoccupied) molecular orbitals of each individual gas which are the electron donors (acceptors) with the electron acceptor (donor), represented by the acidic (basic) metal oxides used to modify the PS surface and the “p-type” PS itself. This process will differ from gas to gas and with the change in nanostructured deposit. However, the nature of the interaction as it provides for increased physisorption and minimizes chemical bond formation (chemisorption), therefore influencing the flow of electrons from the gaseous molecule to the sensor, provides the basis for the observed resistance change. We suggest that the presence of a fractional nanostructured oxide coating on the PS surface serves to promote further interaction with the interface and that the process whereby a gas transfers or withdraws electrons as it interacts with that surface will be strongly influenced by the balance of chemical bonding, which greatly inhibits electron flow, and physical absorption which can facilitate the process.

In this study, we have considered the fractional coverage of a “p-type” porous silicon surface with several nanostructured metal oxide particles. This fractional coverage, while it influences the physisorption to the PS surface, should not greatly modify the “p-type” character of the generated PS surface used in this study [20]. However, the fractional deposition must be held to a low level. Within this framework, we have demonstrated that the nanostructured deposits, as they influence the resistance change, maintain their characteristics over extended periods of testing.

The precise details of this mechanism and the resistance change which appears to be characteristic of virtually all effectively oxidized (increased resistance) and reduced (decrease in resistance), gases with the individually modified hybrid “p-type” PS surfaces

will require further experimentation and modeling. If we, however, consider an appropriate sensor mechanism for interaction with oxide surface subgroups, the fractional nanostructure coating of a "p-type" sensor is consistent with the change in resistance that we outline above. Basic analytes will provide an electron to the p-type PS surface whereas acidic analytes will remove an electron leading to a decrease or increase in the number of majority carriers respectively. It is important to note that these changes are opposite to the resistance changes for n-type bulk sensors [19].

The conductometric sensors, which we formulate, using the IHSAB principle, are simply designed and can operate with less than 1 mW of power. They are potentially sensitive as well as selective to a wide variety of gases while operated at room temperature. These rapidly ($\leq$ 2 s) and reversibly responding devices, with an inherent low voltage and lower power [2,4,14] can be readily integrated with CMOS electronics into arrays of sensors. This follows from the ability to modify the interaction of a "p-type" PS sensor using a "materials selection table [16]"analogous to Table 5.1 to create arrayed devices. The modified PS sensor is also of interest due to its operation at atmospheric pressure and at room temperature as well as over a single, readily accessible, temperature range with an insensitivity to temperature drift. Many of these improvements are greatly aided by the application of the IHSAB concept.

5.5 Conclusion

We offer an approach to focus the physisorption of an extrinsic semiconductor surface and facilitate significant and predictable changes in sensor surface sensitivity for a variety of gases based on an inverse complementary theory to the well known concept of hard and soft acid and base interactions [5-9]. Similar considerations can also be applied as a first order approach to the focusing of the chemisorptive properties of a semiconductor interface. We suggest that nanostructured sensor surfaces for

conductometric array-based devices be constructed from a finders table by first establishing whether the gas to be detected classifies as a hard or soft acid or base and subsequently developing a range of nanostructured fractional deposits which modify a prepared semiconductor interface to encompass as wide a range of acidity and basicity as possible. More specifically, for the gases considered in chapter, the correlation with the trends in the proton affinity (PA), essentially the gas phase basicity, and their interaction with the modified acidic PS surface also bears serious consideration [21]. However, as an overriding principle, the maximum physisorbtion response (resistance change) is to be expected from combinations of hard acid surfaces with soft bases and vice versa. While there are other factors, including steric effects, polarization [22], and the nature of the open or closed shell character of interacting molecules to consider, we suggest that the acid/base makeup of the nanostructure modified PS sensor surface and the mismatch of the hard and soft acid/base character with the species to be detected is the primary driving force for creating the most efficient modified sensor surface. This comment must be tempered by noting that the interaction of a strongly acidic surface with a weakly basic gas can influence the characteristic interactions of this gas. Further, the interaction of amphoteric gases must also be carefully assessed within the model.

5.6 References

[1] L. Seals, L.A. Tse, P.J. Hesketh, J.L. Gole, J. Appl. Phys., 91, 2519-2523 (2002).

[2] (a) S. Lewis, J. DeBoer, J.L. Gole, P. Hesketh, Sens. Actuators, B, Chem 2005, 110, 54-65. (b) J.L. Gole, S. Lewis, S. Lee, Phys. Stat. Sol. A , 204, 1417-22 (2007) and references therein.

[3] J.L. Gole, MRS Bulletin, 28, 263 (2003).

[4] (a) S. Ozdemir, J.L. Gole, Chem. Sens. 8: Chem (Gas, Ion, Bio) Sens. and Analytical Systems, ECS Transactions, 16(11), 379-387 (2008). (b) J.L. Gole, J. Corno, ; S. Ozdemir, S. Prokes, H-C Shin, Phys. Stat. Sol. C, 6, 1773-1776 (2009).

[5] See for example
(a) R.G. Pearson, Coordin. Chem. Rev., 100, 403-25 (1990).
(b) R.G Pearson, J. Am. Chem. Soc., 85, 3533-3539 (1963).
(c) R.G Pearson, Chemical Hardness, John Wiley VCH, Weinheim, 1997.
(d) R.G Pearson, J. Chem. Sci., 117(5), 369-377 (2005).
(e) R.G Pearson, Inorg. Chem., 27, 734-740 (1988).

[6] R.G Parr, R.G Pearson, J. Am. Chem. Soc., 105, 7512-7516 (1983).

[7] (a) R.G Parr, W. Yang. Density Functional Theory of Atoms and Molecules, Oxford University Press, New York, 1989. (b) P. Geerlings, F. De Proft, W. Langenaeker, Chem. Rev. 2003, 109, 1793.

[8] M.H. Cohen, A. Wasserman, J. Phys. Chem., 111, 2229-2242 (2007).

[9] C.G. Zhan, J.A. Nichols, D.A. Dixon, J. Phys. Chem. A, 107(20), 4184-4195 (2003).

[10] J.L. Gole, A.G. Fedorov, P. Hesketh, C. Burda, Phys. Stat. Sol. C, 1(S2), S188-197 (2004).

[11] A. Foucaran; F. Pascalk-Delannoy, A. Giani, A. Sackda, Commette , P. Boyer, Thin Sol. Films , 297, 317 (1997).

[12] P.T. Moseley, Meas. Sci. Technol., 8, 223 (1997).

[13] I. Schechter; M. Ben-Chorin; A. Kuz, Anal. Chem., 67, 3727 (1995).

[14] (a) J.L. Gole, S.E. Lewis, SPIE-Proceedings, 5732, 573-583 (2005). (b) J.L. Gole, S.E. Lewis, A. Fedorov, S. Prokes , SPIE-Proceedings, 1-12:5929-08 (2005). (c) S. Ozdemir, J.L. Gole, Current Opinion in Solid State and Materials Science, 11, 92-100 (2007).

[15] S. Ozdemir, J.L. Gole, "A Phosphine Detection Matrix Using Porous Silicon Gas Sensors", Sensors and Actuators B, 151, 274-280 (2010).

[16] J.L. Gole, "A general approach to creating selective metal coatings at a nano-microporous porous silicon interface for sensor applications", 2006, Continuation in part, Patent Applied for.

[17] J.L. Gole, M.G. White, T-H Wang, C. Watkins, S.C. Street; D.A. Dixon, "The surprising oxidation state of fumed silica and the nature of water binding to silicon oxides and hydroxides", submitted.

[18] S. Ozdemir, J.L. Gole unpublished.

[19] J. Janata, Solid State Chemical Sensors, 1985 Huber (Editor). P.T. Moseley, B.C. Tofield Solid State Gas Sensors 1987 Adam Hilger Series on Sensors. M.J. Madou, S.R. Morrison Chemical Sensing with Solid State Devices 1989.

[20] The porous silicon surface is believed to consist of silicon oxides and silicon oxyhydrides. J,L. Gole, E.C. Egeberg; E. Veje, A. Ferreira de Silva, I. Pepe, D.A. Dixon, J. Phys. Chem.B , 110, 2064 (2006).

[21] D.A. Dixon, private communication. J.L. Gole and D.A. Dixon, unpublished

[22] P. Politzer, J. Chem. Phys., 86, 1072 (1987).

CHAPTER 6

CONCLUSION

A PS gas sensor has been used to detect NO, NH_3, PH_3 by employing different nanostructured metal oxide nanoparticle depositions. Both sol gel methods and physical vapor deposition techniques are employed for forming the nanoparticles. The selective coatings include electroless coatings such as SnO_2, Cu_xO, Au_xO nanoparticles such as TiO_2, Al_2O_3, ZrO_2. These depositions are verified with SEM and XPS measurements.

NH_3 and PH_3 have been detected below ppm levels with various nanostructure depositions. We have achieved significant improvements in the sensor response when naked porous silicon is deposited with Au_xO and Cu_xO nanostructures. We have evaluated the order of magnitude dimensions of the hybrid PS porous layer, and the dominance of Knudsen diffusion, taking into account the time scales of the response process.

We have achieved significant improvements in the sensor's NO response when naked "p-type" porous silicon is coated with SnO_2 dominant nanostructures. The behavior that we observe here may be useful for the creation of a portable sensor system for the early detection of the onset of an asthma attack. A peculiar NO to NO_2 conversion on the porous surface is observed. The interaction of NO_2 with a "p-type" PS or nanostructure modified "p-type" PS sensor results in a decrease in the sensor resistance

We have also developed an approach to a general metal oxide deposition strategy which is based upon an IHSAB concept designed to create a dominant physisorptive interaction for the modified PS interface.

APPENDIX I

TOXIC GAS DATA

Name	Formula	EH40 WEL (Long)	EH40 WEL (Short)	OSHA (PEL)	ACGIH (TLV)
Ammonia	NH_3	25 ppm	35 ppm	50 ppm	25 ppm
Arsine	AsH_3	0.05		0.05	0.05
Boron Trichloride	BCl_3				
Boron Trifluoride	BF_3				
Bromine	Br_2	0.1	0.3	0.1	0.1
Carbon Monoxide	CO	30	200	50	25
Chlorine	Cl_2	0.5	1	1	0.5
Chlorine Dioxide	ClO_2	0.1	0.3	0.1	0.1
Diborane	B_2H_6			0.1	0.1
Dichlorosilane	H_2Cl_2Si				
Dimethyl Amine	C_2H_7N	2	6	10	5
Dimethyl Hydrazine	$C_2H_8N_2$				0.01
Disilane	Si_2H_6				
Ethylene Oxide	C_2H_4O	5		1	1
Fluorine	F_2	1	1	0.1	1
Germane	GeH_4	0.2	0.6		0.2
Hydrazine	N_2H_4	0.02	0.1	1	0.01
Hydrogen	H_2				Asphyxiant
Hydrogen Bromide	HBr		3	3	2
Hydrogen Chloride	HCl	1	5	5	2
Hydrogen Cyanide	HCN		10	10	4.7
Hydrogen Fluoride	HF	1.8	3	3	3
Hydrogen Iodide	HI				
Hydrogen Peroxide	H_2O_2	1	2	1	1
Hydrogen Selenide	H_2Se			0.05	0.05
Hydrogen Sulfide	H_2S	5	10	20	10
Methyl Fluoride	CH_3F				
Monomethyl Hydrazine	CH_6N_2				0.01
Nitric Acid	HNO_3	2	4	2	2
Nitric Oxide	NO			25	25
Nitrogen Dioxide	NO_2			5	3
Nitrogen Trifluoride	NF_3			10	10
Ozone	O_3			5	5
Phosgene	$COCl_2$	0.02	0.06	0.1	100 ppb
Phosphine	PH_3		0.3	0.3	0.3
Propylene Oxide	C_3H_6O	5		100	2
Silane	SiH_4	0.5	1		5
Sulfur Dioxide	SO_2			5	2
Sulfuric Acid	H_2SO_4				0.05
Toluene Diamine	$C_7H_{10}N_2$	50	150		
Toluene Diisocyanate	$C_9H_6N_2O_2$		0.02		0.005
Triethyl Amine	$C_6H_{15}N$	2	4		5

WEL=Work Place exposure **PEL**=Permissible Exposure Limit **TVL**=Threshold Exposure Value

APPENDIX II

PATTERNS ON THE POROUS SILICON SURFACE

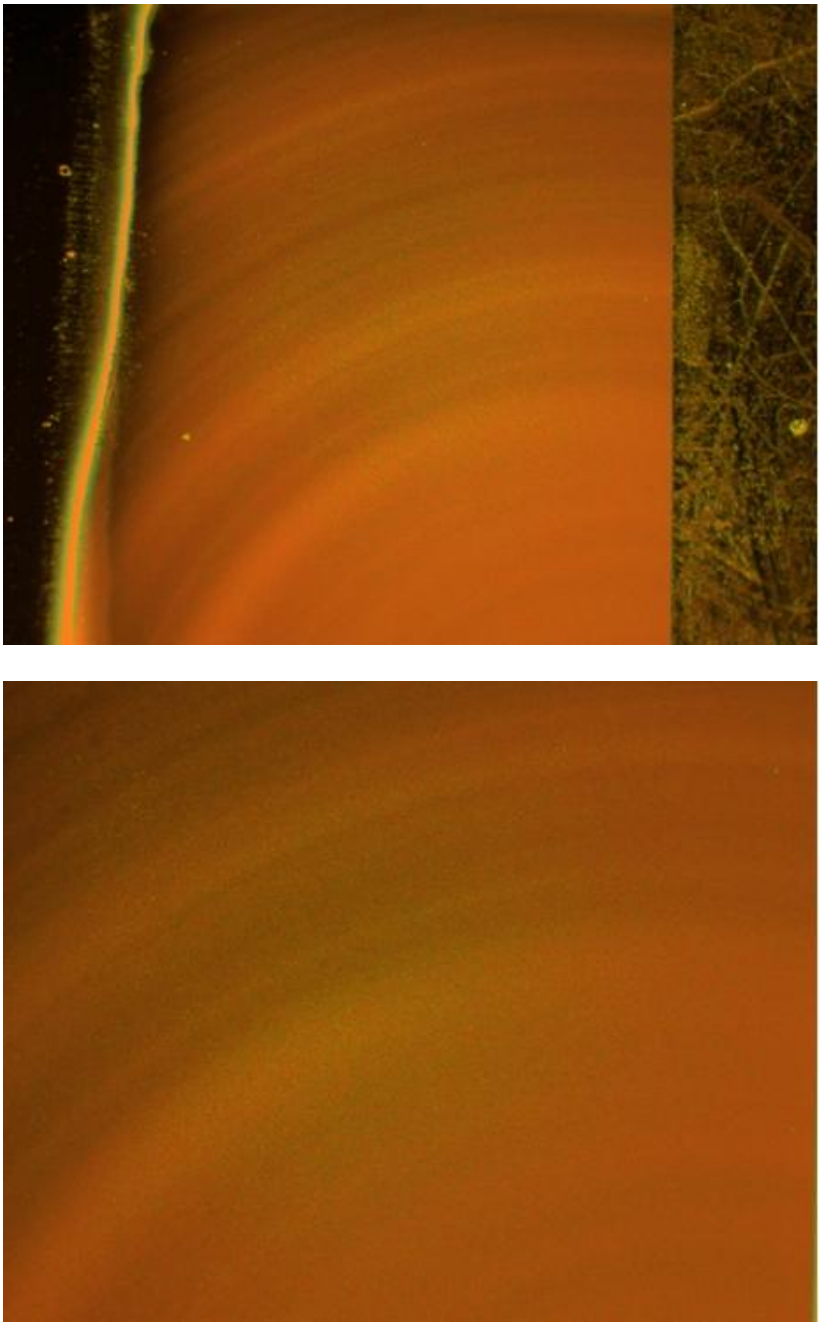

Figure 1. Photos of the top surface of an anodized p-type Si sample taken by using an optical microscope. Top: Circular patterns which can be clearly seen by naked eye on the anodized silicon surface. The circular pores which have average 1.5 μ diameter are randomly dispersed on PS. Bottom: Zoomed into the largest ring depicted in the top photo.

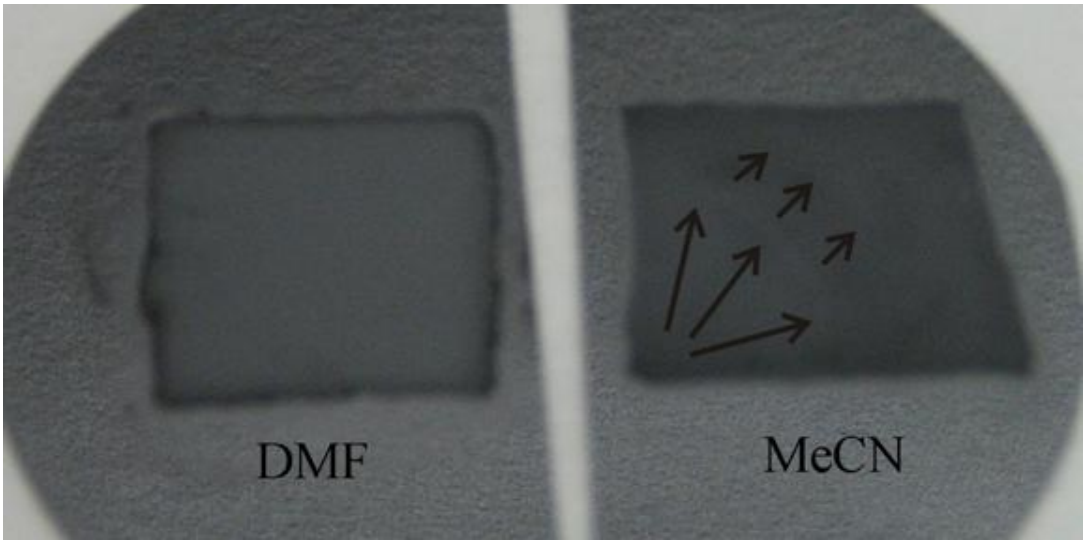

Figure 2. The digital camera shots of two halves of electrochemically etched p type (14-22 Ωcm) wafer. The left half is anodized in a HF:DMF (1:30) solution with 10 mA current for 2700s and the right half is anodized in 20 ml MeCN, 0.8 ml HF and 0.7 gr of TBAP with 20 mA current. In each case, the etch area is about 4 cm^2. While the DMF etch resulted in virtually pale porous surface, the white rings observable on the right half etched in MeCN are marked with arrows in the figure.

APPENDIX III

SURFACE PORE COVERAGE CALCULATED BY IMAGE PROCESSING

```
close all;clear all;clc
img=imread('deneme1.JPG');
img=double(img);
sz = size(img);
I = zeros(sz(1),sz(2));
for ii = 1: sz(2)
   for jj=1:sz(1)
   I(jj,ii) = (img(jj,ii,1) + img(jj,ii,2) + img(jj,ii,3))/3;
   end
end
figure; imagesc(I); colormap gray; axis image;
I= I-min(I(:));
I=I./max(I(:));

level = graythresh(I);
BW = im2bw(I,level);
figure; imagesc(BW);
colormap gray;
black = find(BW==0);
porosity = length(black)/(sz(1)*sz(2))
```

APPENDIX IV

ETCH PROGRAM

Screen Shots of the Block Diagram of the 2-Step (Divided into 2x2 matrix)

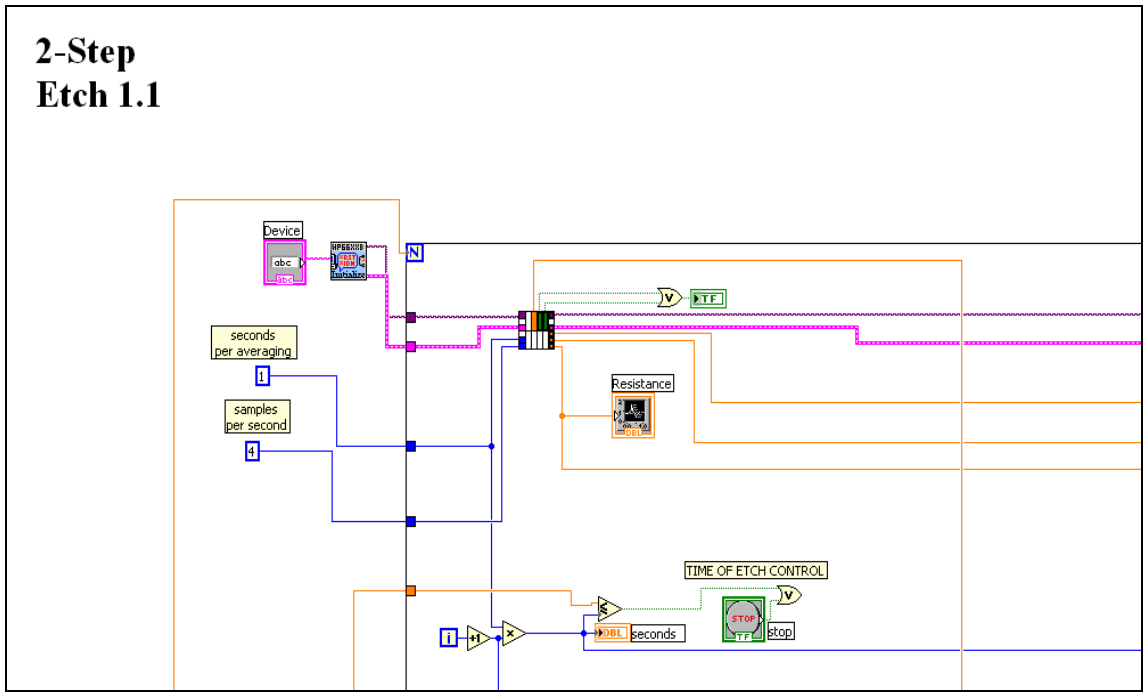

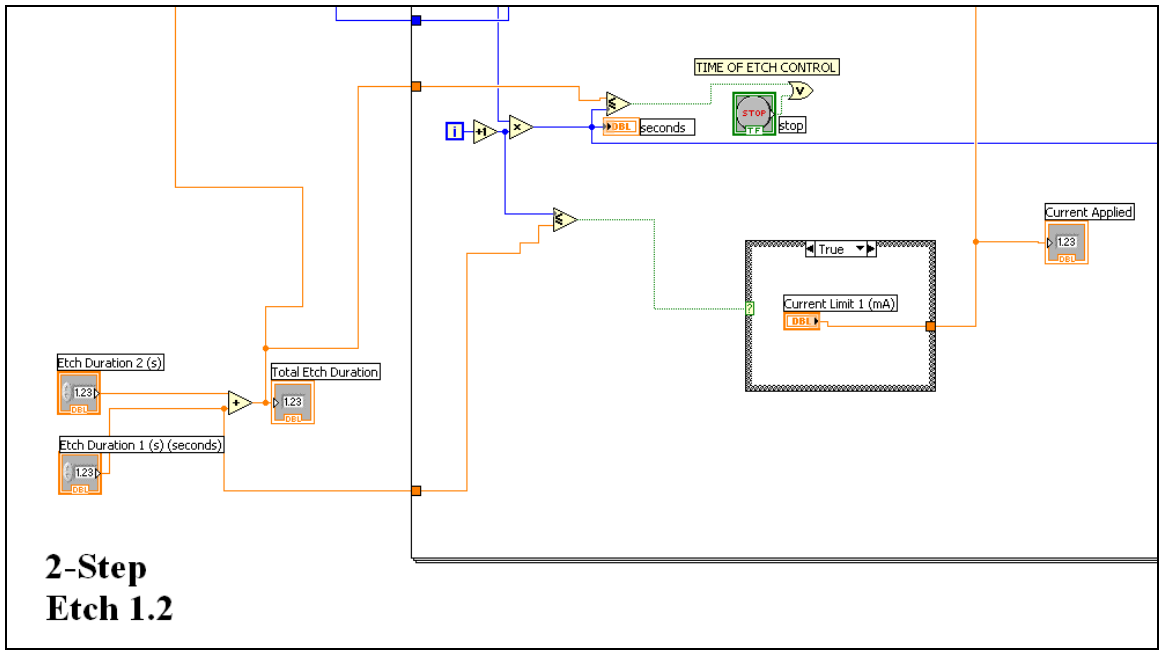

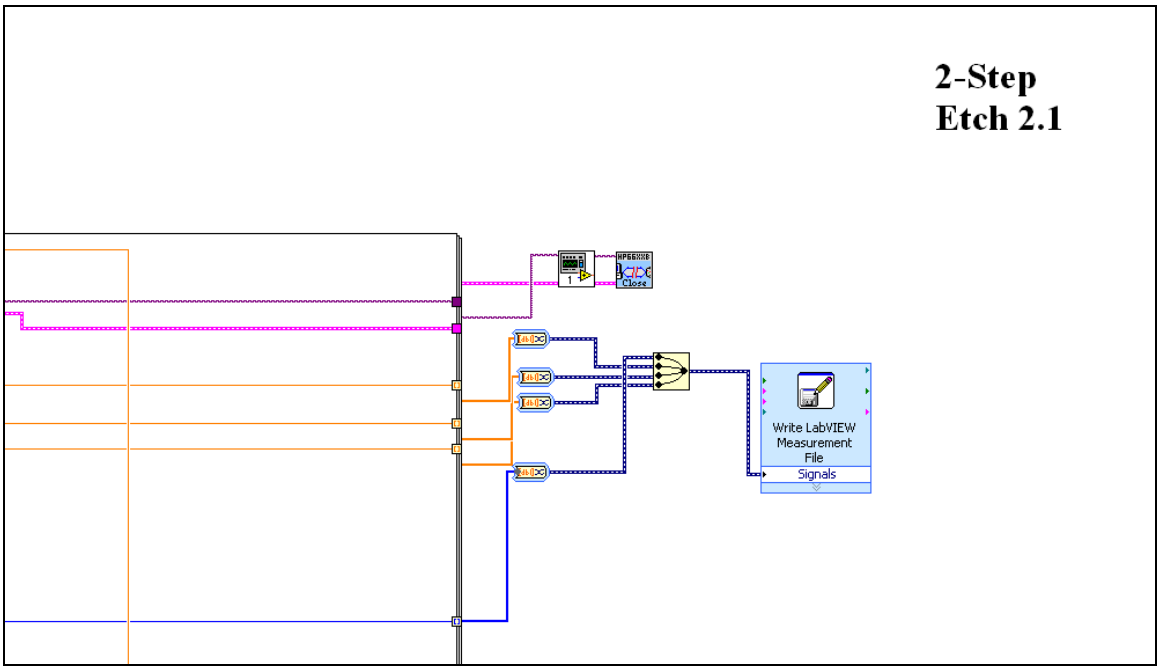
2-Step
Etch 2.1
Write LabVIEW
Measurement
File
Signals

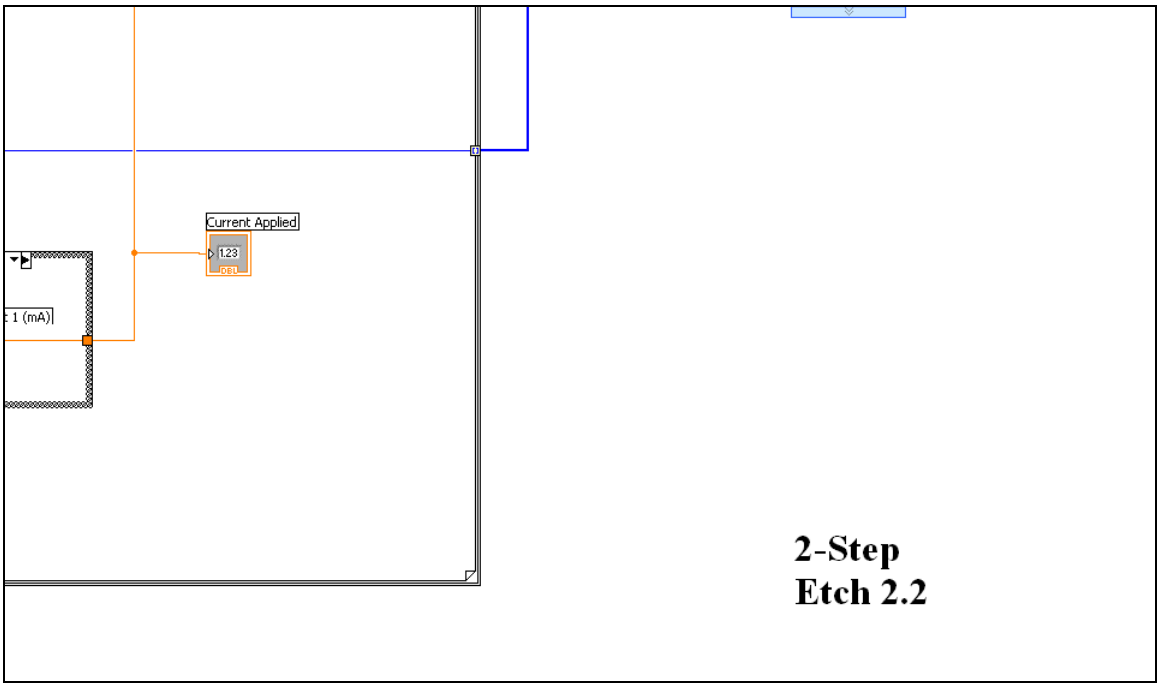
Current Applied
1.23
DBL
1 (mA)
2-Step
Etch 2.2

2-Step Etch Front View

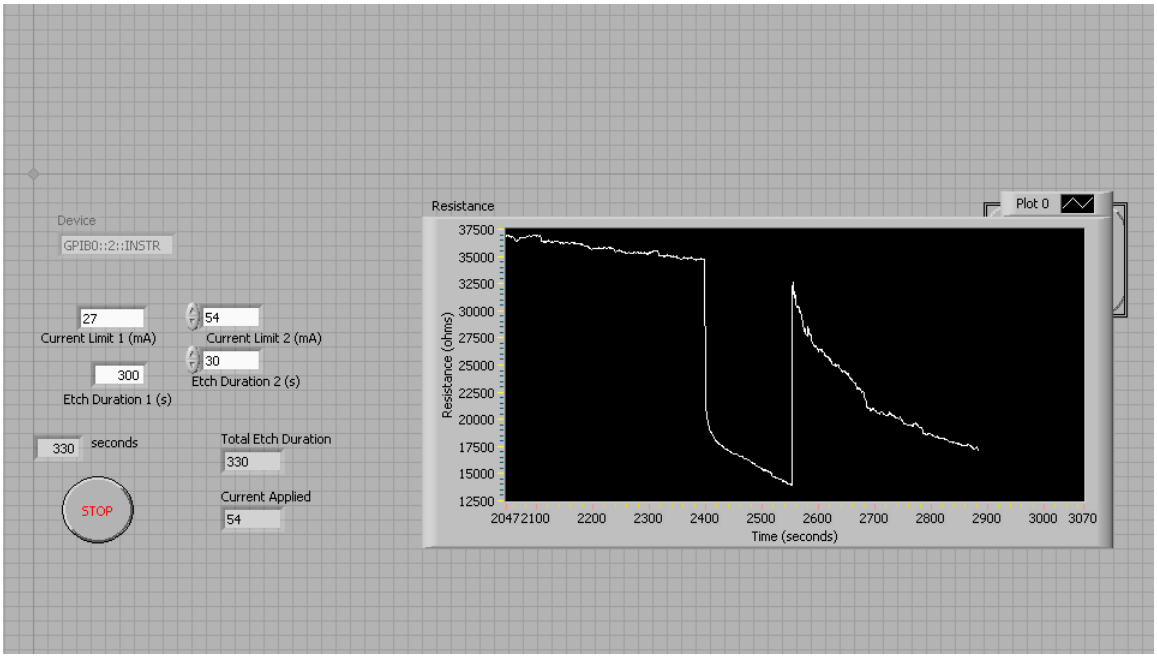

MFC Controller and Measurement System Block Diagram (Divided into 4x2 Matrix)

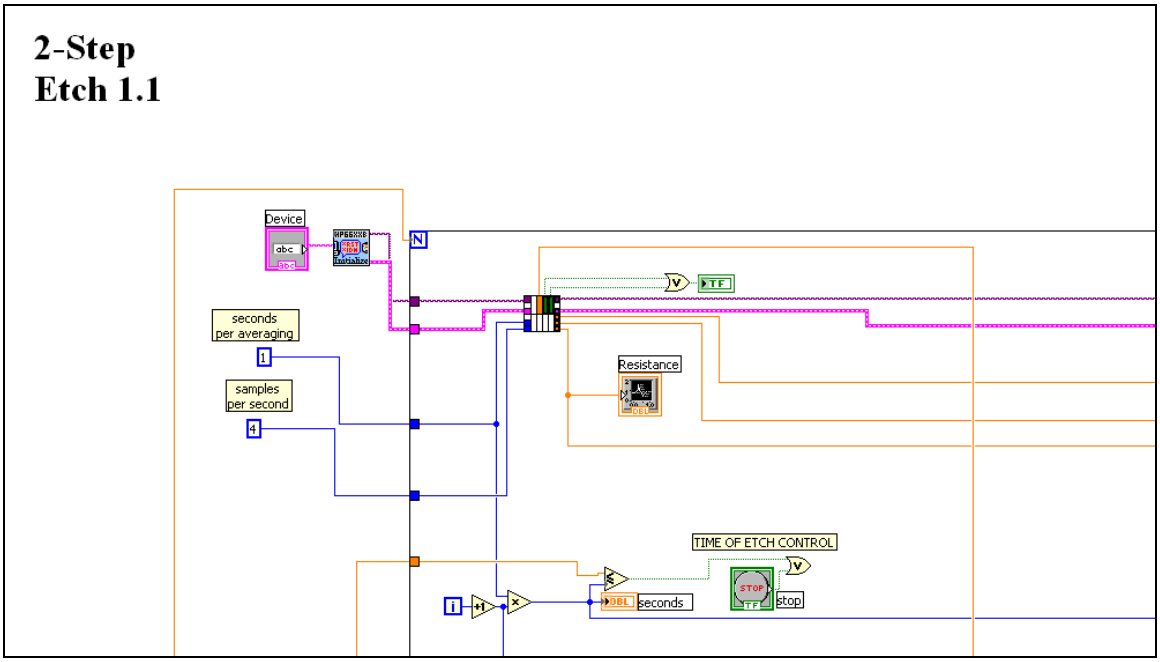

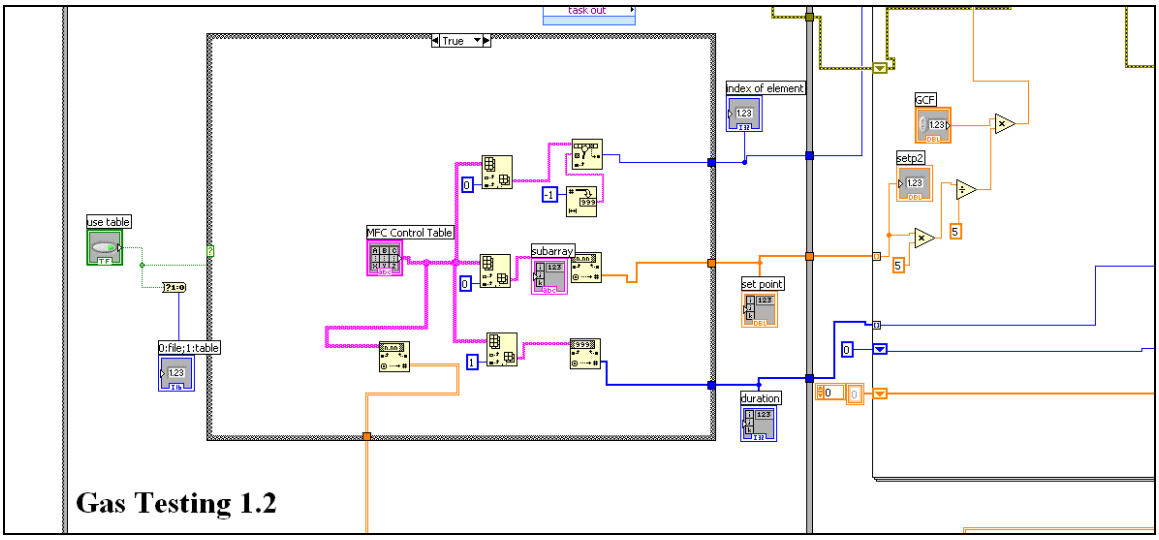
task out
True
index of element
GCF
setp2
use table
MFC Control Table
subarray
set point
0:file;1:table
duration
Gas Testing 1.2

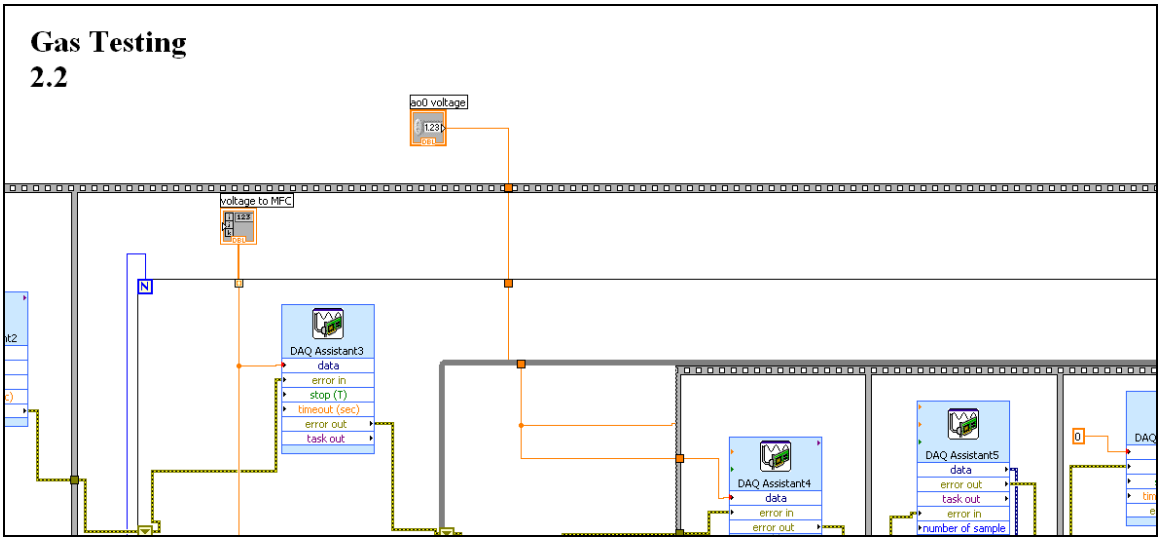
Gas Testing
2.2
ao0 voltage
voltage to MFC
DAQ Assistant3
data
error in
stop (T)
timeout (sec)
error out
task out
DAQ Assistant4
data
error in
error out
DAQ Assistant5
data
error out
task out
error in
number of sample

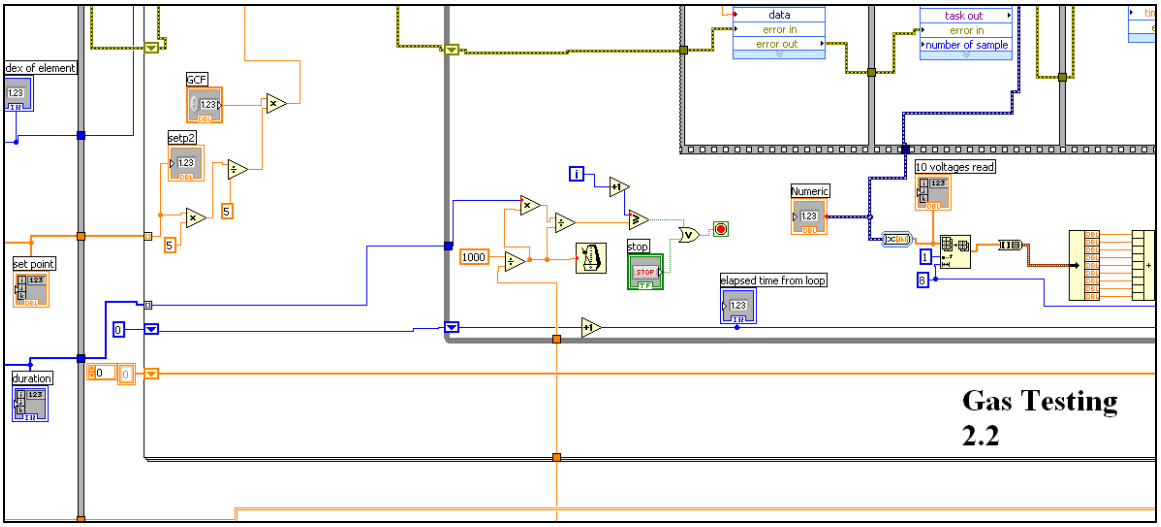
data
error in
error out
task out
error in
number of sample
dex of element
GCF
setp2
10 voltages read
Numeric
set point
1000
stop
elapsed time from loop
duration
Gas Testing
2.2

Gas Testing
3.1

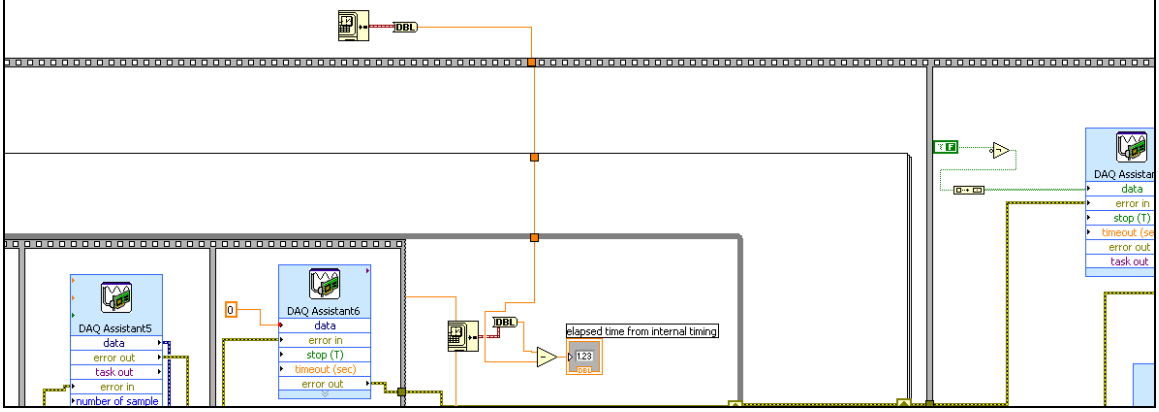

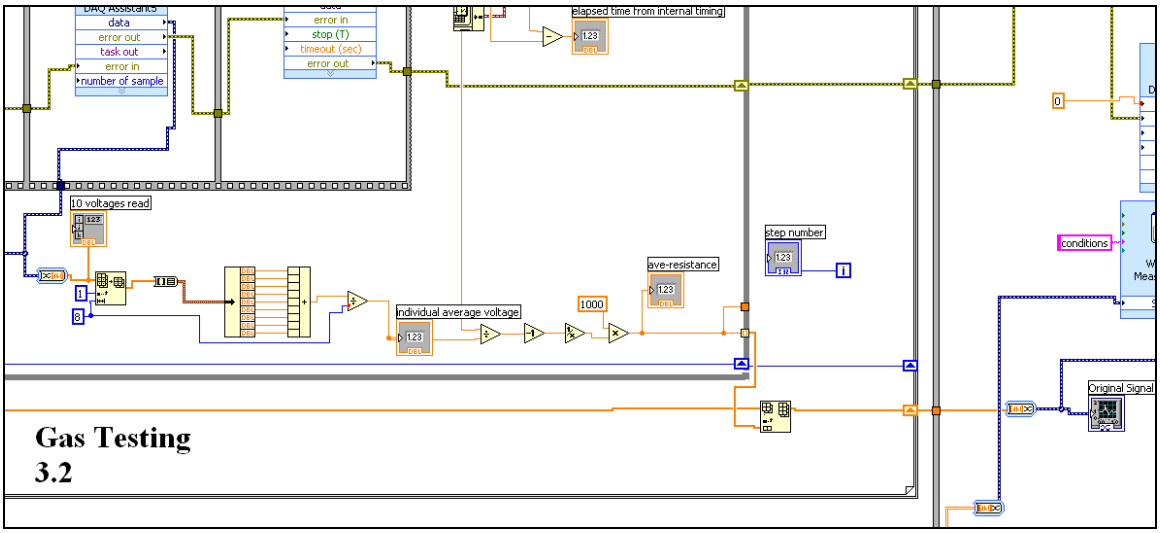

Gas Testing
3.2

Gas Sensing
4.1

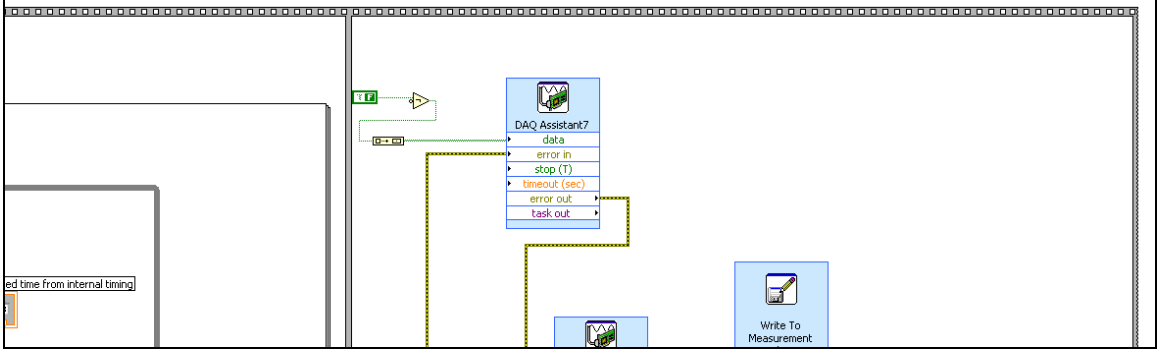

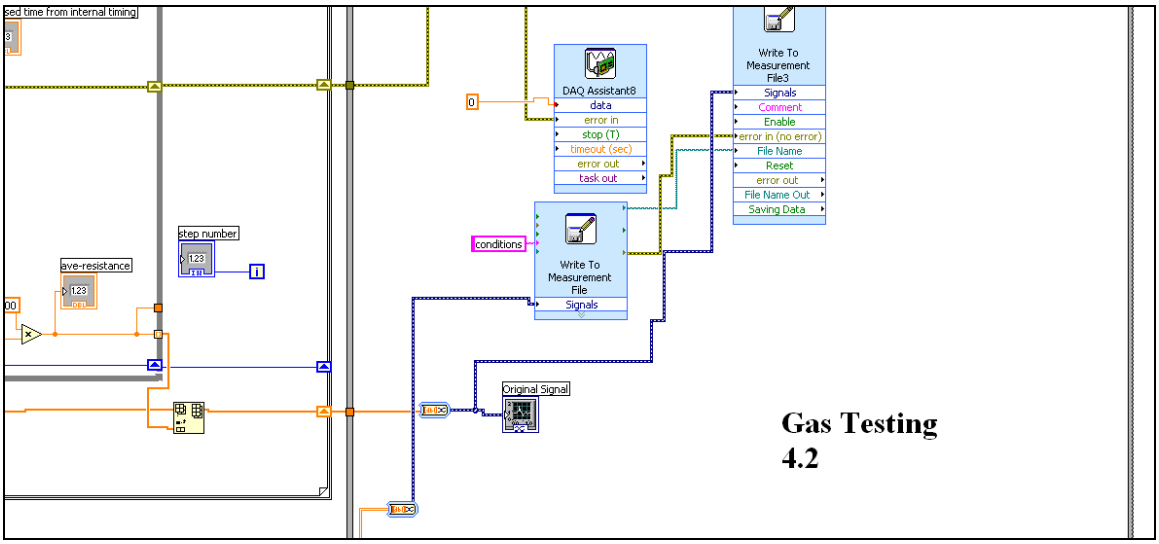
sed time from internal timing
step number
ave-resistance
DAQ Assistant8
data
error in
stop (T)
timeout (sec)
error out
task out
Write To Measurement File3
Signals
Comment
Enable
error in (no error)
File Name
Reset
error out
File Name Out
Saving Data
conditions
Write To Measurement File
Signals
Original Signal
Gas Testing
4.2

APPENDIX IV

SHADOW MASK

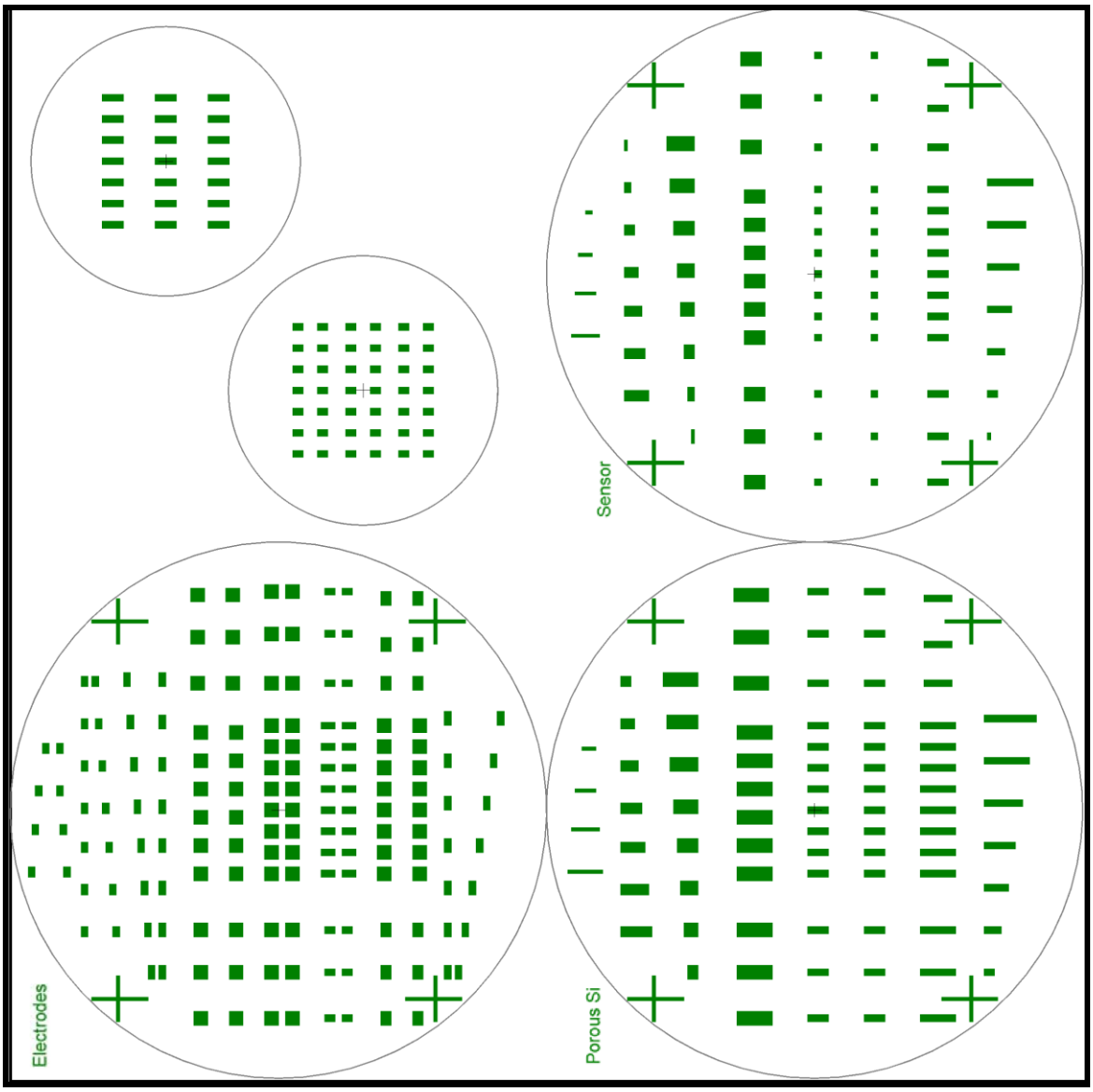

VITA

SERDAR OZDEMIR

Serdar OZDEMIR was born in Turkey. Serdar received bachelor of science and master of science degrees from the Bilkent University Physics Department in 2002 and 2004 respectively. He received a nonthesis master of science degree from the Materials Science and Engineering Department at Georgia Institute of Technology in 2009. He has worked on his PhD degree, with a focus on porous silicon gas sensors in the School of Physics at the Georgia Institute of Technology until March 2011. Serdar will continue his career in the semiconductor industry.